

Sensing, communication and illumination with LED lighting systems

Citation for published version (APA):

Li, S. (2017). *Sensing, communication and illumination with LED lighting systems*. [Phd Thesis 1 (Research TU/e / Graduation TU/e), Electrical Engineering]. Technische Universiteit Eindhoven.

Document status and date:

Published: 06/06/2017

Document Version:

Publisher's PDF, also known as Version of Record (includes final page, issue and volume numbers)

Please check the document version of this publication:

- A submitted manuscript is the version of the article upon submission and before peer-review. There can be important differences between the submitted version and the official published version of record. People interested in the research are advised to contact the author for the final version of the publication, or visit the DOI to the publisher's website.
- The final author version and the galley proof are versions of the publication after peer review.
- The final published version features the final layout of the paper including the volume, issue and page numbers.

[Link to publication](#)

General rights

Copyright and moral rights for the publications made accessible in the public portal are retained by the authors and/or other copyright owners and it is a condition of accessing publications that users recognise and abide by the legal requirements associated with these rights.

- Users may download and print one copy of any publication from the public portal for the purpose of private study or research.
- You may not further distribute the material or use it for any profit-making activity or commercial gain
- You may freely distribute the URL identifying the publication in the public portal.

If the publication is distributed under the terms of Article 25fa of the Dutch Copyright Act, indicated by the "Taverne" license above, please follow below link for the End User Agreement:

www.tue.nl/taverne

Take down policy

If you believe that this document breaches copyright please contact us at:

openaccess@tue.nl

providing details and we will investigate your claim.

Sensing, communication and illumination with
LED lighting systems

A catalogue record is available from the Eindhoven University of Technology
Library

ISBN: 978-90-386-4277-2

The work described in this thesis has been carried out at the Philips Lighting
Research in Eindhoven, The Netherlands, as part of the Philips Lighting Research
programme.

© KONINKLIJKE PHILIPS N.V. 2014

All rights reserved. No part of this publication may be reproduced, stored in a
retrieval system, or transmitted, in any form or by any means, electronic, mechan-
ical, photocopying, recording or otherwise, without the prior written permission
from the copyright owner.

Sensing, communication and illumination with LED lighting systems

PROEFSCHRIFT

ter verkrijging van de graad van doctor aan de Technische Universiteit
Eindhoven, op gezag van de rector magnificus prof.dr.ir. F.P.T. Baaijens,
voor een commissie aangewezen door het College voor Promoties, in het
openbaar te verdedigen op 06 juni 2017 om 16:00 uur

door

Shuai Li

geboren te Shanxi, China.

Dit proefschrift is goedgekeurd door de promotoren en de samenstelling van de promotiecommissie is als volgt:

voorzitter:	prof.dr.ir. A. B. Smolders
1 ^e promotor:	prof.dr.ir. F. M. J. Willems
copromotoren:	dr. A. Pandharipande (Philips Lighting)
leden:	prof.dr. U. Mitra (University of Southern California)
	prof.dr.ir. G. Q. Zhang (TUD)
	prof.dr.ir. S. M. Heemstra - de Groot
	dr. D. Giustiniano (IMDEA Networks Institute)
	prof.dr.ir. J. P. M. G. Linnartz

Het onderzoek of ontwerp dat in dit proefschrift wordt beschreven is uitgevoerd in overeenstemming met de TU/e Gedragscode Wetenschapsbeoefening.

Contents

1	Introduction	1
1.1	Introduction	2
1.1.1	Artificial light	2
1.1.2	Solid state lighting	2
1.1.3	LEDs for illumination	3
1.1.4	LEDs for information transmission	4
1.2	LEDs for sensing	5
1.3	Applications with sensing LEDs	8
1.3.1	Color sensing and control	8
1.3.2	Daylight adaptive control	10
1.3.3	LED-to-LED visible light communication	13
1.4	Outline of the thesis	17
1.5	Publications of the author	19
1.5.1	Journal Publications	19
1.5.2	Conference Publications	19
1.5.3	Other Publications	20
1.5.4	Patent Applications	20
	REFERENCES	21
2	LED-based color sensing and control	27
2.1	Introduction	28
2.1.1	Related work on color sensing	28
2.1.2	Contributions of this work	29
2.2	LED system arrangement and prototype design	30
2.2.1	Source and destination LED lamps	30
2.2.2	Color transporter device	32
2.3	Driving Protocol	33
2.4	Color estimation method	34
2.4.1	Sensitivity matrix based color estimation method	35
2.4.2	DWT based color estimation method	36

2.5	Experimental results	38
2.5.1	Implementation of designed prototypes	38
2.5.2	Sensitivity matrix generation	39
2.5.3	Pre-processing of DWT based method	41
2.5.4	Estimation performance	42
2.6	Conclusions	46
	REFERENCES	47
3	Daylight sensing LED lighting system	51
3.1	Introduction	52
3.1.1	Contributions and organization of the work	53
3.1.2	General principle of LED as light sensor	55
3.2	Daylight sensing luminaire prototype	55
3.3	Daylight sensing and illumination control driver protocol	59
3.4	Luminaire calibration and control method	61
3.4.1	Daylight sensing luminaire calibration and control method	61
3.4.2	Benchmark lighting control system	62
3.5	Experimental results	64
3.5.1	Experimental setup	64
3.5.2	Calibration functions	65
3.5.3	Performance evaluation	66
3.6	Conclusions	68
	REFERENCES	72
4	Unidirectional visible light communication and illumination with LEDs	75
4.1	Introduction	76
4.2	System structure	77
4.3	Front-end design	79
4.4	Physical layer protocol	81
4.4.1	Encoding scheme and PHY frame structure	82
4.4.2	Decoding scheme	83
4.4.3	Semi-synchronization scheme	86
4.4.4	Flicker mitigation	88
4.5	Experimental Results	90
4.5.1	Prototype implementation	90
4.5.2	Calibration and semi-synchronization	91
4.5.3	Communication performance	94
4.5.4	Illumination performance	97
4.6	Conclusions and discussions	98

REFERENCES	100
5 Adaptive visible light communication and illumination with LEDs	103
5.1 Introduction	104
5.2 System structure	105
5.3 Adaptive VLC transmitter	107
5.3.1 Redundant encoder and frame structure	107
5.3.2 Dimming support	108
5.3.3 Adaptive modulation	109
5.4 Adaptive VLC receiver	110
5.4.1 LED sensing front-end and phase-lock unit	110
5.4.2 Decoder	111
5.4.3 Adaptive threshold	112
5.5 Experimental results	114
5.5.1 Prototype implementation	114
5.5.2 Dimming support	115
5.5.3 Communication performance	118
5.6 Conclusions and discussions	119
REFERENCES	120
6 Two-way visible light communication and illumination with LEDs	123
6.1 Introduction	124
6.1.1 Related work	124
6.1.2 Contributions and organization of our work	125
6.2 System structure	126
6.3 LED transceiver front-end	128
6.4 Data transmission	130
6.4.1 PHY frame structure and coding scheme	130
6.4.2 Decoding scheme	131
6.5 Synchronization scheme	132
6.5.1 Symbol-level synchronization	133
6.5.2 Frame-level synchronization	134
6.5.3 Illumination loss and compensation	134
6.6 Experimental results	136
6.6.1 Prototype implementation	136
6.6.2 Coding performance	137
6.6.3 Synchronization performance	138
6.6.4 Communication performance	139

6.7	Conclusions and discussions	144
6.A	Rate-illumination trade-off	145
	REFERENCES	149
7	Conclusions and further research	153
7.1	Color sensing and control	154
7.2	Daylight adaptive control	156
7.3	LED-to-LED visible light communication	157
7.3.1	Unidirectional VLC and illumination with LEDs	157
7.3.2	Adaptive VLC and illumination with LEDs	158
7.3.3	Two-way VLC and illumination with LEDs	159
7.4	Recommendations for future research	160
7.4.1	Robust color control of multi-color LEDs	160
7.4.2	Occupancy sensing with LEDs	161
7.4.3	MIMO LED-to-LED VLC with multi-color LEDs	161
	REFERENCES	162
	Summary	163
	Curriculum vitae	167
	Acknowledgement	169

Chapter **1**

Introduction

1.1 Introduction

Light is one of the basic necessities of life. It is a portion of the electromagnetic (EM) waves that transport energy across space. Depending on the source, light can be categorized as: *daylight* and *artificial light*. Daylight comes from the EM radiation of the sun. It consists of EM waves in both the invisible region and visible region. The invisible component consists mainly of portions of infrared (IR) and ultraviolet (UV) light. The visible part is defined as having wavelengths in the range of 400 nm to 700 nm, between the UV light and IR light. Light is omnipresent, yet it is often under-appreciated. Light is however vital in providing visibility for humans to interact with the surrounding world.

1.1.1 Artificial light

Artificial light results from “man-made” light sources such as lamps. The early generation of electric lamps were incandescent lamps, carbon arc lamps and gas discharge lamps. These early lamp technologies used a lot of energy, had short lifespans and were expensive to produce. Driven by the need to address these issues, research programs focused on fluorescent lamp technologies in the early twentieth century. These lamps lasted longer and were much more efficient than incandescent lamps. In the latter part of the twentieth century, a breakthrough in diode physics took place showing that by simply coating blue diodes with yellow phosphor results in white light, and that white light could also be produced using a combination of red, green and blue diodes. These inventions have resulted in one of the fastest growing lighting innovations in the form of light emitting diodes (LEDs). LEDs offer substantial energy reduction and long lifetime. Although the cost of LEDs is still high, the lighting industry is working hard to improve both the quality of light and the energy efficiency while reducing their costs.

1.1.2 Solid state lighting

Solid-state lighting (SSL) refers to a type of lighting that uses semiconductor LEDs or organic light-emitting diodes (OLEDs) as sources of illumination. Compared to incandescent lighting, SSL consists of semiconductors that convert electricity into light with less heat generation and reduced energy dissipation. Also, SSL promises a longer design lifetime. Specifically, compact fluorescent lamp (CFLs) have a lifetime of about 6000 hours and thereafter fail, i.e. produce zero light output afterwards. In contrast, a LED lamp considers its “end-of-life” at 60% of its rated light output, and this lifetime is roughly 30,000 hours [1]. Among SSL technologies, the LED is becoming the preferred light source of the future

for many lighting applications. Most common “white” LEDs convert blue light from a solid-state device to provide an approximate white light spectrum using a luminescent phosphor. A combination of red, green and blue (RGB) LEDs are also used to produce white light, as well as produce a larger spectrum of colors.

In addition to energy savings and long lifetime, LED lighting opens up new opportunities within the domain of lighting, and beyond. Some of the opportunities that relate to lighting are summarized below:

1. Color control: LED technology offers the possibility of full color control over the visible light spectrum. Having excellent quality LEDs in the red, green, and blue primary colors greatly facilitates color mixing. Further, modern digital LED driver solutions support accurate color mixing by providing precise current control. LED-based color control technology has been adopted in new lighting controls and consumer electronics applications [2], [3], [4], [5].
2. Dimming control: LED sources are inherently dimmable and instantaneously controllable, and they can be readily integrated with sensor and control systems, thus enabling deep energy savings through the use of occupancy sensing, daylight harvesting, and local control of light levels [6], [7], [8], [9].
3. Visible light communication: The high-speed modulation capability of semiconductor LED light sources allows for visible light communication (VLC) while providing flicker-free illumination. With VLC, a LED light source transmits information by modulating its light output. A number of applications in interactive and networked lighting control, consumer electronics, indoor positioning and connected vehicles [10], [11], [12], [13], [14], have considered LED based VLC.

1.1.3 LEDs for illumination

Illumination may be considered to be the primary function of a LED light source. In general lighting applications, e.g. office lighting, the white light output of a LED lighting system may be controlled. Artificial light output is adapted in accordance with occupancy conditions and daylight changes in order to save energy. Substantial energy savings have been shown to be achieved by incorporating occupancy sensor and light sensor feedback in controlling the amount of artificial light output from luminaires [15]. Such controls are respectively termed occupancy controls - adapting light output depending on occupancy status, and daylight controls - adapting light output dependent on the available amount of daylight.

Such controls need to be designed while meeting norms for office lighting, e.g. as specified in European norms EN12464-1 [16]. Feedback related to occupancy and daylight is typically captured using motion sensors and light sensors respectively. A passive infrared sensor is a typical motion sensor used for occupancy control in commercial lighting systems. The presence of a user is determined as a detection from the motion sensor within a time window. Occupancy status then determines a set-point to be achieved at a light sensor. Photodetectors are typical light sensors used in commercial lighting systems. A photodetector measures the net contribution of reflected daylight and artificial light within its field-of-view. For practical reasons, the occupancy and light sensors are situated at the ceiling along with the luminaires. Using measurements from these sensors, a lighting controller determines the dimming levels of luminaires in the lighting system so as to minimize energy consumption while achieving specified illumination constraints.

In consumer applications, color control and interaction in LED lighting becomes additionally relevant. Control based on multi-color LEDs opens up the opportunity for innovative infotainment applications, especially in homes. Examples are the Philips HueTM home lighting system and Osram LightifyTM system, wherein the color and brightness of lamps may be controlled to create a particular ambience. Such control may be done from smartphones or tablets via a wireless bridge. A related example is StoryLightTM that brings Disney stories to life via interaction of an app. When a page on an e-book on a smart device is flipped, the light color of the StoryLight lamp changes to match the story. Another example is Philips AmbilightTM that enriches the television viewing experience. Multi-color LEDs are put around the rear of a TV. They are used to radiate colorful light that matches to the TV frames in real-time, filling a room with perfect ambient light.

1.1.4 LEDs for information transmission

Visible light communication refers to transmission of information by modulating a light source and reception by an optical receiver. A LED light source, on account of its fast switching and easy controllability, can be used as a VLC transmitter while providing flick-free illumination. Visible light communication, as a service beyond illumination, has recently been investigated as a means of communication to augment traditional radio communications. An example application is indoor positioning. With VLC, each luminaire in a LED lighting system sends its unique identifier that can be decoded by image processing at a user smartphone upon signal reception. Such a VLC based indoor positioning system enables sub-meter accuracy in localizing users. The luminaires provide all

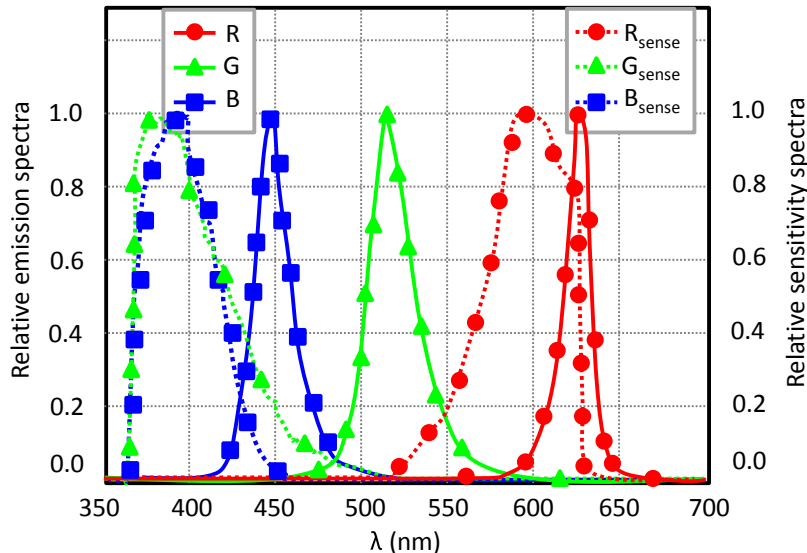


Figure 1.1: Illustration of emission and sensitivity spectra of red, green and blue LEDs at room temperature.

of the benefits of LED-based illumination, including energy savings in comparison to conventional lighting, while also providing additional localization functionality. VLC has also been considered in other applications like commissioning of lighting systems, networked lighting, contextualizing IoT data and consumer infotainment [12], [17], [18], [19].

A large body of work has focused on VLC systems using LEDs for data transmission and *dedicated* light sensors (e.g. photodetectors and cameras) as VLC receivers. In many such scenarios, VLC provides a downlink channel, the uplink channel is realized by other means such as conventional RF like WiFi [20], [21]. Alternatively, a dedicated light sensor collocated with the LED luminaire can be used as a VLC receiver, at the cost of extra sensors and complex circuitry.

1.2 LEDs for sensing

Thus far, LEDs have been used for illumination and more recently for transmitting information. We explore a new functionality - that of sensing. The use of a LED as a light sensor has long been known [22]. As a light sensor, a LED has a wavelength band specific sensitivity, in a band that is below the wavelength band over which it illuminates. This property is illustrated in Fig. 1.1, showing rela-

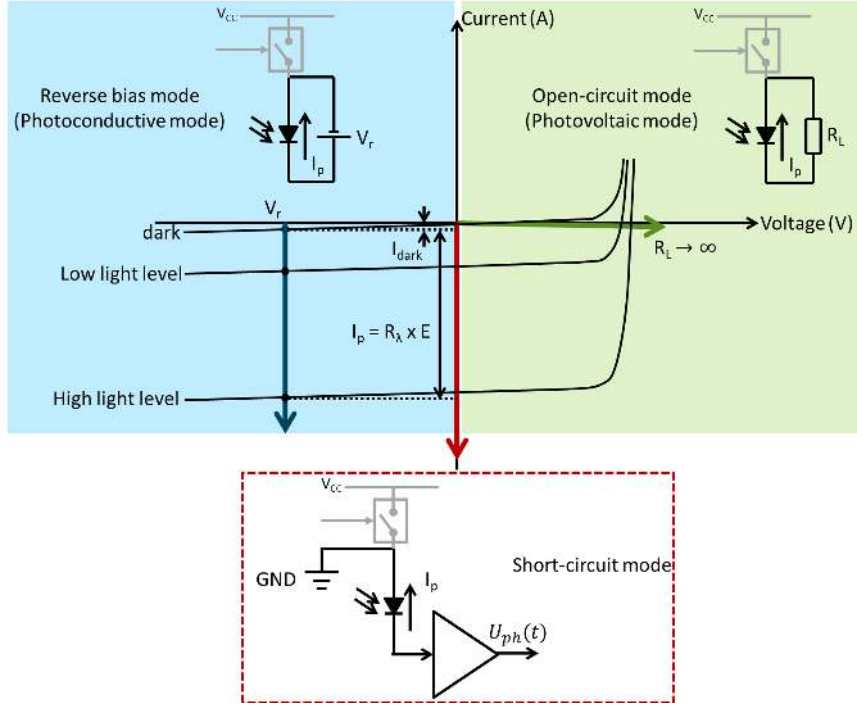


Figure 1.2: LED current-voltage characteristics and three sensing modes.

tive emission and sensitivity spectra of the RGB LEDs at room temperature [23]. The x-axis represents the visible light wavelength range in nanometer (nm). The solid lines correspond to the amplitude of emission characteristics of red, green and blue LEDs driven at a nominal forward current. The dashed lines represent the amplitude of the photosensitivity of each RGB LED chip. Both the emission and sensitivity spectra are normalized to a range between 0 and 1.

There are three modes of operation for a LED as a light sensor: open-circuit mode, short-circuit mode and reverse bias mode. These modes correspond to different phases of the LED current-voltage characteristics plot, as shown in Fig. 1.2.

1. Open-circuit mode (photovoltaic mode): in this mode, a LED is disconnected from power V_{cc} and is switched OFF. It is connected to a large load resistor in parallel, i.e. $R_L \rightarrow \infty$. This corresponds to the load line (green color) close to the x-axis, and its intersections with the current-voltage curves under different light levels give the photovoltage values. Thus, a photovoltage is measured across the load resistor R_L . In this mode, the

Table 1.1: LED as a light sensor: operation mode and linearity.

Bias	Sensing mode	Linearity
None	Photovoltaic mode	Non-linear
Zero bias	Short-circuit mode	Linear
Reverse bias	Photoconductive mode	Linear

photovoltage relates non-linearly to the measured light level. Specifically, their relation follows a logarithmic manner. An example of such a mode is a solar panel. In this mode, it conducts electricity when exposed to light at appropriate frequencies.

- Reverse bias mode (photoconductive mode): in this mode, the LED is disconnected from power V_{cc} and is reverse-biased by an external voltage V_r . This corresponds to the load line (blue color) in the third phase of the current-voltage plot. This mode benefits with linearity over a wide range:

$$I_p = R_\lambda \times E, \quad (1.1)$$

where I_p , R_λ and E are respectively the photocurrent signal, the LED responsivity and the measured light power. According to the load line, the photocurrent $I_p > 0$ under dark conditions in the absence of any ambient light ($E = 0$). Thus, the measurement in this mode is biased by a current, denoted by I_{dark} . The dark current I_{dark} is determined by the reverse saturation current, applied reverse bias voltage and absolute temperature. Further, this mode requires a reverse bias voltage that is expensive to provide in modern LED drivers.

- Short-circuit mode: in this mode, the anode pin of the LED is grounded and a circuit loop is formed. This mode corresponds to the load line (red color) on the negative y-axis with zero load resistance. The photocurrent I_p relates linearly to the measured light level E by Eq. (1.1). Further, the photocurrent signal I_p is unbiased in this case since $I_{dark} = 0$ for $E = 0$. The photocurrent I_p is amplified and transformed into a voltage signal $U_{ph}(t)$, which can be measured using a standard analog-to-digital converter (ADC).

The sensing functionality of LEDs is summarized in Table 1.1. Only when being switched OFF and with proper bias can a LED serve as a light sensor. We shall refer to such an OFF period as *sensing slot*. The LED sensing functionality can be integrated into the existing LED applications (color sensing and control, daylight adaptive control and VLC) by properly incorporating the sensing slot with the dimming waveform in two ways:

1. Time multiplexing of a dedicated sensing slot and an analog dimming waveform, which dims the LEDs by adjusting the LED current level. Specifically, dedicated OFF periods are reserved between dimming waveform for sensing functionality. The duration and frequency of the sensing slot must be designed properly to avoid perceivable flicker.
2. Time sharing of dedicated sensing slot and a pulse-width modulated waveform (PWM). In PWM dimming control applications, the control signal is in the form of a cyclic pulse-width modulated waveform. The duty cycle of the PWM waveform determines the dimming level. As a LED dims down, it can reuse the OFF period of PWM waveform to perform sensing. In VLC applications, the sensing slot can be overlapped with the OFF period of an on-off-keying symbol.

In this thesis, our main goals are therefore:

Main goals:

- (i) *To create new LED systems and applications exploiting the wavelength-sensitive sensing function of LEDs;*
- (ii) *To demonstrate feasibility of such systems by developing proof-of-concept prototypes and study their sensing and illumination performance.*

1.3 Applications with sensing LEDs

In this section, we revisit three LED-based applications: color sensing and control, daylight adaptive control and VLC. We consider integration of the LED sensing functionality in these applications.

1.3.1 Color sensing and control

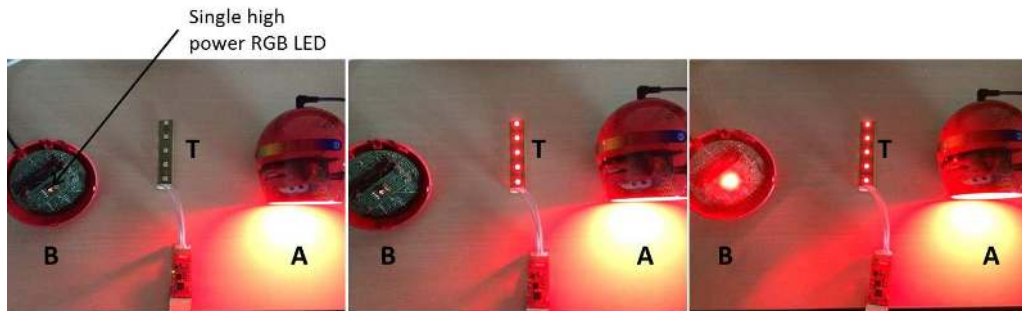
The use of LEDs in lamps is enabling new applications and products that enable users to control and interact with LED lamps in innovative ways. A simple use case is illustrated in Fig. 1.3a wherein the color coming from the screen of a smartphone is used to adapt the light output of an RGB LED lamp using a color sensing mechanism. In Fig. 1.3b, we demonstrate a *ColorTransporter* device. By default, it switches OFF to sense color emitted by a source lamp. It can pick up colors when it is brought in the proximity of the light source. It then holds this color until a user resets the sensing state using an external button. With this *ColorTransporter* device, the color can then be transported to a destination

1.3. APPLICATIONS WITH SENSING LEDS



(a) Color sensing LED luminaire adapts its color to the screen of a smart phone.

(b) ColorTransporter picks up primary colors (red, green, blue) from LED lamps.



Calibration of B & T

T picks up red color from A

T transports red color to B

(c) Interactive color control.

Figure 1.3: Color control application.

light source. The destination light source is another LED lamp, which reuses the RGB LEDs for color sensing and illumination.

The complete interactive color control application is shown in Fig. 1.3c. The application is to transport color from a source lamp A to another destination lamp B using a ColorTransporter T. In this illustration, Lamp A is a commercial LivingColor™ lamp, which outputs preset colors by mixing the light output from RGB LEDs. At the first stage, the source color of lamp A is preset to emit the desired color (red in this case) via a touch panel. Meanwhile, the lamp B and the ColorTransporter T stay at sensing state and self-calibrate by monitoring the ambient color noise for a short interval. Subsequently, when the ColorTransporter T is brought in the proximity of lamp A, it picks up the red color. The previously collected noise measurements are stored locally and used in a color estimation

step. Finally, when the ColorTransporter is brought in the proximity of lamp B, the lamp picks up the red color from device T.

This work focuses on tackling the following technical questions in such an application.

1. How to sense multiple colors within a reasonable sensing range?
2. How to sense without causing flicker in illumination?
3. How to maintain low complexity of the described interactive LED lamps?

In this thesis, our first sub-goal is therefore:

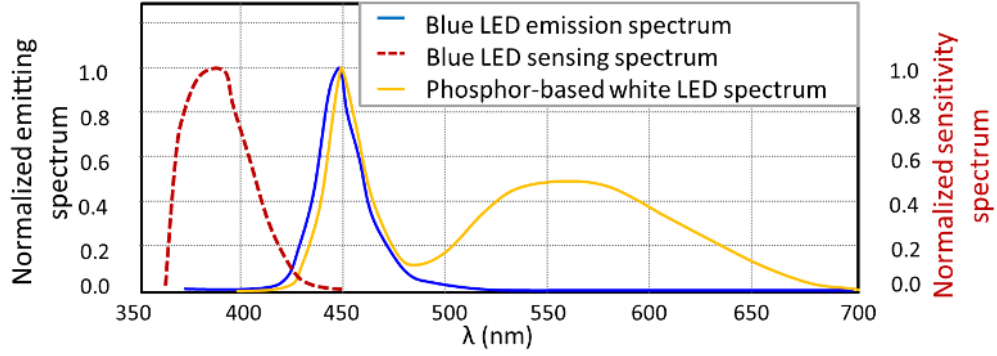
Sub-goal 1: *To develop a prototype system that uses RGB LED wavelength selectivity to provide new ways of light interaction, without dedicated light sensors.*

Our work addresses the main technical questions in the following ways.

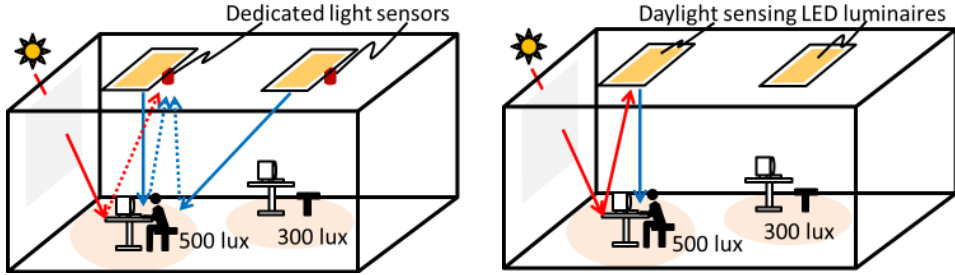
1. The sensing function is realized with red, green and blue LEDs as three band-pass optical filters and sensors, and devising color estimation algorithms using these RGB channel measurements. Such an approach is feasible given the wavelength selectivity of RGB LEDs shown by their sensing spectra in Fig. 1.1.
2. The source and destination lamps implement a driving protocol, wherein illumination and sensing are performed in a time-division multiplexing manner. Switching between two modes is scheduled such that the light output is modulated at a rate higher than twice the main frequency, resulting in color sensing without causing illumination flicker.
3. The proposed LED lamps can sense and control color without dedicated light sensors, which saves the cost of having a dedicated sensor. Further, the photovoltaic sensing mode is selected resulting in minor hardware modification limited to adding one extra load resistor. As such, the color sensing functionality comes mainly in the form of software algorithms that can be integrated into a micro-controller unit.

1.3.2 Daylight adaptive control

In the previous color sensing application, RGB LEDs were reused to sense over the full color band. In this section, we explore the LED sensitivity in the *invisible* light band. Specifically, we consider the phosphor-converted white (pc-white) LED consisting of a blue LED die and yellow phosphor material. Its emitting and sensing spectra are depicted in Fig. 1.4a.



(a) Emitting and sensing spectra of phosphor-converted white LEDs.



(b) Benchmark daylight adaptive lighting control system with LED luminaires and dedicated photodetectors.

(c) Proposed daylight adaptive lighting control system with daylight-sensing LED luminaires.

Figure 1.4: Daylight adaptive lighting control application.

The normalized emitting spectrum of the pc-white LED consists of blue luminescence and long phosphorescence [24], as shown by the solid line in Fig. 1.4a. The dashed line in Fig. 1.4a shows the normalized sensing spectrum of the blue LED [23], with an about 70 nm shift towards the UV band. Note that the UV-A wavelength range is also within the pass-band (370 nm to 450 nm) of the blue LED sensing spectrum. Therefore, the blue color LED is sensitive to UV-A light. In addition, UV-A light can pass through phosphor with very limited radiation energy loss [25]. Thus, the pc-white LED is also sensitive to UV-A light. In general, UV light is not purposely emitted by any artificial light. Therefore, the measured photocurrent of a pc-white LED is primarily due to daylight contribution.

We now integrate the daylight sensing functionality of pc-white LED into daylight control lighting systems. In such systems, the light output from the luminaires is adapted to produce artificial illumination in accordance with chang-

ing daylight such that the net achieved illumination level meets the desired value while saving energy [8], [26].

In state-of-art daylight adaptive lighting control systems [9], [15], the achieved illumination level is monitored using dedicated light sensors collocated with luminaires as depicted in Fig. 1.4b. The control target is to reach illumination level at workspaces in accordance with office lighting norms [16], e.g. at least 500 lux in occupied space and 300 lux elsewhere. The desired illumination level at workspaces is mapped to target set-points to be achieved at the light sensor via a night-time calibration phase. Using feedback in the form of light sensor measurements, the lighting controller seeks to achieve the target set-points by adapting the dimming levels of the luminaires. Such photodetector based lighting control systems have the following drawbacks:

1. The use of additional photodetectors leads to extra cost and installation complexity.
2. A photodetector measures both the daylight and artificial light from all the luminaires that is reflected back within its field-of-view. Thus, careful design of closed-loop feedback control is required to obtain the dimming levels of the luminaires so as to maintain stability and system responsiveness to illumination changes.
3. Under environmental changes, the reflectance values of the surfaces beneath the photodetectors may vary with time. Examples of such changes are the movement of desks and placement of a bright object on a dark desk surface. This leads to more (or less, depending on the reflectance of the objects) artificial light as well as daylight being reflected back at the light sensor. As a result, this can lead to large deviations in the achieved illumination level from the desired value [27], [28].

Fig. 1.4c depicts the proposed daylight adaptive lighting system with daylight-sensing LED luminaires. An array of pc-white LEDs can perform the dual functionality of illumination and daylight sensing, obviating the need of additional light sensors. Reusing pc-white LEDs for daylight-adaptive control improves system performance. Specifically, the pc-white LEDs do not sense any artificial light, which makes the proposed system more robust to artificial reflectance changes in comparison to a photodetector-based closed-loop lighting control system. Integration of daylight sensing functionality brings a list of technical challenges:

1. How to design the driver waveform for pc-white LEDs for both daylight sensing and illumination, without causing flicker?

2. How to design the lighting control law to update the luminaire light output to adapt to daylight measurements?

In this thesis, our second sub-goal is therefore:

Sub-goal 2: *To develop a daylight adaptive LED lighting system that can sense and adapt to daylight changes, without using dedicated light sensors.*

Our work addresses the main technical questions in the following ways.

1. We adopt typical PWM signals to drive pc-white LEDs and reuse the OFF period of each PWM cycle for daylight sensing. Thus, the illumination is flicker-free as long as the PWM frequency is above twice the main frequency.
2. An iterative control method is proposed to update the dimming level of a daylight sensing luminaire. At each iteration, the luminaire estimates daylight contribution and artificial light contribution by neighboring luminaires using calibration functions and implements an open-loop control law to update self-contribution. The control algorithm targets on achieving a desired illumination at the workspace under each daylight sensing luminaire.

1.3.3 LED-to-LED visible light communication

In addition to color and daylight, LEDs are also used to receive data coming from VLC transmitters. A VLC link is feasible only if the sensing spectrum of receiving LEDs overlaps partially with the emitting spectrum of transmitting LEDs. Such a system can achieve LED-to-LED VLC, without the use dedicated light sensors. In this section, we integrate the LED sensing functionality into the VLC application.

We begin with the VLC transmitter. The opportunity to send data by VLC has largely arisen because of the widespread use of LED light sources. LEDs are semiconductor devices that switch at high speed, which allows for embedding information into the light output. The modulation is done fast enough that it is not perceivable to human eyes. Thus, VLC transmitters can provide a light output suitable also for illumination purpose. One example is the VLC transmitter in the state-of-art LiFi technology [29], wherein the same visible light energy used for illumination is also used for communication.

Fig. 1.5 illustrates an exemplary setup of an indoor VLC system. A VLC modem is collocated with a LED lamp and embeds information into the light output, while dimming the light output within a certain range. Note that the shown setup provides a unidirectional VLC link, which is dedicated for the broadband

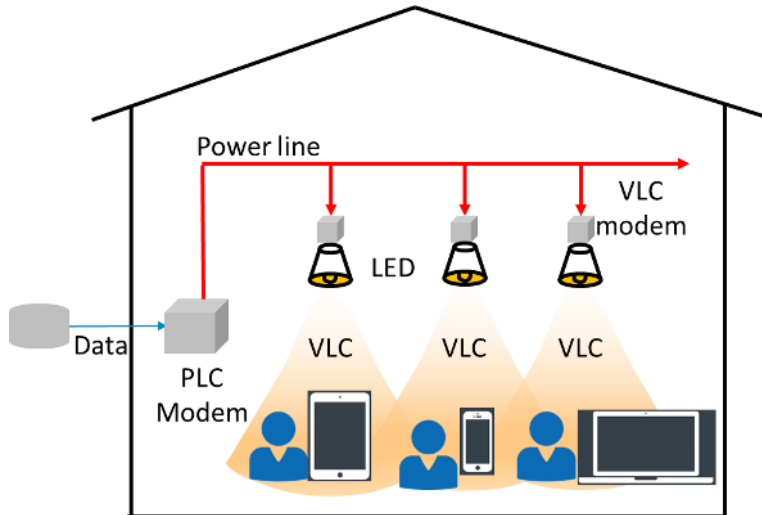


Figure 1.5: Integration of indoor visible light and power line communication Systems.

downlink, i.e., from LED lamps to VLC receivers. The transmitted information could be a luminaire identifier for an indoor positioning application, or multimedia data streams for infotainment applications. By interfacing with a backbone network such as a power line communication (PLC) system, much like the role Ethernet plays towards WiFi, a VLC transmitter can draw information from a remote database. VLC receivers can typically be consumer electronic devices such as a smartphone, tablet and laptop.

A number of works have considered VLC systems with LED-based VLC transmitters and *dedicated* light sensors as VLC receivers [10], [30], [31], [32], [33], [34], [35], [36], [37], [38], [39]. In [10], the performance of a LED lighting system that provides illumination and VLC with photodetectors was analyzed. The possibility of achieving high data rates with VLC were shown in [30], [32], [37], [38], [39]. A hybrid communication protocol for mixing camera communication with faster modulation designed for photodetectors was considered in [33]. However, none of these LED transmitters can be used in a LED-to-LED VLC application. This is because the transmission waveforms in these prior works do not support the possibility of sensing, while providing illumination. In the VLC system depicted in Fig. 1.5, the VLC receiver can reuse the LED screen of a smart device or a LED flashlight to receive VLC data. Meanwhile, the LED screen or LED flashlight can provide steady light output for illumination.

This raises the following technical challenges for transmitter and receiver

design in such LED-to-LED VLC systems.

1. How should the information be encoded at the LED VLC transmitter that facilitates decoding at the LED receiver?
2. How should the transmitted optical signal be designed to realize VLC and flicker-free illumination?
3. How does the decoding mechanism work, given that the LED is used for both VLC reception and providing illumination?
4. How does synchronization work in such VLC systems?

Our third sub-goal in this research is therefore:

Sub-goal 3: *To provide flick-free illumination and unidirectional visible light communication between two LED devices, without dedicated light sensors.*

These challenges are addressed in our proposed one-way VLC system.

1. At the VLC transmitter, data is encoded using a standard run-length limited (RLL) code with carefully added redundancy. The redundant bits provide information of the carrier signal waveform, which facilitates decoding.
2. The VLC data is carried by a PWM signal, whose frequency is higher than twice the main frequency for flicker-free illumination.
3. The receiver modulates a dedicated sensing bit sequence using on-off-keying and uses the OFF periods for VLC reception. The run-length number of the sensing bit sequence is limited to avoid illumination flicker. Decoding is realized with threshold detection plus waveform analysis schemes.
4. The proposed decoding scheme does not require tight synchronization between the VLC transmitter and receiver. While receiving VLC data, the receiver can also measure the phase offset in real time and adapt to keep it within a preset range. It saves the dedicated synchronization intervals required by state-of-art LED-to-LED VLC systems [40], [41].

After commissioning the VLC system, we need to calibrate the VLC receiver so that the VLC data can be correctly decoded from a certain distance from the VLC transmitter under a stable ambient light condition. Such a calibration scheme requires a fixed communication distance between the two LED devices and that the ambient light be constant. The effective communication range of

such a system is limited by device portability and ambient light changes (e.g. slow daylight variations). This raises the following technical challenges for transmitter and receiver design in such LED-to-LED systems.

1. How should the receiver support adaptive threshold decoding?
2. How should the transmitter allocate the transmission power for better communication performance?

Our fourth sub-goal in this research is therefore:

Sub-goal 4: *To enhance the unidirectional visible light communication with an adaptive VLC transmitter and receiver.*

These challenges are addressed in our proposed adaptive VLC system.

1. At the receiver, the impact of communication distance and ambient light level changes on threshold values is measured and compensated.
2. At the transmitter side, we consider a weighted combination of a PWM signal and a redundant RLL encoded OOK signal. The weights are designed to achieve a target dimming level and enhance the transmit signal-to-noise ratio (SNR).

The dual use of LEDs for illumination and sensing can be treated as being analogous to transmitting and receiving information in a two-way channel [42]. Limited work has been done on bi-directional LED-to-LED VLC systems, except for [43], [44] that considered medium access control protocols. The performance of two-way VLC system has not been studied in literature yet. The design of two-way LED-to-LED VLC system brings new technical challenges.

1. How to encode data such that simultaneous decoding is feasible?
2. How should the LED devices be synchronized for two-way VLC?
3. What are the communication and illumination trade-offs in such a system?

Our fifth sub-goal in this research is therefore:

Sub-goal 5: *To provide flicker-free illumination and full-duplex visible light communication between two LED devices, without dedicated light sensors.*

These challenges are addressed in our proposed two-way VLC system.

1. We select Manchester coding and on-off keying for transmission, which can support simultaneous decoding using a simple exclusive-OR operation.

2. We propose symbol and frame level synchronization schemes. Phase-offset between two LED devices is measured during a dedicated time interval reserved at the frame head, using the OFF slot of an OOK symbol. Phase-offset compensation is executed once per frame, which provides tight synchronization for intra-frame two-way VLC.
3. We formulate the trade-off between the system rate and illumination in such a system and show that the combination of Manchester coding and OOK modulation achieves optimum system performance in the sense of balancing the rate-illumination trade-off.

1.4 Outline of the thesis

In this section, we summarize the scope and key contributions of each chapter.

Chapter 2 addresses the first sub-goal in this thesis. We present a LED system prototype with source and destination LED lamps and a LED array as a color transporter device. A color sensing and illumination driver protocol is presented so that the LED lamps can sense color while illuminating without perceivable flicker. A similar protocol is used at the LED array transporter device with the additional use of hardware triggers to have the device either in sensing or illumination mode. Two color estimation methods are presented to map the measured voltage on the red, green and blue channels to a sensed color. Evaluation of the proposed methods shows that it is possible to detect colors efficiently, with a few exceptional cases. The proposed RGB LED system is especially attractive in consumer applications where sensor placement is either cumbersome or expensive. The contents of Chapter 2 have been published in [5].

Chapter 3 addresses the second sub-goal in this thesis. We present a LED luminaire prototype that can provide the dual functionality of illumination and daylight sensing. The proposed solution avoids the extra cost and installation complexity involved in current lighting control systems that use external photodetectors. Two driver protocols for performing daylight sensing while providing illumination are proposed. One of these protocols incurs only a nominal loss in light output and was chosen for implementation in the luminaire prototype. An open loop control method based on the sensed daylight values and knowledge of calibration is used to obtain the dimming levels of the luminaires to adapt to daylight and occupancy changes. The performance of the proposed daylight sensing lighting control system is compared with a photodetector based system and shown to be more robust in the presence of reflectance changes in the environment. The contents of Chapter 3 have been published in [45].

Chapter 4 addresses the third sub-goal in this thesis. We present the design and evaluation of a prototype system with two LED devices for asynchronous communication while also providing illumination. The devices use the LEDs themselves for data transmission and reception, without additional dedicated light sensors. The built prototype is evaluated in terms of BER and illumination flicker performance. We show that reliable communication at a rate of a few kbps is achievable, with illumination flicker comparable to conventional PWM dimming. The contents of Chapter 4 have been published in [46].

In Chapter 5, we present the design of a LED-based VLC system where the LED is used for adaptive VLC transmission and reception, as well as for illumination. In the proposed design, the modulation index at the transmitter and calibration detection thresholds at the receiver are adapted to changes in ambient illumination conditions and limited LED device portability. Using an experimental prototype system, we show that an increase of almost 30% in reliable communication distance is obtained in comparison to a non-adaptive VLC system in Chapter 4. The contents of Chapter 5 are in review [47].

Chapter 6 addresses the fifth sub-goal in this thesis. We present the design of a two-way VLC system with LEDs used as transceivers and also for illumination. We show that for time-slotted VLC, the combination of Manchester coding and OOK modulation achieves the optimum trade-off between system rate and illumination. This scheme is used for data transmission along with a simple XOR decoding scheme at the receiver. At the receiver, OFF periods in the signal waveform are used for retrieving the transmitted information. We implement a proof-of-concept LED prototype system with a low-power single red LED and show that data rates in the order of kbps are achieved at a distance of a few tens of cm. For luminaires with hundreds of LEDs, a communication range in the order of a few meters becomes feasible. The contents of Chapter 6 have been published in [48].

Finally, Chapter 7 summarizes the conclusions and results of this thesis. We also discuss future research challenges and directions.

1.5 Publications of the author

1.5.1 Journal Publications

1. S. Li and A. Pandharipande, "LED-Based Color Sensing and Control," *IEEE Sensors Journal*, vol. 15, no. 11, pp. 6116-6124, November 2015.
2. S. Li, A. Pandharipande and F. M. J. Willems, "Daylight Sensing LED Lighting System," *IEEE Sensors Journal*, vol. 16, no. 9, pp. 3216-3223, May 2016.
3. S. Li, A. Pandharipande and F. M. J. Willems, "Unidirectional visible light communication and illumination with LEDs," *IEEE Sensors Journal*, vol. 16, no. 23, pp. 8617-8626, December 2016.
4. S. Li, A. Pandharipande and F. M. J. Willems, "Adaptive visible light communication and illumination with LEDs," *IEEE Journal on Selected Areas in Communications Special Issue on Localisation, Communication and Networking with VLC*, in review.
5. S. Li, A. Pandharipande and F. M. J. Willems, "Two-way visible light communication and illumination with LEDs," *IEEE Transactions on Communications*, vol. 65, no. 2, pp. 740-750, February 2017.

1.5.2 Conference Publications

1. A. Pandharipande and S. Li, "Illumination and light sensing for daylight adaptation with an LED array: Proof-of-principle," *39th Annual Conference of the IEEE Industrial Electronics Society (IECON)*, pp. 6081-6086, Vienna, 2013.
2. S. Li and A. Pandharipande, "Color sensing and illumination with LED lamps," *IEEE Fourth International Conference on Consumer Electronics Berlin (ICCE-Berlin)*, pp. 1-2, Berlin, 2014.
3. S. Li, A. Pandharipande and F. M. J. Willems, "Redundant run-length limited encoding for two-way visible light communication," *42nd Annual Conference of the IEEE Industrial Electronics Society (IECON)*, pp. 4706-4712, Florence, 2016.

1.5.3 Other Publications

1. D. Caicedo, S. Li and A. Pandharipande, “Smart lighting control with workspace and ceiling sensors,” *Lighting Research & Technology*, February 2016.
2. S. Li and A. Pandharipande, “Networked Illumination Control With Distributed Light-Harvesting Wireless Sensors,” *IEEE Sensors Journal*, vol. 15, no. 3, pp. 1662-1669, March 2015.
3. A. Pandharipande and S. Li, “Light-Harvesting Wireless Sensors for Indoor Lighting Control,” *IEEE Sensors Journal*, vol. 13, no. 12, pp. 4599-4606, December 2013.
4. X. Chen, S. Li, J. Schleifer, T. Coenen, A. Chattopadhyay, G. Ascheid and T. G. Noll, “High-level modeling and synthesis for embedded FPGAs,” *Design, Automation & Test in Europe Conference & Exhibition (DATE)*, pp. 1565-1570, France, 2013.
5. X. Chen, A. Minwegen, Y. Hassan, D. Kammler, S. Li, T. Kempf, A. Chattopadhyay and G. Ascheid, “FLEXDET: Flexible, Efficient Multi-Mode MIMO Detection Using Reconfigurable ASIP,” *IEEE 20th Annual International Symposium on Field-Programmable Custom Computing Machines (FCCM)*, pp. 69-76, Toronto, 2012.

1.5.4 Patent Applications

1. S. Li and A. Pandharipande, “Two-way communication using LEDs”, filed.
2. S. Li and A. Pandharipande, “Controlling a light source”, filed.
3. S. Li and A. Pandharipande, “Commissioning in a lighting system”, filed.

REFERENCES

- [1] A. Sayigh, *Sustainability, Energy and Architecture - Chapter 7 - The LED Lighting Revolution*. Boston: Academic Press, 2013.
- [2] F. C. Wang, C. W. Tang, and B. J. Huang, “Multivariable robust control for a red-green-blue LED lighting system,” *IEEE Transactions on Power Electronics*, vol. 25, no. 2, pp. 417–428, 2010.
- [3] S. Muthu, F. J. P. Schuurmans, and M. D. Pashley, “Red, green, and blue LEDs for white light illumination,” *IEEE Journal of Selected Topics in Quantum Electronics*, vol. 8, no. 2, pp. 333–338, 2002.
- [4] S. Afshari, S. Mishra, A. Julius, F. Lizarralde, J. D. Wason, and J. T. Wen, “Modeling and control of color tunable lighting systems,” *Energy and Buildings*, vol. 68, Part A, pp. 242–253, 2014.
- [5] S. Li and A. Pandharipande, “LED-based color sensing and control,” *IEEE Sensors Journal*, vol. 15, no. 11, pp. 6116–6124, November 2015.
- [6] D. Caicedo and A. Pandharipande, “Distributed illumination control with local sensing and actuation in networked lighting systems,” *IEEE Sensors Journal*, vol. 13, no. 3, pp. 1092–1104, 2013.
- [7] S. Tanaka, M. Yoshikata, M. Miki, and T. Hiroyasu, “An evolutionary optimization algorithm to provide individual illuminance in workplaces,” in *IEEE International Conference on Systems, Man and Cybernetics*, pp. 941–947, October 2009.
- [8] N. van de Meughevel, A. Pandharipande, D. Caicedo, and P. van den Hof, “Distributed lighting control with daylight and occupancy adaptation,” *Energy and Buildings*, vol. 75, pp. 321–329, 2014.
- [9] A. Pandharipande and D. Caicedo, “Smart indoor lighting systems with luminaire-based sensing: A review of lighting control approaches,” *Energy and Buildings*, vol. 104, pp. 369–377, 2015.
- [10] T. Komine and M. Nakagawa, “Fundamental analysis for visible-light communication system using LED lights,” *IEEE Transactions on Consumer Electronics*, vol. 50, no. 1, pp. 100–107, February 2004.
- [11] H. Yang, T. C. W. Schenk, J. W. M. Bergmans, and A. Pandharipande, “Enhanced illumination sensing using multiple harmonics for LED lighting

- systems,” *IEEE Transactions on Signal Processing*, vol. 58, no. 11, pp. 5508–5522, 2010.
- [12] G. Corbellini, K. Aksit, S. Schmid, S. Mangold, and T. R. Gross, “Connecting networks of toys and smartphones with visible light communication,” *IEEE Communications Magazine*, vol. 52, no. 7, pp. 72–78, July 2014.
- [13] M. Yasir, S. W. Ho, and B. N. Vellambi, “Indoor positioning system using visible light and accelerometer,” *Journal of Lightwave Technology*, vol. 32, no. 19, pp. 3306–3316, 2014.
- [14] C. B. Liu, B. Sadeghi, and E. W. Knightly, “Enabling vehicular visible light communication (V2LC) networks,” in *Proceedings of the Eighth ACM International Workshop on Vehicular Inter-networking*, pp. 41–50, 2011.
- [15] A. Pandharipande and D. Caicedo, “Adaptive illumination rendering in LED lighting systems,” *IEEE Transactions on Systems, Man, and Cybernetics: Systems*, vol. 43, no. 5, pp. 1052–1062, 2013.
- [16] European Committee for Standardization, “EN 12464-1:2002. Light and lighting. Lighting of work places. Part 1: Indoor work places,” 2002.
- [17] K. Warmerdam, A. Pandharipande, and M. Zuniga, “Visible light communications for sensing and lighting control,” *IEEE Sensors Journal*, vol. 16, no. 17, pp. 6718–6726, September 2016.
- [18] S. Li and A. Pandharipande, “Commissioning in a lighting system,” Patent, filed.
- [19] K. Warmerdam, A. Pandharipande, and D. Caicedo, “Connectivity in IoT indoor lighting systems with visible light communications,” *2015 IEEE Online Conference on Green Communications (OnlineGreenComm)*, pp. 47–52, 2015.
- [20] S. Shao, A. Khreishah, M. B. Rahaim, H. Elgala, M. Ayyash, T. D. C. Little, and J. Wu, “An indoor hybrid WiFi-VLC internet access system systems,” in *IEEE 11th International Conference on Mobile Ad Hoc and Sensor Systems*, pp. 569–574, 2014.
- [21] M. Ayyash, H. Elgala, A. Khreishah, V. Jungnickel, T. Little, S. Shao, M. Rahaim, D. Schulz, J. Hilt, and R. Freund, “Coexistence of WiFi and LiFi toward 5G: concepts, opportunities, and challenges,” *IEEE Communications Magazine*, vol. 54, no. 2, pp. 64–71, February 2016.

-
- [22] F. M. Mims, *Siliconconnections: Coming of Age in the Electronic Era*. New York, NY, USA: McGraw-Hill, 1986.
- [23] C. Martiny and M. Wendt, “Intrinsic sensing and color control of multiLED lamp-modules,” *Philips Research, Eindhoven, The Netherlands, Tech. Rep. PR-TN 2006/00195*, 2006.
- [24] E. Schubert, *Light-Emitting Diodes*. Cambridge University Press, 2006.
- [25] Y. Zhu, N. Narendran, and Y. Gu, “Investigation of the optical properties of YAG: Ce phosphor,” in *6th International Conference on Solid State Lighting*, p. 63370S, September 2006.
- [26] G. Boscarino and M. Moallem, “Daylighting control and simulation for LED-based energy-efficient lighting systems,” *IEEE Transactions on Industrial Informatics*, vol. 12, no. 1, pp. 301–309, 2016.
- [27] D. Caicedo, A. Pandharipande, and F. M. J. Willems, “Light sensor calibration and dimming sequence design in distributed lighting control systems,” in *IEEE 11th International Conference on Networking, Sensing and Control*, pp. 344–349, 2014.
- [28] D. Caicedo, A. Pandharipande, and F. M. J. Willems, “Illumination gain estimation and tracking in a distributed lighting control system,” in *IEEE Conference on Control Applications*, pp. 1650–1655, 2014.
- [29] D. Tsonev, S. Videv, and H. Haas, “Light fidelity (Li-Fi): towards all-optical networking,” *Proc. SPIE*, vol. 9007, no. 2, pp. 1–10, 2013.
- [30] H. Elgala, R. Mesleh, and H. Haas, “Indoor optical wireless communication: potential and state-of-the-art,” *IEEE Communications Magazine*, pp. 56–62, September 2011.
- [31] P. H. Pathak, X. Feng, P. Hu, and P. Mohapatra, “Visible light communication, networking, and sensing: A survey, potential and challenges,” *IEEE Communications Surveys Tutorials*, vol. 17, no. 4, pp. 2047–2077, 2015.
- [32] Z. Wu, J. Chau, and T. Little, “Modeling and designing of a new indoor free space visible light communication system,” *16th European Conference on Networks and Optical Communications*, pp. 72–75, July 2011.
- [33] N. Rajagopal, P. Lazik, and A. Rowe, “Hybrid visible light communication for cameras and low-power embedded devices,” in *Proceedings of the 1st*

- ACM MobiCom Workshop on Visible Light Communication Systems*, pp. 33–38, July 2014.
- [34] L. Klaver and M. Zuniga, “Shine: A step towards distributed multi-hop visible light communication,” *IEEE 12th International Conference on Mobile Ad Hoc and Sensor Systems*, pp. 235–243, 2015.
- [35] H. Yang and A. Pandharipande, “Full-duplex relay VLC in LED lighting triangular system topology,” *6th International Symposium on Communications, Control and Signal Processing*, pp. 85–88, May 2014.
- [36] H. Yang and A. Pandharipande, “Full-duplex relay VLC in LED lighting linear system topology,” *Annual Conference of the IEEE Industrial Electronics Society*, pp. 6075–6080, November 2013.
- [37] Y. Wang, L. Tao, X. Huang, J. Shi, and N. Chi, “8-Gb/s RGBY LED-based WDM VLC system employing high-order CAP modulation and hybrid post equalizer,” *IEEE Photonics Journal*, vol. 7, no. 6, pp. 1–7, December 2015.
- [38] J. J. D. McKendry, D. Massoubre, S. Zhang, B. R. Rae, R. P. Green, E. Gu, R. K. Henderson, A. E. Kelly, and M. D. Dawson, “Visible-light communications using a CMOS-controlled micro-light-emitting-diode array,” *Journal of Lightwave Technology*, vol. 30, no. 1, pp. 61–67, January 2012.
- [39] R. X. G. Ferreira, E. Xie, J. J. D. McKendry, S. Rajbhandari, H. Chun, G. Faulkner, S. Watson, A. E. Kelly, E. Gu, R. V. Penty, I. H. White, D. C. O’Brien, and M. D. Dawson, “High bandwidth GaN-based micro-LEDs for multi-Gb/s visible light communications,” *IEEE Photonics Technology Letters*, vol. 28, no. 19, pp. 2023–2026, October 2016.
- [40] S. Schmid, G. Corbellini, S. Mangold, and T. R. Gross, “An LED-to-LED visible light communication system with software-based synchronization,” *IEEE Globecom Workshops*, pp. 1264–1268, December 2012.
- [41] S. Schmid, G. Corbellini, S. Mangold, and T. R. Gross, “Continuous synchronization for LED-to-LED visible light communication networks,” *3rd International Workshop in Optical Wireless Communications*, pp. 45–49, September 2014.
- [42] C. E. Shannon, “Two-way communication channels,” *Proceedings of the Fourth Berkeley Symposium on Mathematical Statistics and Probability*, pp. 611–644, 1961.

-
- [43] Q. Wang, D. Giustiniano, and D. Puccinelli, “An open-source research platform for embedded visible light networking,” *IEEE Wireless Communications*, vol. 22, no. 2, pp. 94–100, 2015.
- [44] Q. Wang and D. Giustiniano, “Intra-frame bidirectional transmission in networks of visible LEDs,” *IEEE/ACM Transactions on Networking*, vol. 24, no. 6, pp. 3607–3619, December 2016.
- [45] S. Li, A. Pandharipande, and F. M. J. Willems, “Daylight sensing LED lighting system,” *IEEE Sensors Journal*, vol. 16, no. 9, pp. 3216–3223, May 2016.
- [46] S. Li, A. Pandharipande, and F. M. J. Willems, “Unidirectional visible light communication and illumination with LEDs,” *IEEE Sensors Journal*, vol. 16, no. 23, pp. 8617–8626, December 2016.
- [47] S. Li, A. Pandharipande, and F. M. J. Willems, “Adaptive visible light communication and illumination with LEDs,” *IEEE Journal on Selected Areas in Communications Special Issue on Localisation, Communication and Networking with VLC*, in review.
- [48] S. Li, A. Pandharipande, and F. M. J. Willems, “Two-way visible light communication and illumination with LEDs,” *IEEE Transactions on Communications*, vol. 65, no. 2, pp. 740–750, February 2017.

Chapter 2

LED-based color sensing and control*

New ways of light interaction are being enabled with the advent of light-emitting diodes (LEDs). In this chapter, we describe a LED system with LED lamps and a LED array, where the LED array is used to sense color of a source lamp and then transport it to a destination lamp to adapt its color. We present a design prototype of the LED lamps and the LED array in order to realize the dual function of color sensing and illumination. A driving protocol is proposed such that color sensing may be performed, without causing an additional flicker during illumination. Depending on the wavelength selectivity of the LED devices, two methods for color estimation are proposed. Experimental results are presented to evaluate the performance of the proposed estimation method.

*This chapter has been published as: S. Li and A. Pandharipande, "LED-based color sensing and control", *IEEE Sensors Journal*, vol. 15, no. 11, pp. 6116-6124, November 2015.

2.1 Introduction

Lighting is witnessing a major technology shift towards semiconductors with the adoption of light emitting diodes (LEDs). New applications in lighting controls, information systems, consumer electronics, smartphones have emerged based on LEDs [1], [2], [3], [4], [5], [6], [7], [8]. Besides illumination applications, LEDs have also been used for other functions like communication and sensing [9], [10], [11], [12], [13]. In this paper, we explore the dual use of LEDs for color sensing and illumination. We consider a LED system wherein a color is sensed by a LED array device from a lamp, and then transported to another LED lamp to adapt its color. Such a system opens up new lighting applications towards interactions between lamps, toys, electronic devices etc. with embedded LEDs.

We consider a LED system with two RGB (red, green, blue) LED lamps, where one is designated as a source lamp and the other, the destination lamp. By controlling the power to each RGB LED, different colors can be generated. This may be achieved using three software pulse width modulated (PWM) signals generated by a micro-controller unit (MCU). We consider a LED array with RGB LEDs as a color transporter device that is used to sense color from the source lamp and transport it to the destination lamp, where the color of the lamp can be adapted. This color sensing and control application is realized by making use of LEDs as wavelength band selective sensors.

The use of a LED as a light sensor has long been known [14]. As a sensor, a LED has a wavelength band specific sensitivity, in a band that is below the wavelength band over which it illuminates. This property is illustrated in Fig. 2.1, showing relative emission and sensitivity spectra of an RGB LEDs at room temperature [15]. The x-axis represents the visible light wavelength range in nanometer (nm). The solid lines correspond to the amplitude of emission characteristics of red, green and blue LEDs driven at a particular nominal forward current of 350 mA. The dashed lines represent the amplitude of the photosensitivity of each RGB LED chip. Both the emission and sensitivity spectra are normalized to a range between 0 and 1.

2.1.1 Related work on color sensing

In [16], a reflective color sensor was proposed with RGB LEDs and a photo-transistor. Color information was frequency-modulated by modulating the RGB LEDs at different frequencies. Color detection was performed using a dedicated photo-transistor and three bandpass filters. In [17], a color sensor for detecting eight different colors within a working distance up to 5 cm was presented. Colors were generated by turning on RGB LEDs one at a time. A dedicated photo-

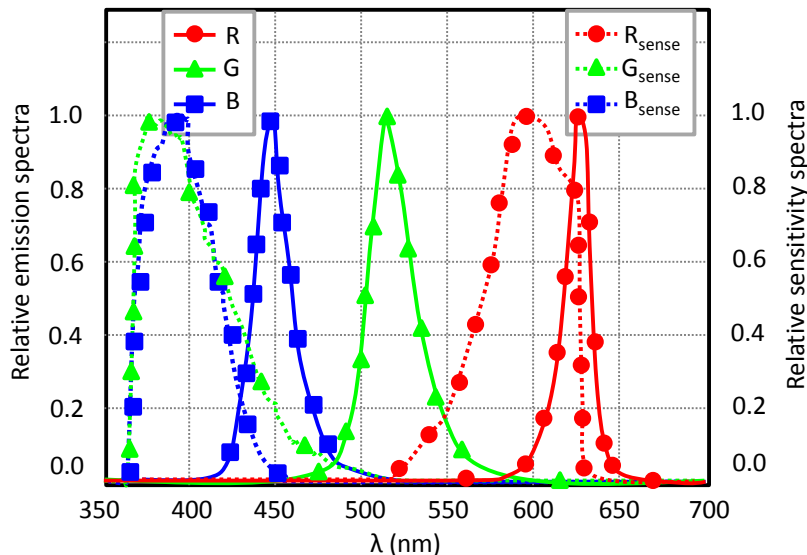


Figure 2.1: Illustration of emission and sensitivity spectra of red, green and blue LEDs at room temperature.

transistor was used to make binary decisions on the reflected light from each RGB channel. These previous works used a single dedicated sensor to separate the three color components from RGB LEDs and used some form of modulation at the transmitter. In [18], an integrated filter-less BiCMOS sensor for detecting the three RGB primary colors was presented. The sensor consists of three different pn junctions aligned vertically on one silicon, each of which collects generated photo-carriers at the corresponding layer. Color was determined by relating light wavelengths to layer depths. These works considered the use of a dedicated color sensor which may be prohibitive in certain applications due to cost or sensor placement constraints.

2.1.2 Contributions of this work

A design prototype of a LED system with LED lamps and LED array is presented, wherein the LED array senses color from an illuminating source lamp and transports it to adapt the color of an illuminating destination lamp. The prototype LED lamp and LED array consist of an emitting path and a sensing path controlled by a MCU. A driving protocol is designed for color sensing under the constraint that the signaling does not result in additional perceivable flicker in illumination mode. A color estimation method using a calibrated sensitiv-

ity matrix is considered for detecting arbitrary colors. In the case where the sensitivity matrix is not well-conditioned, estimation is achieved using a discrete wavelet transform (DWT) based method. In comparison, in our earlier work [19], a simple threshold algorithm was used to detect primary colors. The proposed LED system does not require an additional dedicated color sensor to realize the sensing function, and is thus attractive in applications where sensor placement is expensive and cumbersome.

2.2 LED system arrangement and prototype design

The LED lamp system consists of a source RGB LED lamp, a color transporter device and a destination RGB LED lamp. In the considered application scenario, a LED array is used to sense and pick the color from an illuminating source lamp. The LED array then illuminates at the picked color and transports the color in order to adapt the color of a destination lamp. We now describe a prototype design implementation of the source/destination LED lamps and the color transporter device.

2.2.1 Source and destination LED lamps

In Fig. 2.2, we illustrate the block diagram of the RGB LED lamp. It consists of four major parts: the MCU, current regulator, sensing path and RGB LED. Three general purpose input/output (GPIO) pins Lit_R, Lit_G and Lit_B on the MCU are configured to output logic-level driving signals that switch on or off the corresponding LEDs when the output logic is high or low respectively. The current regulator block implements a constant current source and operates in two modes: illumination and sensing. In illumination mode, it boosts the incoming logic high control signal high enough to light the RGB LED. In sensing mode, it translates a logic low control signal to high impedance which isolates the RGB LED from the current source and allows a sensing path to measure the small photocurrent. The sensing path is built for two purposes. Firstly, it isolates the MCU from the current regulator in order to protect the GPIO pins ADC_R, ADC_G and ADC_B. Secondly, it forms an RC circuit for photocurrent measurements. The detailed structures of the current regulator and sensing path are shown in Fig. 2.3.

Current Regulator

The current regulator consists of three transistors and four resistors. The gate pin of the logic-level N-channel MOSFET Q1 is controlled by MCU pin Lit_R in

2.2. LED SYSTEM ARRANGEMENT AND PROTOTYPE DESIGN

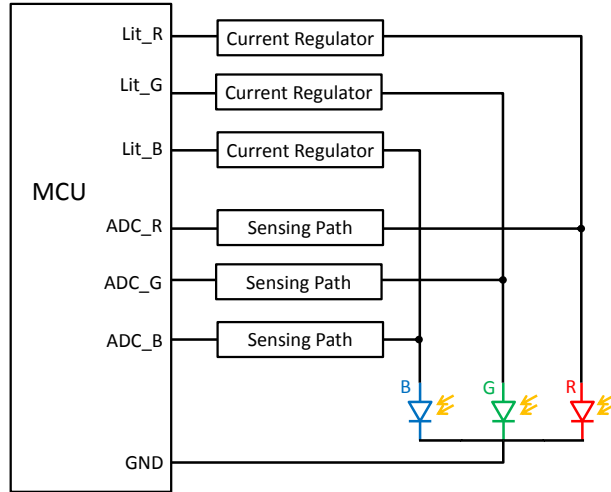


Figure 2.2: Luminaire block diagram.

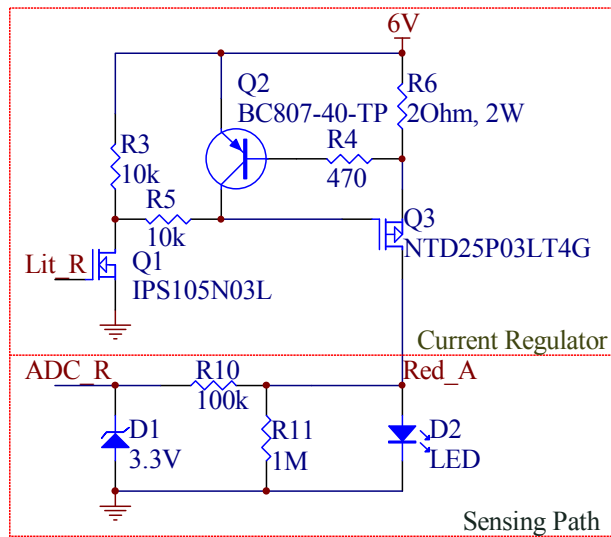


Figure 2.3: Structure of current regulator and sensing path.

Fig. 2.2. The drain of the P-channel MOSFET Q3 is routed to the anode pin of the red LED chip. The power supply must exceed $V_f + V_{be}$ in order to forward-bias the red LED. Here V_f is the forward voltage of the LED chip operating at nominal current, and V_{be} is the base-emitter voltage drop of transistor Q2.

When the current regulator is in illumination mode, pin Lit_R outputs a high

logic which switches on Q1 and Q3 and connects resistor R6 and red LED in series. The forward current I_f flowing through the red LED is regulated by resistor R6 and, for the implementation illustrated in Fig. 2.3, may be calculated as $I_f = V_{be}/R6 = 0.7 \text{ V}/2 \text{ Ohm} = 350 \text{ mA}$. When the current regulator is in sensing mode, pin Lit_R outputs a low logic to switch off Q1. Q3 gate is pull-up to Vcc (6 V) via resistors R3 and R5, switching Q3 off since its gate-source is not reverse-biased. The current regulator output is limited by the zero gate voltage drain current of Q3 which is in the order of 10-100 nA. Thus, the red LED is isolated from the current source which makes photocurrent measurements feasible by the sensing path.

Sensing Path

The sensing path consists of one zener-diode and two resistors. Pin ADC_R is mapped to an analog-to-digital converter (ADC) input channel on MCU. The functionality of the sensing path can be explained in two modes. In illumination mode, the ADC channel is deactivated and configured as an input GPIO pin. The input voltage is clamped with a 3.3 V zener diode D1 in order to protect the GPIO pins from being damaged by a large value of V_f . Further, a current limit resistor R10 is connected in series to prevent the GPIO pin from being damaged by a large value of I_f . In sensing mode, the ADC channel is activated. The LED chip is zero-biased to operate at photovoltaic mode with the excited photocurrent driving a load resistor R11. The voltage across resistor R11 is measured by the ADC and used as input to the color estimation algorithm.

2.2.2 Color transporter device

The color transporter device is built with an array of RGB LEDs connected in parallel. LEDs in parallel structure require higher forward current which can be brought by a smaller R6 in the current regulator. The advantage of this configuration is a better resolution without the need of an additional operational amplifier because of increased total capacitance. However, poor emission performance caused by asymmetrical forward current on each LED chip is expected. Each RGB LED consists of three LED chips with red, green and blue color in one package. The cathodes of these LEDs are combined and connected to the MCU in a similar way to the sensing path depicted in Fig. 2.3. The anode pins of LEDs with same color are combined and connected with the MCU using wires or current regulators depending on the required driving power of the LEDs. The color transporter device is further equipped with a switch to indicate whether it needs to pick up a color, or needs to transport a color.

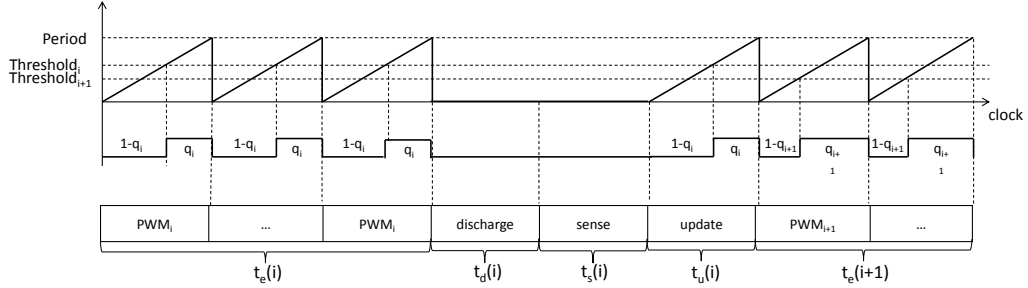


Figure 2.4: Color sensing and illumination Protocol.

2.3 Driving Protocol

In this section, we present the driving protocol for the LED array transporter device and lamps to sense and emit light. The driving protocol is identical across the source and destination lamps, and differs from the LED transporter device in that a certain hardware trigger is used in the latter.

Fig. 2.4 illustrates the LED driver protocol wherein sensing is performed in a time-division multiplexing manner, comprising of an emitting period (t_e), decoupling period (t_d), sensing period (t_s) and updating period (t_u), all constituting one cycle. Let us consider the red channel (same design applies to blue and green channels). In cycle i , over the emitting period $t_e(i)$, the red LED is forward-biased to emit red light. Over the decoupling period $t_d(i)$, the red LED is decoupled and starts to discharge through resistors R_{10} and R_{11} (see Fig. 2.3). The coupled noise component from the blue and green channels is introduced during period $t_e(i)$, where part of the emitting light is reflected back to the LED chips by the LED and lamp packaging. The period $t_d(i)$ ensures that the signal-to-noise ratio is high enough for the ADC to measure the real incident light spectrum in a subsequent period $t_s(i)$. With the ADC measurements, the MCU continues with an updating period $t_u(i)$ which is composed of few $t_e(i)$ periods. During period $t_u(i)$, MCU calculates a new threshold using a color estimation algorithm and updates duty cycle of signal on pin Lit_R before entering the next cycle. This driving protocol is followed at the source and destination lamps without any hardware triggers.

In the case of the LED transporter device, a hardware trigger is inserted at the end of each $t_e(i)$ period. It is implemented by means of an external button. By default, the transporter device continuously works at $t_e(i)$ period, emitting an estimated color combination. One hardware trigger allows the device to enter the sensing mode (periods $t_d(i)$ and $t_s(i)$) and pick up a color from a source lamp (periods $t_u(i)$ and $t_e(i+1)$). Until the next hardware trigger, the device stays at

period $t_e(i+1)$ and keeps illuminating the sensed color, in which case the sensing period is set to zero. This mode ensures that the device does not change color unintentionally when brought in proximity with another lamp. In this mode, a destination LED lamp can sense and pick up the transported color from the LED device.

It is known that the modulation rates higher than twice the main frequency (100 or 120 Hz) do not cause perceivable flicker to the user. The LED off time during $t_d(i)$ and $t_s(i)$ must hence be shorter than 10 ms or 8.3 ms (depending on the main frequencies) so that the modulation is not perceived by a user, and also to achieve the required forward average current by increasing the current amplitude. Thus, the upper bound of $t_d(i) + t_s(i)$ is given by

$$t_d(i) + t_s(i) < \frac{1}{f_0} \cdot \left(1 - \frac{I_f}{I_{f,max}}\right), \quad (2.1)$$

where f_0 is the minimum required modulation frequency before flicker occurs, I_f the average forward current required by the lamp to achieve a certain illuminance level and $I_{f,max}$ is the rated maximum forward current of each LED chip. On the other hand, $t_d(i)$ must exceed the discharge time of the RC loop (see Fig. 2.3) to remove self-coupling and $t_s(i)$ must exceed the ADC setup time to complete photocurrent measurements. Thus, the lower bound for the sensing period is

$$t_d(i) + t_s(i) \geq \tau_0 + \tau_1 + \sigma_0, \quad (2.2)$$

where τ_0 is the discharge time required by the anode pin voltage to drop to 0, and τ_1 is the charge time required by the incident light to raise anode voltage from 0 to a stable level. The constant σ_0 corresponds to the maximum time required by the ADC to quantize measurements. Note that τ_0 is determined by resistors $R10$ and $R11$, and τ_1 is determined by $R11$. Thus, $R10$ and $R11$, as design parameters, may be adjusted to ensure that the sensing period is short enough to limit flicker. By decreasing $R10$ and $R11$, both τ_0 and τ_1 are reduced. However, more current is sunk by MCU pins and ground during period $t_e(i)$, which degrades the energy efficiency of the current regulator. The values of $R10$ and $R11$ listed in Fig. 2.3 balance this trade-off.

2.4 Color estimation method

It is feasible to detect primary colors (red, green and blue) using a simple threshold algorithm as considered in our earlier work [19]. However detecting an arbitrary color is not straightforward. In this section, we propose two color estimation methods. One is based on a sensitivity matrix. The other one is based on the

DWT and peak detection. Depending on the emission and sensitivity spectra of LED devices, one of these methods is used.

2.4.1 Sensitivity matrix based color estimation method

In the RGB color space, sensing arbitrary colors requires estimation of primary color portions based on the observations by sensing elements. We introduce a sensitivity matrix \mathbf{S} based on RGB channel measurements v_R , v_G and v_B at a reference state. The reference state means a primary color is generated by a corresponding LED (red, green or blue) operating at a nominal forward current from a certain distance under conditions of room temperature. The resulting \mathbf{S} is a 3×3 square matrix written as

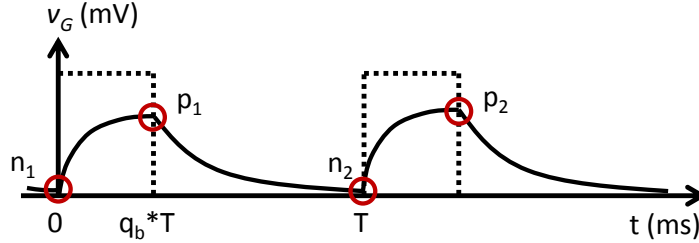
$$\mathbf{S} = \begin{bmatrix} s_{R,r} & s_{R,g} & s_{R,b} \\ s_{G,r} & s_{G,g} & s_{G,b} \\ s_{B,r} & s_{B,g} & s_{B,b} \end{bmatrix}. \quad (2.3)$$

Each element $s_{i,j}$ corresponds to the sensitivity of the i channel on the j colored light, where $i \in \{R, G, B\}$ and $j \in \{r, g, b\}$. For example, element $s_{R,g}$ indicates the wavelength selectivity of the R channel exposed to pure green light at the reference state.

Assume an incident light with red, green and blue light components modulated by square waves with a constant frequency but at different duty cycles q_r , q_g and q_b . Under the condition of a dark environment, the R channel measurement v_R equals the superposition of the red, green and blue light contributions on R channel. It is calculated by the multiplication of the first row of matrix \mathbf{S} with a column vector $\mathbf{q} = [q_r, q_g, q_b]^T$. The G and B channel measurements are given similarly. The resulting model may be written in matrix form as follows

$$\mathbf{v} = \mathbf{S}\mathbf{q} + \mathbf{n}, \quad (2.4)$$

where $\mathbf{v} = [v_R, v_G, v_B]^T$ is the vector containing ADC measurements on the RGB channels, and \mathbf{n} is a vector containing voltages if the source of the intended color was in off state, thus capturing effect of the ambient environment. The vector \mathbf{n} is obtained during a calibration stage by collecting N measurements on each RGB channel. Sample number N is determined by rounding up the product of the PWM cycle duration T in seconds and the ADC sampling frequency f_s in Hz. By averaging the ADC measurements on each color channel, the effect of the ambient light environment over each channel is obtained. This influence is canceled from the averaged N measurements $\mathbf{v}[i]$ with $i = 1, \dots, N$. The estimated duty cycle vector $\hat{\mathbf{q}}$ can then be obtained as a solution to the following constraint optimization problem,


 Figure 2.5: G-channel observation over $2T$ slot.

$$\hat{\underline{q}} = \min_{\substack{\underline{q} \\ 0 \leq \underline{q} \leq 1}} \left\| \frac{1}{N} \sum_{i=1}^N \underline{v}[i] - \underline{n} - \underline{S}\underline{q} \right\|^2, \quad (2.5)$$

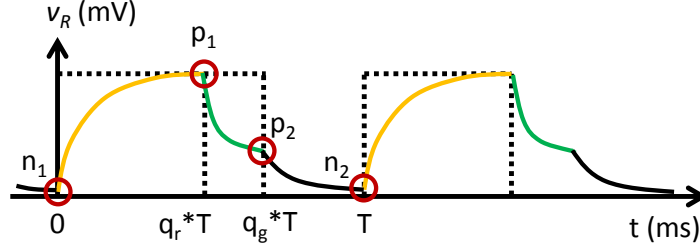
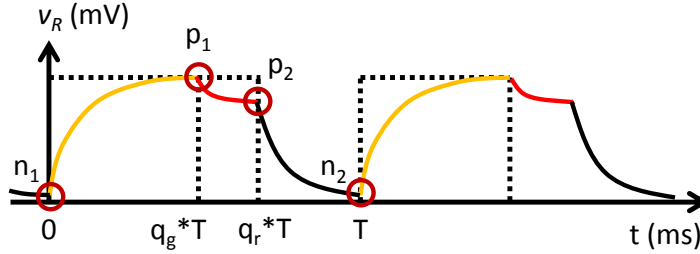
where the inequality constraint $0 \leq \underline{q} \leq 1$ indicates that each component of \underline{q} lies between 0 and 1. A solution to the above constrained quadratic optimization problem may be found using algorithms like the interior-point method [20], and efficient algorithms exist that allow for implementation on a micro-controller [21, 22].

In practice, an upper triangular matrix \underline{S} is observed due to the wavelength band selectivity of RGB LEDs chips. The row vectors of \underline{S} matrix must be linearly independent for (2.4) to have a unique solution. Violation of this condition will make the method inapplicable. In such a situation, we propose a solution to obtain \hat{q}_r and \hat{q}_g directly from observation \underline{v}_R using a wavelet analysis technique.

2.4.2 DWT based color estimation method

In the proposed method, we apply discrete wavelet analysis on N observations $\underline{v}[1] \cdots \underline{v}[N]$ in order to discover the transient points that correspond to the falling and raising edges of transmitted PWM square waves. The duty cycle \underline{q} is then estimated by the ratio of transient point position to the PWM cycle duration N .

We now detail this method and start with the estimation of q_b . Consider the illustration in Fig. 2.5. The solid line corresponds to the G channel measurements v_G (mV) of a light sensing lamp over a duration $2T$. The dashed line indicates the PWM square wave applied on a blue LED of a light emitting lamp in the t_e stage. During period $0 < t \leq q_b \cdot T$, the blue LED is switched on and v_G increases. For $q_b \cdot T < t \leq T$, the blue LED is switched off and v_G starts to decrease. Due to the integrator formed by the RC sensing path on each RGB channel, we observe a triangular wave. The wave transient is characterized by singular points n_1 , p_1 , n_2 and p_2 . Within a single T period, we find a n-p-n type of pattern and


 Figure 2.6: R-channel observation over $2T$ slot (case1: $q_r < q_g$).

 Figure 2.7: R-channel observation over $2T$ slot (case2: $q_r > q_g$).

formulate the estimation as

$$\hat{q}_b = \frac{t_{p_1} - t_{n_1}}{T}, \quad (2.6)$$

where t_{p_1} , t_{n_1} , t_{p_2} and t_{n_2} denote the sample indices of each singular point. A robust approach to locate the singular points is by applying wavelet analysis on the observed triangular wave. In our approach, we use the 1st-order Haar DWT [23] which results in four distinct peaks. Two positive peaks provide locations of p_1 and p_2 . Two negative peaks give locations of n_1 and n_2 .

In Fig. 2.6, we illustrate the R-channel response to combined red and green light under the condition of $q_r < q_g$. During the period $0 < t \leq q_r \cdot T$, both red and green LEDs are switched on to emit yellow light. As a response, voltage v_R increases from point n_1 to reach a first peak p_1 . For $q_r \cdot T < t \leq q_g \cdot T$, the red LED is switched off and voltage v_R decreases to reach a second peak p_2 . Considering the green light is still on, the p_2 value is positive. Finally for $q_g \cdot T < t \leq T$, both red and green LEDs are switched off, resulting in a decreasing voltage v_R to zero. As such, the R channel response is found to follow a n-p-p-n pattern with four singular transient points. Performing a 1st-order Haar DWT on signal v_R , we find two positive peaks (p_1 , p_2) and two negative peaks (n_1 , n_2).

In Fig. 2.7, we consider the case $q_r > q_g$ and find that the R channel response also follows the n-p-p-n pattern. For both patterns, the PWM cycle duration T

can be calculated by $t_{n_2} - t_{n_1}$. However, it is not straightforward to relate p_1 and p_2 to the falling edge of two PWM square waves. We solve this problem using the sensitivity matrix elements $s_{R,r}$ and $s_{R,g}$. For a RC circuit with a constant τ , the steady state period starts from 4τ . Assuming $t_{p_1} - t_{n_1} > 4\tau$, $t_{p_2} - t_{p_1} > 4\tau$ and $t_{n_2} - t_{p_2} > 4\tau$, the voltages corresponding to points p_1 , p_2 and n_2 reach their steady state values. Based on the signal model in (2.4), those steady state values are respectively $s_{R,r} + s_{R,g}$, $s_{R,g}$, 0 for the first case, and $s_{R,r} + s_{R,g}$, $s_{R,r}$, 0 for the second case. The estimation is then given as

$$\begin{aligned}\hat{q}_r &= \begin{cases} \frac{t_{p_1} - t_{n_1}}{T}, & \text{if } |1 - \frac{\Delta l}{l_1}| \leq |1 - \frac{\Delta l}{l_2}| \\ \frac{t_{p_2} - t_{n_1}}{T}, & \text{otherwise,} \end{cases} \\ \hat{q}_g &= \begin{cases} \frac{t_{p_2} - t_{n_1}}{T}, & \text{if } |1 - \frac{\Delta l}{l_1}| \leq |1 - \frac{\Delta l}{l_2}| \\ \frac{t_{p_1} - t_{n_1}}{T}, & \text{otherwise,} \end{cases}\end{aligned}\quad (2.7)$$

where $\Delta l = \frac{v_{p_1} - v_{p_2}}{v_{p_2} - v_{n_2}}$, $l_1 = \frac{s_{R,r}}{s_{R,g}}$ and $l_2 = \frac{s_{R,g}}{s_{R,r}}$. In practice, the RC charging and discharging curves are distorted by ambient noise, resulting in unwanted peaks after wavelet analysis. For better estimation resolution, observations \underline{v} are smoothed by processing through a filter f . Selection of the filter f is discussed in the next section.

2.5 Experimental results

In this section, we first describe the experimental setup with the designed prototypes. The generation of sensitivity matrix \mathbf{S} during the calibration stage and DWT pre-processing is then described. Finally, we evaluate the performance of the two proposed color estimation methods.

2.5.1 Implementation of designed prototypes

The designed prototypes of the source and destination RGB lamps are shown in Figs. 2.8a and 2.8c. The circuit implementation of the source and destination lamps are identical; the circuit board of the destination lamp is shaped to fit into a circular lamp package. The MCU, current regulator and sensing path are placed on side A of the board. A single RGB LED is placed in the middle of the other side B. The RGB LED lamps are implemented by a single Cree XLamp[®] MC-E color LED. Red, green, royal blue and white LEDs are packed into one package. Each LED chip operates at a nominal current of 350 mA and is individually addressable. The MCU is implemented by an MSP430F2274 micro-processor

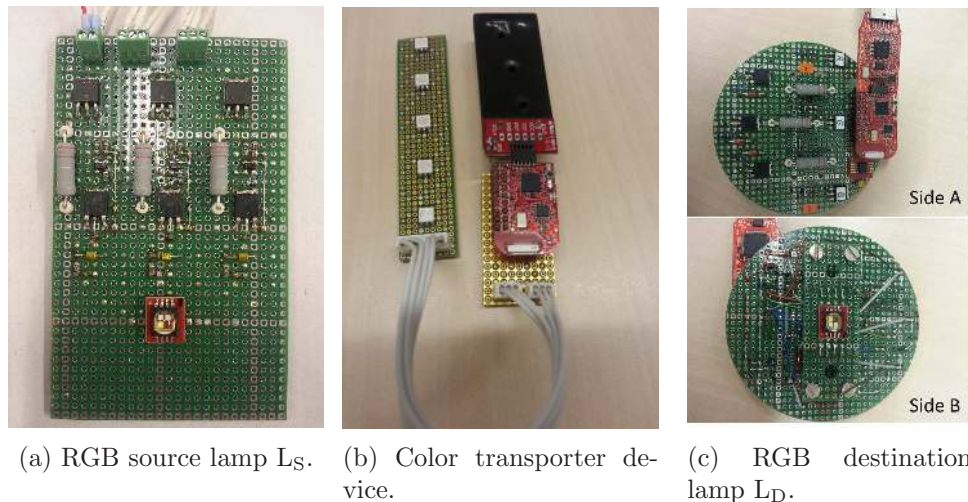


Figure 2.8: Designed prototypes.

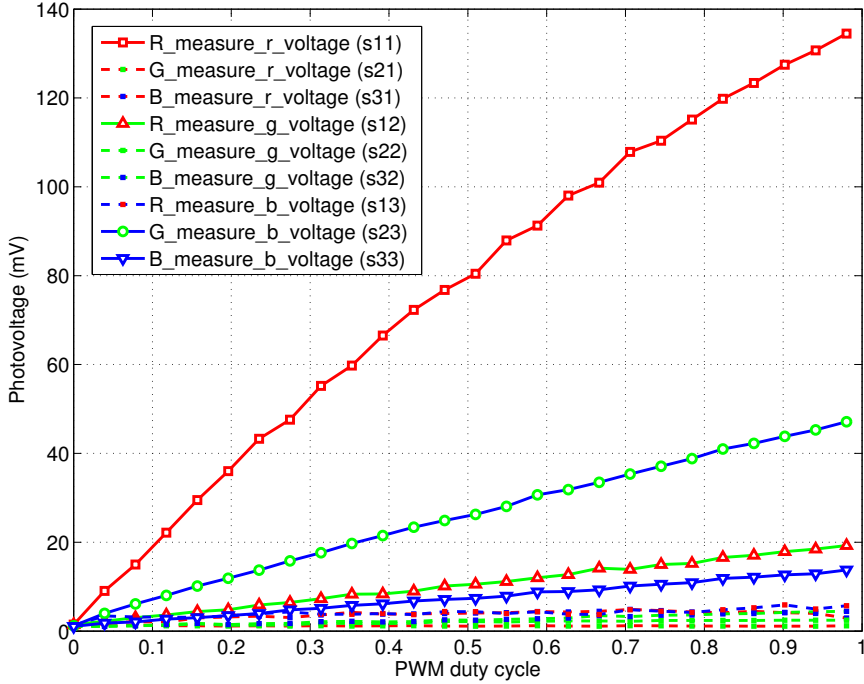
with two timers. Three compare registers are programmed to implement PWM efficiently without consuming central processing unit resources. It benefits with a real-time system running color estimation algorithm during the update stage t_u . The output of the color estimation algorithm is used to update the three compare registers for color adaptation.

The designed prototype of the color transporter device is shown in Fig. 2.8b. It consists of a linear array of five RGB LEDs. The driving protocol and sensing algorithm are implemented on a portable eZ430-RF2500T target board. The RGB LEDs are arranged in a parallel array configuration, operating at a nominal forward current of 30 mA. These mid-power LEDs are directly driven by the GPIO ports of the MCU. An interruptible push button is included on the target board for user switching and is dedicated to switching the LED array between sensing and illumination modes.

2.5.2 Sensitivity matrix generation

Two sensitivity matrices are involved in the considered applications. Matrix \mathbf{S}_1 characterizes sensitivity of the color transporter to light emitted by a source RGB lamp L_S . Matrix \mathbf{S}_2 specifies the sensitivity of a destination RGB lamp L_D to light emitted by the color transporter. Both matrices are generated in a similar way.

We take the sensitivity matrix \mathbf{S}_2 as an example. It is obtained during a dark-state calibration stage. Lamp L_D and the color transporter are spaced at


 Figure 2.9: Matrix \mathcal{S}_2 generated at different sensing ranges.

a certain distance facing each other. The color transporter is programmed to only emit light and the Lamp L_D is dedicated to sensing light. Both MCUs are connected to a computer via serial ports. A Matlab testbench, running on the computer, communicates with the two ends by sending a preset PWM duty cycle vector \underline{q} to the color transporter, and receives the corresponding ADC measurements \underline{v} from the Lamp L_D . Three consecutive \underline{q} vectors form a scaled identity matrix. The scaling factor is the preset duty cycle for each red, green and blue LED chips. As such, only one LED chip is emitting light at a time.

In Fig. 2.9, we show the voltage measurements given by increasing the duty cycle vector from 0 in steps of $\frac{50}{255}$. Although the light intensity and propagation distance follow an inverse-square law, in a small distance range, the light intensity may be approximated to fall linearly with the distance. As such, the impact of sensing range on sensitivity matrix can be studied by simply scaling the testing duty cycle. At each PWM duty cycle, nine voltage measurements are collected, forming a complete matrix corresponding to a certain sensing distance. We chose

nine ADC measurements at PWM duty cycle of $\frac{250}{255}$ to form the matrix \mathbf{S}_2 . Further, matrix \mathbf{S}_2 is subtracted by the small offset at origin (about 1 mV) such as to approximate the slope of each curve. The resulting matrix \mathbf{S}_2 is given by

$$\mathbf{S}_2 = \begin{bmatrix} 135.2 & 19.5 & 6.0 \\ 0.9 & 2.1 & 47.6 \\ 2.6 & 3.5 & 14.4 \end{bmatrix}. \quad (2.8)$$

The matrix \mathbf{S}_1 is found in a similar way and is given as

$$\mathbf{S}_1 = \begin{bmatrix} 138.1 & 50.1 & 0.6 \\ 0.1 & 92.8 & 277.6 \\ 0.4 & 0.5 & 50.2 \end{bmatrix}. \quad (2.9)$$

Note that the $s_{G,g}$ element of matrix \mathbf{S}_2 is small and that \mathbf{S}_2 is ill-conditioned. In this case, the DWT based method is used at the destination lamp L_D for color estimation. For the color transporter, however, the implemented green LED chip is sufficiently sensitive to the green light from lamp L_S . As such, we can choose the constrained optimization approach in (2.5) for color estimation.

2.5.3 Pre-processing of DWT based method

In this section, we explain the pre-processing stage of the DWT based method with an example. The color transporter is programmed to emit a preset color specified by $\underline{\mathbf{q}} = [\frac{100}{255}, \frac{200}{255}, \frac{50}{255}]^T$. At the target lamp L_D , we estimate $\hat{\underline{\mathbf{q}}}$ using the DWT method.

Fig. 2.10 shows $2N$ samples measured by each RGB channel at the target lamp L_D during daytime. The resulting curves are noisy and are smoothed before applying DWT. We select a digital smoothing filter f as a Gaussian filter which is widely used in image edge detection [24]. The coefficients of filter f are given by

$$f[k] = \frac{1}{\sqrt{2\pi}\sigma} e^{-\frac{k^2}{2\sigma^2}}, \quad (2.10)$$

where σ is the standard deviation and $k = 1, \dots, K$. We chose $\sigma = 0.25$ and the window size $K = 8$. The filtered signal is then processed by the 1st-order Haar DWT with the resulting coefficients shown in Fig. 2.11. Based on coefficient c_R , a n-p-p-n pattern is clearly recognized and estimation is done following (2.7) as

$$\begin{aligned} \hat{q}_r &= \frac{t_{p1} - t_{n1}}{t_{n2} - t_{n1}} = \frac{92 - 62}{142 - 62} = 0.375 \approx \frac{96}{255}, \\ \hat{q}_g &= \frac{t_{p2} - t_{n1}}{t_{n2} - t_{n1}} = \frac{127 - 62}{142 - 62} = 0.8215 \approx \frac{207}{255}. \end{aligned} \quad (2.11)$$

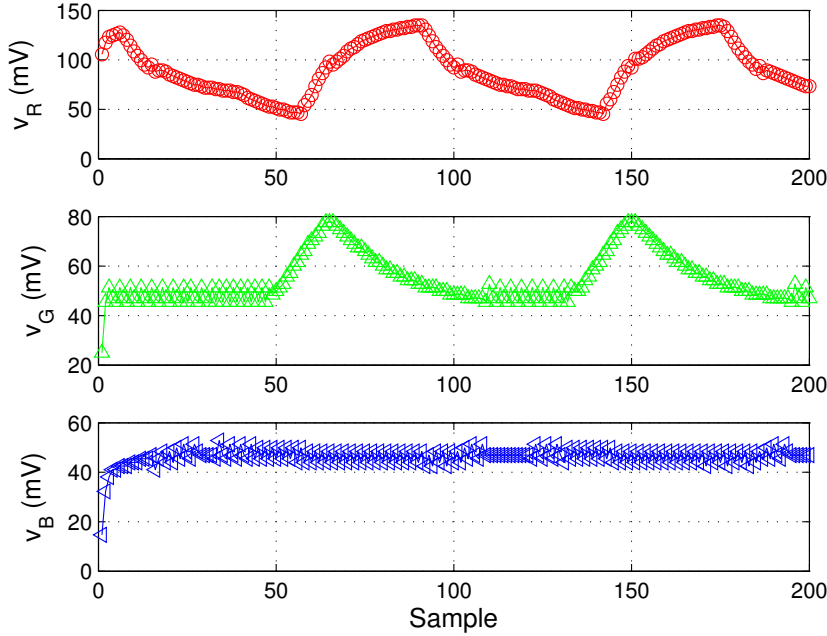


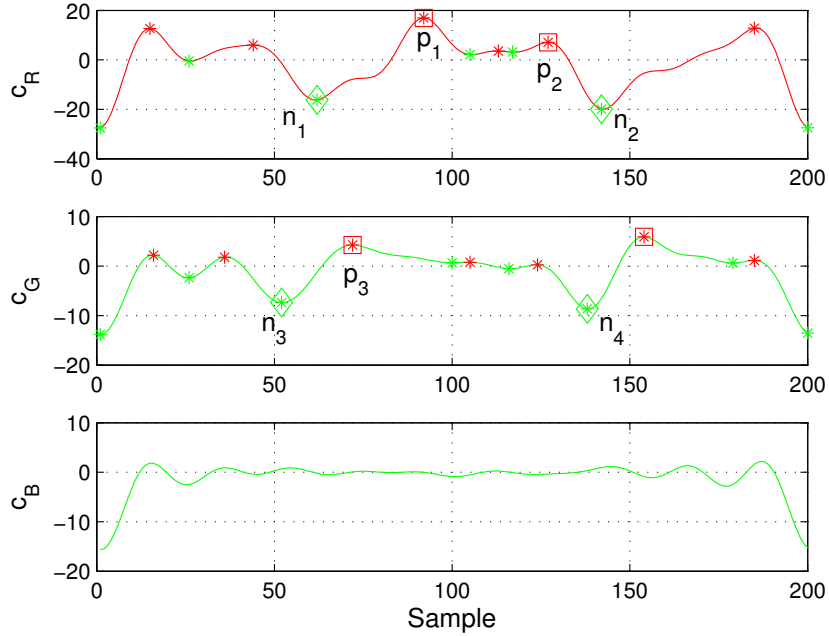
Figure 2.10: Noisy ADC measurements by RGB channels.

Based on coefficient c_G , a n-p-n pattern is observed and the blue color component is estimated using (2.6) as

$$\hat{q}_b = \frac{t_{p3} - t_{n3}}{t_{n4} - t_{n3}} = \frac{72 - 52}{138 - 52} \approx 0.2326 \approx \frac{59}{255}. \quad (2.12)$$

2.5.4 Estimation performance

In order to evaluate the performance of proposed color estimation methods, an estimation error metric has to be determined. In the conventional RGB color space, each component contains both the color information along with the luminance information. To eliminate the effect of variant sensing range on brightness changes, separation of luminance from chrominance is required. Color models such as the normalized color rgb as well as the saturation S and hue H are all invariant to the viewing direction, object geometry and illumination [25]. We choose the normalized color rgb for its simplicity and formulate the estimation error vector as


 Figure 2.11: 1st-order Haar DWT coefficients.

$$\begin{aligned}
 \underline{e} &= |\underline{q}_N - \hat{\underline{q}}_N|, \\
 \underline{q}_N &= \frac{1}{q_r + q_g + q_b} \cdot \underline{q}, \\
 \hat{\underline{q}}_N &= \frac{1}{\hat{q}_r + \hat{q}_g + \hat{q}_b} \cdot \hat{\underline{q}}.
 \end{aligned} \tag{2.13}$$

With the exemplary test vector $\underline{q} = [\frac{100}{255}, \frac{200}{255}, \frac{50}{255}]^T$ and the DWT based estimation $\hat{\underline{q}} = [\frac{96}{255}, \frac{207}{255}, \frac{59}{255}]^T$, an error vector is calculated as $[e_r, e_g, e_b]^T = [0.0205, 0.0004, 0.0201]^T$ for the corresponding RGB channels.

We first evaluate the performance of the sensitivity matrix based method. The color transporter utilizes (2.5) to estimate color that is emitted by the source lamp L_S . In Fig. 2.12, we show the estimation errors when receiving combined red and green light. At lamp L_S , the blue light duty cycle q_b is preset to be 0. The duty cycles q_r and q_g respectively increases from 0 to approach 1 at steps of $\frac{50}{255}$. As such, 36 cubes are observed and are colored by the corresponding RGB color code $[q_r \times 255, q_g \times 255, q_b \times 255]$. The estimation errors e_r , e_g and e_b of

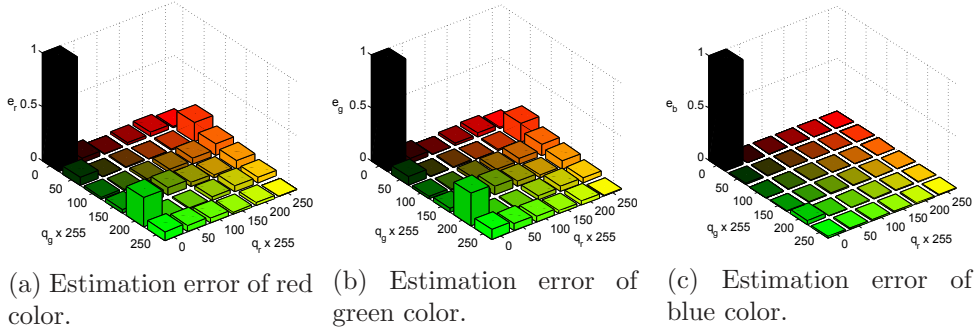


Figure 2.12: Estimation using (2.5) of mixed red, green and blue light (with $q_b = 0$).

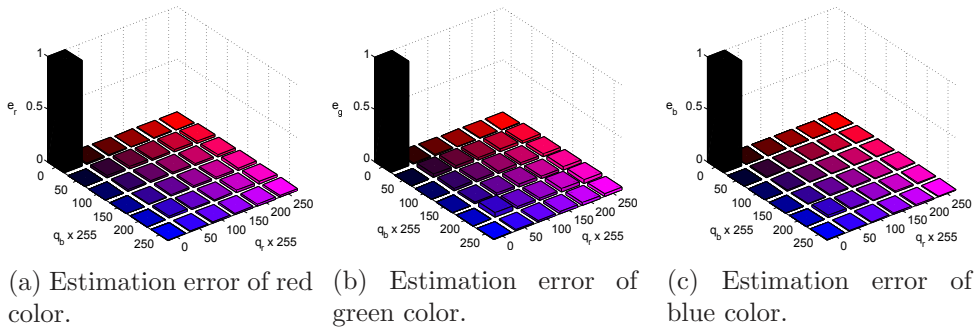


Figure 2.13: Estimation using (2.5) of mixed red, green and blue light (with $q_g = 0$).

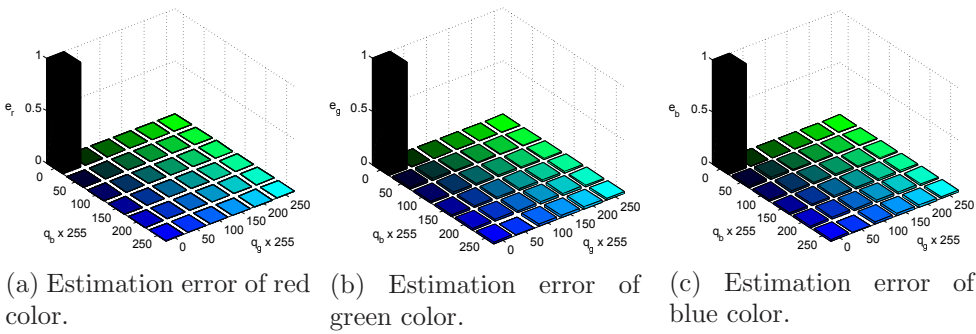


Figure 2.14: Estimation using (2.5) of mixed red, green and blue light (with $q_r = 0$).

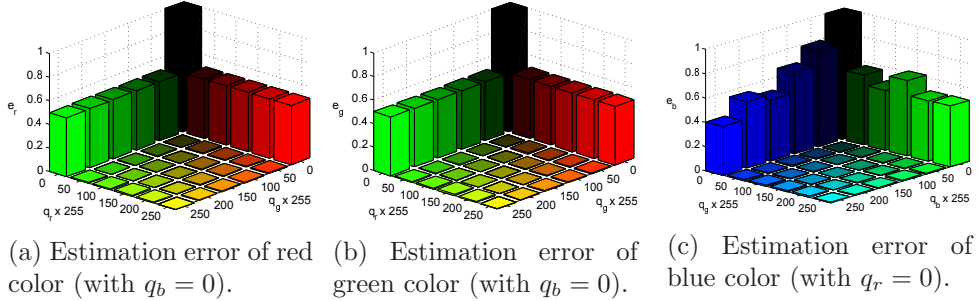


Figure 2.15: Estimation error of the DWT based method.

each estimated red, green and blue color components are indicated by the height of each cube. The estimation error at origin is assigned to 1 and served as a reference. In Fig. 2.13 and 2.14, we respectively show the estimation errors of combined red and blue light as well as combined green and blue light. For the considered matrix \mathbf{S}_1 , this method gives quite small estimation errors.

Figs. 2.15a and 2.15b show the estimation errors e_r and e_g given by the target lamp L_D which runs the DWT based estimation method. At color transporter, the blue light duty cycle q_b is preset to be 0. The duty cycles q_r and q_g respectively increases from 0 to approach 1 in steps of $\frac{50}{255}$. The resulting cube color is specified by the corresponding RGB color code and the cube height indicates the absolute error value. Significant errors are observed in two cases: $q_r = 0$ and $q_g = 0$. In the first case, color transporter only emits green light at different brightness levels. As such, the observation v_R transforms from the n-p-p-n pattern to a n-p-n pattern. The estimation \hat{q}_r is determined to equal \hat{q}_g and equals $\frac{t_{p1} - t_{n1}}{T}$. Using (2.13), the estimation error vector is calculated as $\underline{e} = |[0 \ 1 \ 0]^T - [0.5 \ 0.5 \ 0]^T| = [0.5 \ 0.5 \ 0]$, which is consistent with the plot. The second case follows a similar explanation.

Fig. 2.15c shows the estimation error e_b given by the target lamp L_D which runs the DWT based estimation method. At color transporter, the red light duty cycle q_r is preset to be 0. The duty cycles q_g and q_b respectively increases from 0 to approach 1 in steps of $\frac{50}{255}$. Various errors are found in two cases: $q_g = 0$ and $q_b = 0$. In the first case, color transporter emits pure blue light at different brightness levels. Estimation of \hat{q}_g and \hat{q}_b are respectively based on observations v_R and v_G . Because $q_r = 0$ and $q_g = 0$, the observation v_R is noisy. The estimated \hat{q}_g can be a random positive value, making the estimation error also random and large. A similar explanation applies to the second case by considering the noisy observation v_G .

The errors in the estimation analysis above are indicative of the limits in how many, and which, colors can be estimated and transported. Furthermore, the

estimation analysis above was done on the duty cycle vector. The performance analysis may also be done in a different color space such as the CIE XYZ using appropriate transformation [26].

2.6 Conclusions

We presented a LED system prototype with source and destination LED lamps and a LED array as a color transporter device. A color sensing and illumination driver protocol was presented such that the LED lamps could sense color while illuminating without perceivable flicker. A similar protocol was used at the LED array transporter device with the additional use of hardware triggers to have the device either in sensing or illumination mode. Two color estimation methods were presented to map the measured voltage on the red, green and blue channels to a sensed color. Evaluation of the proposed methods showed that it is possible to detect colors efficiently, with the exception of a few corner cases. The proposed RGB LED system is especially attractive in consumer applications where sensor placement is either cumbersome or expensive.

Acknowledgements

The authors thank David Caicedo and Frans M. J. Willems for their useful comments and feedback on early drafts of the manuscript.

REFERENCES

- [1] F. C. Wang, C. W. Tang, and B. J. Huang, "Multivariable robust control for a red-green-blue LED lighting system," *IEEE Transactions on Power Electronics*, vol. 25, no. 2, pp. 417–428, 2010.
- [2] S. Muthu, F. J. P. Schuurmans, and M. D. Pashley, "Red, green, and blue LEDs for white light illumination," *IEEE Journal of Selected Topics in Quantum Electronics*, vol. 8, no. 2, pp. 333–338, 2002.
- [3] A. Pandharipande and D. Caicedo, "Adaptive illumination rendering in LED lighting systems," *IEEE Transactions on Systems, Man, and Cybernetics: Systems*, vol. 43, no. 5, pp. 1052–1062, 2013.
- [4] S. Afshari, S. Mishra, A. Julius, F. Lizarralde, J. D. Wason, and J. T. Wen, "Modeling and control of color tunable lighting systems," *Energy and Buildings*, vol. 68, Part A, pp. 242–253, 2014.
- [5] H. Yang, T. C. W. Schenk, J. W. M. Bergmans, and A. Pandharipande, "Enhanced illumination sensing using multiple harmonics for LED lighting systems," *IEEE Transactions on Signal Processing*, vol. 58, no. 11, pp. 5508–5522, 2010.
- [6] C. C. Chang, C. C. Chen, U. Kurokawa, and B. I. Choi, "Accurate sensing of LED spectra via low-cost spectrum sensors," *IEEE Sensors Journal*, vol. 11, no. 11, pp. 2869–2877, 2011.
- [7] G. Pang, T. Kwan, H. Liu, and C.-H. Chan, "LED wireless," *IEEE Industry Applications Magazine*, vol. 8, no. 1, pp. 21–28, 2002.
- [8] E. Schubert, *Light-Emitting Diodes*. Cambridge University Press, 2006.
- [9] P. Dietz, W. Yerazunis, and D. Leigh, "Very low-cost sensing and communication using bidirectional LEDs," *5th International Conference on Ubiquitous Computing*, pp. 175–191, 2003.
- [10] D. Giustiniano, N. O. Tippenhauer, and S. Mangold, "Low-complexity visible light networking with LED-to-LED communication," *IFIP Wireless Days*, pp. 1–8, November 2012.
- [11] Schmid, Stefan, G. Corbellini, S. Mangold, and T. R. Gross, "LED-to-LED visible light communication networks," *Proceedings of the Fourteenth ACM International Symposium on Mobile Ad Hoc Networking and Computing*, pp. 1–10, 2013.

- [12] G. Corbellini, K. Aksit, S. Schmid, S. Mangold, and T. R. Gross, “Connecting networks of toys and smartphones with visible light communication,” *IEEE Communications Magazine*, vol. 52, no. 7, pp. 72–78, July 2014.
- [13] A. Pandharipande and S. Li, “Illumination and light sensing for daylight adaptation with an LED array: Proof-of-principle,” *39th Annual Conference of the IEEE Industrial Electronics Society*, pp. 6081–6086, November 2013.
- [14] F. M. Mims, *Siliconconnections: Coming of Age in the Electronic Era*. New York, NY, USA: McGraw-Hill, 1986.
- [15] C. Martiny and M. Wendt, “Intrinsic sensing and color control of multiLED lamp-modules,” *Philips Research, Eindhoven, The Netherlands, Tech. Rep. PR-TN 2006/00195*, 2006.
- [16] J. S. Bajić, B. Dakić, D. Z. Stupar, M. P. Slankamenac, and M. B. Živanov, “The frequency-modulated reflective color sensor,” in *Proceedings of the 35th International Convention MIPRO*, pp. 162–166, May 2012.
- [17] M. Moghavvemi, S. S. Jamuar, E. H. Gan, and Y. C. Yap, “Design of low cost flexible RGB color sensor,” *International Conference on Informatics, Electronics Vision*, pp. 1158–1162, May 2012.
- [18] A. Polzer, W. Gaberl, M. Davidovic, and H. Zimmermann, “Integrated filterless BiCMOS sensor for RGB-LED color determination,” *IEEE8 SENSORS Proceedings*, pp. 1937–1940, October 2011.
- [19] S. Li and A. Pandharipande, “Color sensing and illumination with LED lamps,” *IEEE Fourth International Conference on Consumer Electronics Berlin*, pp. 1–2, September 2014.
- [20] S. Boyd and L. Vandenberghe, *Convex Optimization*. New York, NY, USA: Cambridge University Press, 1986.
- [21] A. Wills, A. Mills, and B. Ninness, “FPGA implementation of an interior-point solution for linear model predictive control,” in *Proceedings 18th IFAC World Congress*, vol. 44, no. 1, pp. 14 527–14 532, 2011.
- [22] P. Zometa, M. Kögel, T. Faulwasser, and R. Findeisen, “Implementation aspects of model predictive control for embedded systems,” in *Proceedings American Control Conference*, pp. 1205–1210, June 2012.
- [23] M. Stéphane, *A Wavelet Tour of Signal Processing*. San Francisco, CA, USA: Academic Press, 2008.

REFERENCES

- [24] M. Basu, "Gaussian-based edge-detection methods-a survey," *IEEE Transactions on Systems, Man, and Cybernetics, Part C (Applications and Reviews)*, vol. 32, no. 3, pp. 252–260, August 2002.
- [25] T. Gevers and A. W. Smeulders, "Color-based object recognition," *Pattern Recognition*, vol. 32, no. 3, pp. 453–464, 1999.
- [26] *Multimedia Systems and Equipment Colour Measurement and Management-Part 21: Colour Management Default RGB Colour Spaces RGB*. IEC document 61966-2-1:1999, 1999.

Chapter 3

Daylight sensing LED lighting system*

Adaptation of artificial light based on the available amount of daylight is known to be effective for energy savings. To achieve such daylight control, the state-of-the-art lighting systems use external photodetectors. The photodetector measures the combined contribution of artificial light and daylight, and closed-loop control schemes are used to determine the dimming levels of luminaires to produce the right amount of artificial light. In this chapter, we propose LED luminaires that can perform the dual function of illumination and daylight sensing, obviating the need of additional photodetectors. We present a daylight sensing luminaire prototype and consider two driving protocols for sensing and illumination. An open-loop control scheme is then considered for daylight control. The proposed system is shown to be more robust to reflectance changes in comparison with a photodetector-based closed-loop lighting control system.

*This chapter has been published as: S. Li, A. Pandharipande and F. M. J. Willems, "Daylight sensing LED lighting system", *IEEE Sensors Journal*, vol. 16, no. 9, pp. 3216-3223, May 2016.

3.1 Introduction

Light emitting diodes (LEDs) are being widely adopted for general lighting applications in offices, industry and homes. With LED lighting systems, the light output can be flexibly and easily controlled. This is especially attractive for daylight adaptive lighting control for reducing the substantial portion of the electrical energy that is consumed by lighting. In such lighting control systems, the light output from the luminaires is adapted to produce artificial illumination in accordance with changing daylight such that the net achieved illuminance meets illuminance requirements, while saving energy [1], [2], [3], [4]. Thus when there is sufficient amount of daylight, the luminaires are dimmed while maintaining a desired illuminance value at the workspaces.

In state-of-art lighting control systems, the achieved illuminance is monitored using external photodetectors [5] at the ceiling as depicted in Fig. 3.1. In office applications, the goal is to achieve illuminance values at workspaces higher than desired values specified according to lighting norms, see for example [6]. The desired illuminance values at workspaces are mapped to target set-points to be achieved at the photodetectors via a night-time calibration phase [4]. Using feedback in the form of photodetector measurements, the lighting controller seeks to achieve the target set-points by adapting the dimming levels of the luminaires. Various control methods with different objective functions have been considered in [1], [2], [3], [4], [7]. Such photodetector based lighting control systems have the following drawbacks:

- (i) The use of additional photodetectors leads to extra cost and installation complexity.
- (ii) A photodetector measures both the daylight and artificial light from all the luminaires that is reflected back within its field-of-view. Thus, careful design of closed-loop feedback control is required to obtain the dimming levels of the luminaires so as maintain stability and system responsiveness to illumination changes [1], [3].
- (iii) Under environmental changes, the reflectance values of the surfaces beneath the photodetectors may vary with time. Examples of such changes are the movement of desks and placement of a bright object on a dark desk surface. This leads to more (or less, depending on the reflectance of the objects) artificial light as well as daylight being reflected back at the photodetector. As a result, this can lead to large deviations in the achieved illuminance from the desired illuminance values [8], [9].

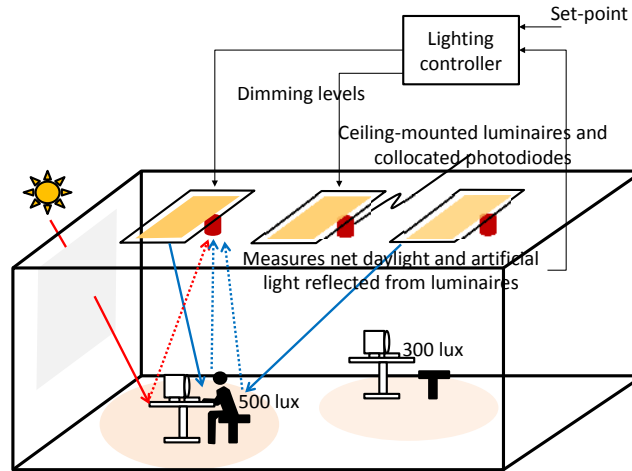


Figure 3.1: Photodetector based lighting control system.

In this paper, we explore the dual use of a LED luminaire as a light source as well as a light sensor. A typical LED luminaire used in general lighting applications consists of phosphor-coated blue LEDs to produce white light. We use such a LED luminaire to operate in two modes: a light emitting mode and a sensing mode. Both modes are time-multiplexed by a sensing and illumination control driver protocol. In emitting mode, the LED luminaire is switched on with a dimming level determined by a pulse width modulation (PWM) signal. During the sensing mode, the LED luminaire is switched off and serves as a light sensor. In this mode, the illuminance measured by the LED luminaire corresponds to the daylight contribution. This is due to the physical property of the phosphor-coated blue LEDs to sense an ultraviolet component that is present in daylight, but is absent in artificial light.

3.1.1 Contributions and organization of the work

We design a LED luminaire prototype, without any modifications to the LEDs or their structure, to perform the dual function of illumination and daylight sensing. The details of the designed daylight sensing luminaire prototype are presented in Section 3.2.

A time-multiplexing driver protocol to provide illumination and perform daylight sensing is then proposed (Section 3.3). Key considerations in the protocol design are that no additional perceivable flicker is caused due to the daylight sensing function and that the loss in light output due to sensing is limited. We then consider a calibration mechanism, akin to conventional photodetectors, to

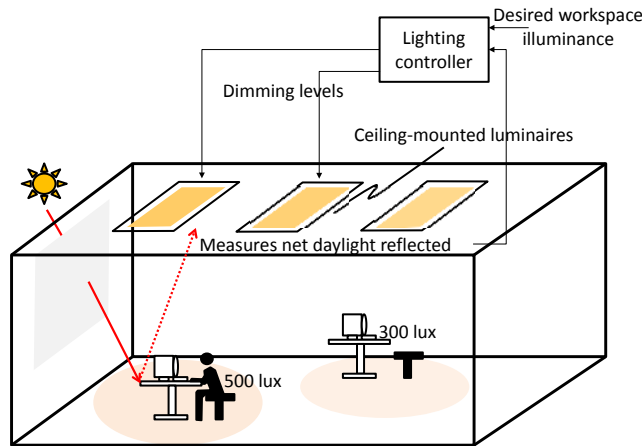


Figure 3.2: Proposed daylight sensing based lighting control system.

map the illuminance measurement of the daylight sensing LED luminaire to that expected at the workspace plane. Different to the photodetector calibration that is done using artificial lighting in dark conditions in the absence of daylight, the LED luminaire calibration has to be done in daylight conditions. Using the mapping obtained from calibration and sensed illuminance measurements, an open-loop illumination control scheme to obtain luminaire dimming levels for daylight adaptation is then considered. The proposed daylight sensing based lighting control system is depicted in Fig. 3.2. The calibration and control methods are described in Section 3.4.

Given that the LED luminaire primarily measures the daylight contributions, an advantage of the proposed daylight sensing based control system is that it is more robust to the impact that reflectance changes have on a conventional photodetector based lighting control system. The performance of the proposed daylight sensing LED lighting system is compared to a photodetector based lighting system in an experimental setup by inducing reflectance changes in the environment. These experimental results are reported in Section 3.5.

We extend our preliminary work [10] where a LED array prototype with six LEDs was used to demonstrate the proof-of-principle of daylight sensing. The design used a photoconductive mode, in contrast to the use of the photovoltaic mode in this work. The photovoltaic mode of operations allows a simple implementation as will be discussed further in Section 3.2.

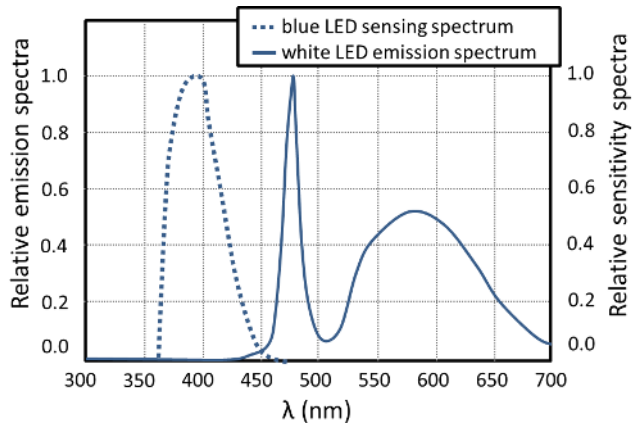


Figure 3.3: Emission and sensing spectra of phosphor-coated blue LED.

3.1.2 General principle of LED as light sensor

The use of LEDs as light sensors has been known for long [11]. This property has been used in different applications like interactive control, consumer electronics and data communication [12], [13], [14]. In sensing mode, a LED shows wavelength-selective sensitivity over a band that is below the emission band. Such wavelength-selective sensing behavior is consistent with the photo responsivity of a single phosphor-coated blue LED to produce white light, as depicted in Fig. 3.3. The emission spectrum of the white LED thus consists of the blue luminescence and long phosphorescence [15], as shown by the solid line in Fig. 3.3. The dashed line in Fig. 3.3 shows the relative sensitivity spectrum of the blue LED [16]. Approximately 70 nm shift is observed between the emission and sensing spectra for the blue LED. This has been attributed to the internal piezoelectric fields, spontaneous polarization and excitation recombination. Note that the ultraviolet A (UV-A) wavelength range is within the pass-band (370 nm to 450 nm) of the blue LED sensing spectrum. In addition, UV-A light is able to pass through phosphor with very limited radiation energy loss [17]. Therefore, daylight estimation is achieved by measuring the excited photocurrent which relates to the pure daylight component.

3.2 Daylight sensing luminaire prototype

In this section, we describe the daylight sensing luminaire prototype. It consists of a digital micro-controller unit (MCU), a phosphor-converted white LED array

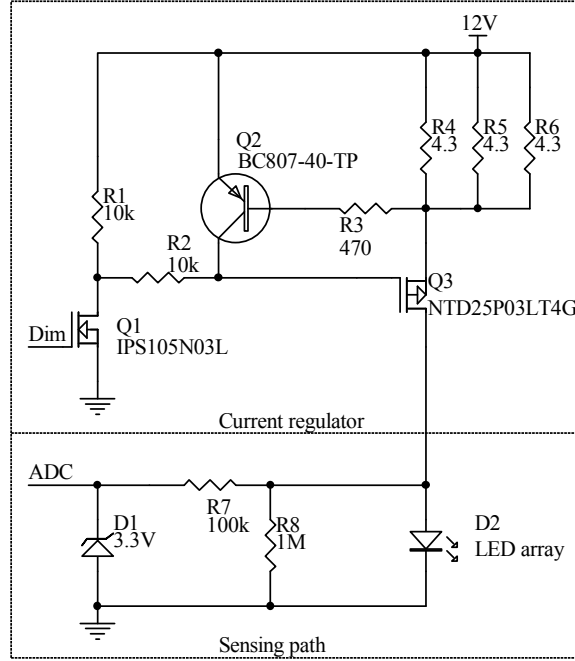


Figure 3.4: Proposed dual-mode luminaire driver block diagram.

and a dual-mode driver circuit. The MCU implements a daylight sensing protocol and a daylight adaptive controller. The dual-mode driver circuit achieves dimming of the LED array and switches between an illumination mode and a sensing mode.

Fig. 3.4 illustrates the dual-mode driver circuit comprising a current regulator and a sensing path. The current regulator implements a constant current source. The drain current, I_D , of transistor Q3 can be written as

$$I_D = \begin{cases} V_{BE} \times \left(\frac{1}{R_4} + \frac{1}{R_5} + \frac{1}{R_6} \right) & , \text{Q1 is ON} \\ 0 & , \text{Q1 is OFF,} \end{cases} \quad (3.1)$$

where V_{BE} is the voltage between the base and the emitter of transistor Q2. Resistors R4, R5 and R6 are chosen such that the nominal forward current of the LED array D2 is achieved. In order to provide dimming functionality for daylight-adaptive control, switch Q1 is duty-cycled by a pulse-width-modulation signal *Dim*. This control signal is the output of the daylight adaptive controller and is provided by a MCU pin. Denoting the ON period of signal *Dim* with q

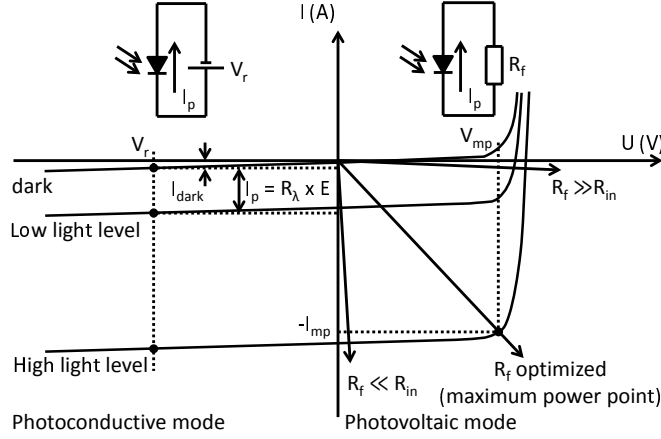


Figure 3.5: Current-voltage (I-V) curve of a typical photodiode.

($0 \leq q \leq 1$), the current regulator output i_o is

$$i_o = q \times I_D. \quad (3.2)$$

For the selected white LED array, current i_o can vary from 0 to 575 mA which exceeds the maximum current that can be sunk by MCU pins. Therefore, a 3.3 V zener diode D1 is used to prevent the MCU pin *ADC* from being damaged by the current regulator. In addition, a shunt resistor R7 is used to limit the current sunk by ground and thus increase the efficiency of the driver circuit.

The driver circuit is switched to sensing mode during the OFF period of the *Dim* signal. As per (3.1), current i_o is null ignoring the drain-to-source leakage current of transistor Q3. The LED array is isolated from the current regulator and serves as a photodetector. It is zero-biased and operates at photovoltaic mode, driving a load resistor R8. The load voltage is measured by the analog-to-digital converter (ADC) of the MCU and translated to illumination level using a calibration function. With the ADC measurements, the daylight adaptive controller updates control signal *Dim* at a period scheduled by the sensing protocol.

Fig. 3.5 illustrates the I-V curve of a typical photodiode under different illumination levels [18]. With reverse bias voltage V_r , an excited photocurrent I_p is linearly related to an illumination level E by the responsivity R_λ (A/W) of the photodiode. In general, photodetectors operate at photoconductive mode for better response linearity. However, we choose to apply the photovoltaic mode for two reasons. First, it is difficult to provide reverse bias voltage with limited modifications to conventional LED driver topologies. Second, the applied reverse bias voltage generates dark current i_{dark} as an error factor. In contrast, in the

photovoltaic mode, the dark current is zero because there is no external voltage across the photodetector. Therefore, the photovoltaic mode is potentially better to measure the reflected illumination levels using a ceiling mounted LED luminaire. In addition, it is easier to implement photovoltaic mode with one extra load resistor (R_8 in Fig. 3.4).

As shown in Fig. 3.5, linearity still holds for light loads with resistance R_f much smaller than the internal resistance R_{in} of photodiode. In this case, an extra voltage amplifier is required for high resolution. As load resistor R_f approaches to the maximum power point, the resolution increases while maintaining linearity. Afterwards, the increment of R_f degrades the linearity as well as resolution. In the extreme case where $R_f \gg R_{in}$ (i.e. open circuit), photocurrent I_p relates to illumination level in a logarithmic manner. The resulting photodiode is less robust to noise. Therefore, the value of load resistor R_f has to be chosen so as to retain linearity within a certain sensing range while achieving a high resolution.

In practice, LED luminaires consist of a combination of series and parallel strings. The I-V curve of the LED array has to be characterized in order to optimize the load resistor R_f . With the selected photovoltaic mode, we adopt the mathematical model of a photovoltaic array considered in [19]. For a LED array formed by N_{ser} identical LEDs connected in series and N_{par} of such strings in parallel, the following I-V equation applies

$$I = I_p N_{par} - I_0 N_{par} \left[\exp \left(\frac{V + R_s \left(\frac{N_{ser}}{N_{par}} I \right)}{V_t a N_{ser}} \right) - 1 \right] - \frac{V + R_s \left(\frac{N_{ser}}{N_{par}} I \right)}{R_p \left(\frac{N_{ser}}{N_{par}} \right)}, \quad (3.3)$$

where I_p and I_0 are respectively the light-generated photocurrent and saturation current of a single LED. Parameters R_s and R_p are the internal series and parallel resistance of each LED. Parameter a is the diode ideality constant and V_t is the thermal voltage. With the I-V characteristic of LED luminaire, the maximum power point corresponding to a certain illumination level E can be found. Assuming that linearity is required over a sensing range upper bounded by illumination level E_o , we first use (3.3) to find the maximum power point corresponding to E_o and denote it by $(V_{mp}, -I_{mp})$. The optimized value of load resistor R_f is then determined as $\frac{V_{mp}}{I_{mp}}$.

Apart from resolution and linearity, the bandwidth of the sensing path circuit is also important. It not only determines the daylight sensing speed but also impacts the illumination quality. A narrow bandwidth requires longer sensing period, making the averaged illumination level below a visual comfort level or

3.3. DAYLIGHT SENSING AND ILLUMINATION CONTROL DRIVER PROTOCOL

even causing flicker. The 3 dB bandwidth of the LED array can be written as

$$f_{3dB} = \frac{1}{2\pi R_L C_{eq}} = \frac{1}{2\pi R_f C_J}, \quad (3.4)$$

where $C_{eq} = \frac{N_{par}}{N_{ser}} C_J$ and $R_L = \frac{N_{ser}}{N_{par}} R_f$ are respectively the equivalent capacitance and load resistance of the LED array, C_J is the junction capacitance of a single LED, and R_f is the optimized load resistance for a single LED. For the designed sensing luminaire, the bandwidth is independent of the LED structure and is solely determined by the capacitance and V-I characteristic of a single LED.

3.3 Daylight sensing and illumination control driver protocol

In this section, we explain the daylight sensing and illumination control driver protocol implemented at the MCU. Based on the application, two control protocols are proposed as described in Figs. 3.6 and 3.7. In the first protocol, control signal Dim is in the form of a standard PWM wave w_1 with duty cycle q_1 and frequency f_1 . Daylight sensing is executed at the OFF period of each PWM cycle. Due to the existence of a sensing period, duty cycle q_1 is smaller than 1. Thus, the maximum possible luminance output will not be achieved by the luminaire. In the second protocol, control signal Dim is a product of a standard PWM wave w_1 with another square wave w_2 . Wave w_2 features a duty cycle q_2 and frequency f_2 . During the ON period of w_2 , the luminaire outputs light with a level determined by the wave w_1 . The OFF period of w_2 serves as a dedicated sensing time slot during which the luminaire conducts daylight sensing. The design details and benefits of each protocol are now discussed respectively.

The first control protocol is illustrated in Fig. 3.6 with the MCU clock number shown over the X-axis and the Y-axis shows the waveform of control signal Dim over $N_s + N_u$ PWM cycles. Parameter N_s is the number of ADC samples collected by the MCU. The averaged value is used to calculate the updated dimming level at time cost of N_u cycles. For the first N_s cycles, each one is composed of a light emitting period t_e , discharging period t_d and sensing period t_s . Over period t_e , the luminaire is forward-biased to emit light. Over period t_d , the luminaire is switched off and discharges the residual forward voltage through resistors R7 and R8 (Fig. 3.4). Over period t_s , the ADC measures the photovoltage on load resistor R8 at a single-channel single-conversion mode. During the other N_u cycles, the MCU not only collects N_u samples but also executes the daylight adaptive control with the averaged N_s samples as an input. In this way, the daylight sensing and

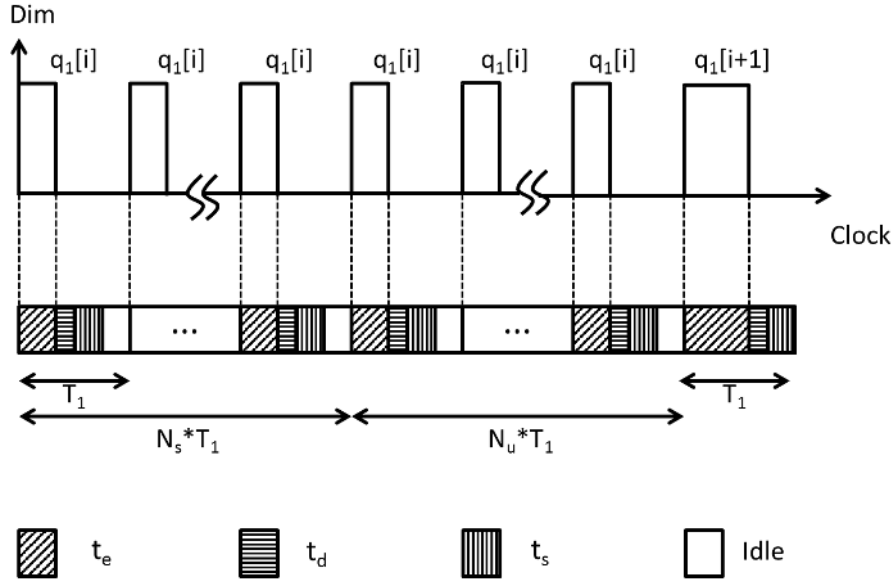


Figure 3.6: Illumination and sensing protocol 1.

adaptation are pipe-lined. The maximal throughput is achieved if N_s equals N_u . Daylight sensing at each PWM cycle benefits with a fast-response system at the cost of a constrained illumination level less than or equal to $1 - \eta_1$, where parameter η_1 is the maximum illuminance loss given by

$$\eta_1 = \frac{t_d + t_0 + 1/f_s}{T_1}, \quad (3.5)$$

where $T_1 = 1/f_1$, t_0 is the setup time of the ADC and f_s is the ADC sampling frequency.

The second control protocol is depicted in Fig. 3.7 with X-axis the MCU clock number and Y-axis the waveform of control signal *Dim* over $N_e + N_s + N_u$ PWM cycles. Parameter N_e is the number of wave w_1 cycles, which consists of pure light emitting periods t_e . As such, the corresponding illumination level is unconstrained and is at the range between 0 and 1. The subsequent t_d plus t_s periods constructs the OFF period of one w_2 cycle. Over the t_d period, the luminaire is switched off and discharges the residual forward voltage. Over period t_s , the ADC measures the photovoltage on load resistor R8 at repeat single channel mode. The collected samples are used to update the illumination level during the last N_u cycles. Meanwhile, light emitting period t_e is repeated with historical illumination level. The corresponding illumination loss is formulated

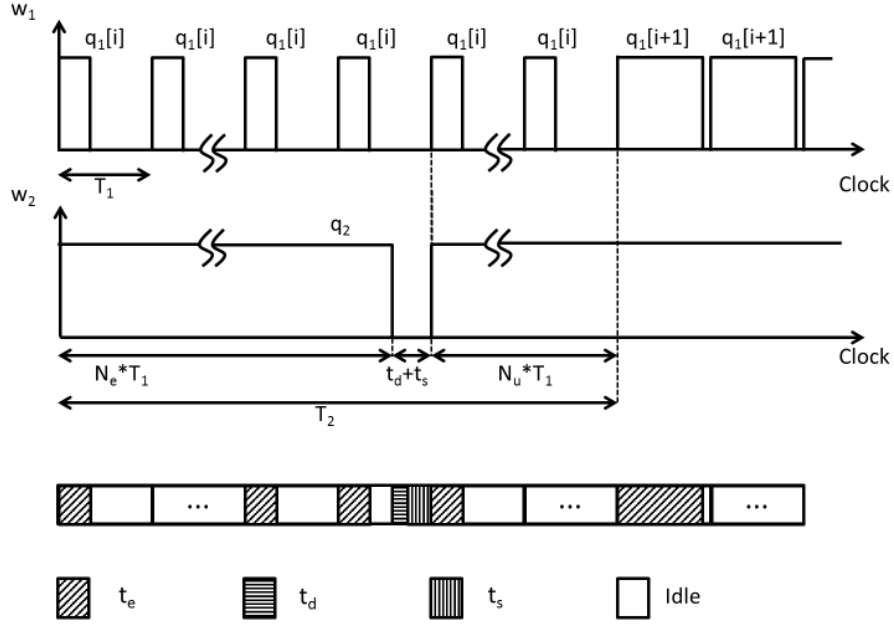


Figure 3.7: Illumination and sensing protocol 2.

as

$$\eta_2 = \frac{t_d + t_0 + N_s/f_s}{(N_e + N_u)T_1}. \quad (3.6)$$

In applications where daylight sensing frequency is in the order of seconds, the denominator is much greater than the numerator. As such, η_2 is small and the illumination level loss is negligible.

3.4 Luminaire calibration and control method

In this section, we describe the daylight sensing luminaire calibration and associated control scheme. A benchmark is set up to evaluate the luminaire performance.

3.4.1 Daylight sensing luminaire calibration and control method

Fig. 3.8 illustrates the elements of daylight sensing luminaire calibration and control. Denote the measured photovoltage by luminaire k as v_k . Let calibration

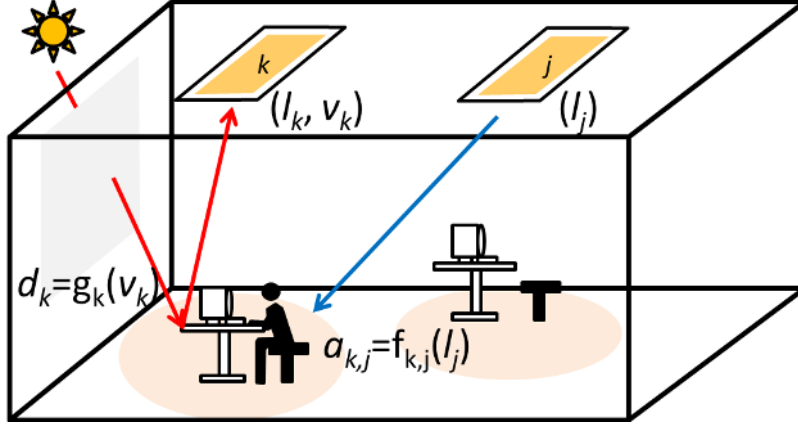


Figure 3.8: Daylight sensing luminaire calibration setup.

function $g_k(\cdot)$ denote the mapping of the photovoltage v_k to the estimated daylight level d_k at the workspace level under luminaire k . Let the dimming level of luminaire j be l_j . Denote the function $f_{k,j}(\cdot)$ to be illuminance contribution of luminaire j at the workspace under luminaire k .

The desired illumination level at workspace plane under luminaire k , W_k , is given as

$$W_k = \begin{cases} W_k^o & , \text{if workspace under luminaire } k \text{ is occupied,} \\ W_k^u & , \text{otherwise.} \end{cases} \quad (3.7)$$

An iterative control method to update l_k , the dimming level of luminaire k , at n^{th} iteration is formulated as

$$l_k[n] = \begin{cases} \Phi \left\{ f_{k,k}^{-1}(e_k[n]) \right\} & , \text{if } |e_k[n]| > \epsilon_k \\ l_k[n-1] & , \text{otherwise,} \end{cases} \quad (3.8)$$

where $e_k[n] = W_k - \sum_{j \neq k} f_{k,j}(l_j[n]) - d_k[n]$ captures the amount of artificial light to be compensated by luminaire k . The estimated daylight at the workspace level under luminaire k is calculated as $d_k[n] = g_k(v_k[n])$. A saturation function $\Phi\{\}$ ensures that dimming level is within a valid range: $\{0 \leq l_k[n] \leq (1 - \eta_1)\}$ in protocol 1 and $\{0 \leq l_k \leq (1 - \eta_2)\}$ in protocol 2. Parameter $\epsilon_k > 0$ is a deadband.

3.4.2 Benchmark lighting control system

Fig. 3.9 illustrates the benchmark setup which is different from luminaire calibration in two aspects. First, all luminaires only work at emitting mode with

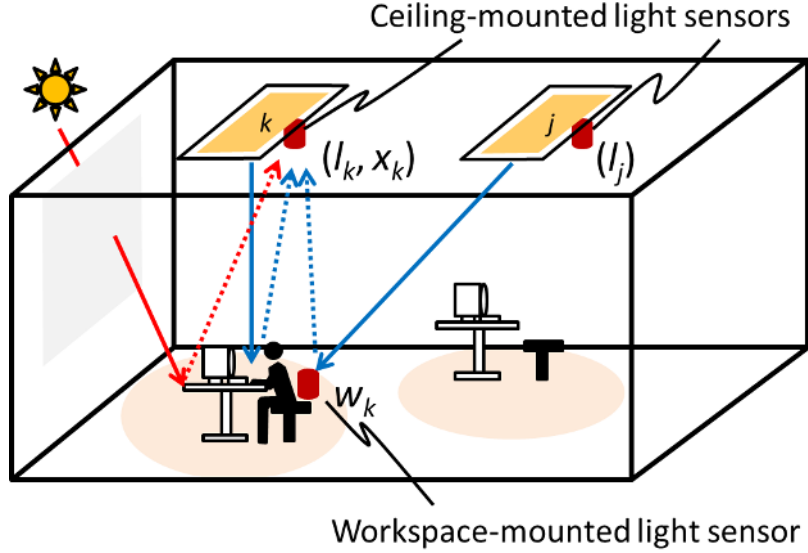


Figure 3.9: Benchmark setup.

dimming levels varying at a range between 0 and 1. Second, a dedicated photodetector is commissioned under each luminaire, capturing illumination level of both daylight and artificial light. Denote the illumination level measured by the ceiling-mounted photodetector collocated at luminaire k by x_k , the target illumination level at this photodetector by z_k and the dimming level of luminaire k by l_k . A closed-loop control law to update l_k at n^{th} iteration is formulated as

$$l_k[n] = \begin{cases} \Phi(l_k[n-1] + K_P e_k[n] + K_I \sum_{j=1}^{j=J} e_k[n-j]) & , \text{if } |e_k[n]| > \varepsilon_k \\ l_k[n-1] & , \text{otherwise,} \end{cases} \quad (3.9)$$

where $e_k[n] = z_k - x_k[n]$ is the error associated with the luminaire k . Parameters $K_P > 0$ and $K_I > 0$ are controller coefficients chosen such that the control loop is stable.

The target illumination level z_k is obtained during a dark-room calibration step with all luminaires set to a reference dimming level that results in a illumination level W_k^* . We then calculate a scaling factor for luminaire k ,

$$c_k = \frac{X_k}{W_k^*}, \quad (3.10)$$

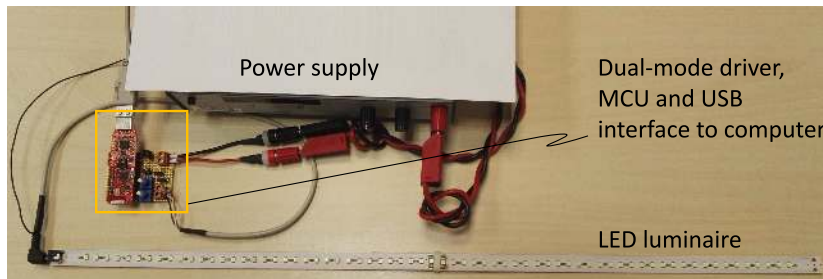


Figure 3.10: Prototype of designed dual-mode luminaire.

where X_k and W_k^* are respectively the measured illumination levels from the ceiling-mounted and workspace-mounted photodetectors. Using this calibration factor, W_k as derived from (3.7) can be translated into a target illumination level at ceiling-mounted photodetector at the ceiling,

$$z_k = c_k W_k. \quad (3.11)$$

3.5 Experimental results

In this section, we evaluate the performance of the daylight sensing LED luminaire and compare it with a photodetector based lighting control system. For the proposed system, daylight calibration is also evaluated by considering different daylight conditions.

3.5.1 Experimental setup

The designed daylight sensing LED luminaire prototype is depicted in Fig. 3.10, with the luminaire containing 68 LEDs (two LEDs in series and 34 of these connected in parallel). Protocol 2 was used to drive the luminaire. Two such luminaires were placed in a “ceiling-mounted configuration” inside a closed box enclosure as shown in Fig. 3.11, emulating an indoor space. To facilitate benchmarking, two photodetectors were collocated at the luminaires. The illumination achieved at the “workspace plane” under the luminaires was monitored using two additional photodetectors. All measurements were collected at a computer via a universal asynchronous receiver/transmitter (UART) interface, where the control algorithm was implemented. The computed dimming levels from the algorithm were used to update the dimming levels of the luminaires.

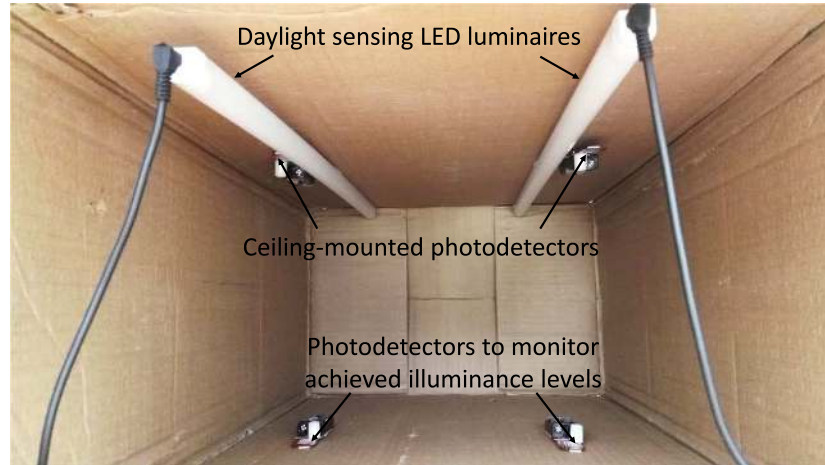


Figure 3.11: Experimental setup with two daylight sensing luminaires.

3.5.2 Calibration functions

Calibration function g_k

The calibration function $g_k(\cdot)$ relates the photovoltage v_k to the estimated daylight at the workspace under luminaire k . It was obtained at daytime with the luminaires in daylight sensing mode. The luminaire measurement v_k was collected, as well as the photodetector measurement w_k . To capture the impact of daylight variation, data was collected from 8 A.M. till 6 P.M. every two hours. To include the impact of weather conditions, data was collected under clear sky and overcast sky conditions. The collected data samples are shown in Table 3.1.

A best linear fit was used to obtain the calibration function $g_k(\cdot)$ as is shown in Fig. 3.12. Note that while the best linear fit is a reasonable fit for most of the data points, some data points are away from the fit. It is thus conceivable to create a simple calibration procedure using a few daylight measurements by creating different daylight situations (e.g. by modifying blind positions).

Calibration function $f_{k,j}$

The calibration function $f_{k,j}(\cdot)$ relates the dimming level of luminaire j to the artificial light contribution at the workspace under luminaire k and is obtained during a dark-room calibration. In this case, only luminaire j is switched on to work in light emitting mode. Its dimming level was increased from 0 to 1 at steps of 0.1, and the illuminance values measured by the photodetector under luminaire k were recorded. The relationship between dimming level l_k and photodetector

Time	Overcast sky		Clear sky	
	v_k (mV)	w_k (lux)	v_k (mV)	w_k (lux)
8 a.m.	0	0	0.6206	36.75
10 a.m.	0.0494	11.2	0.4638	25.55
12 a.m.	1.043	51.8	1.202	39.55
2 p.m.	1.483	54.6	1.654	57.75
4 p.m.	1.549	114.8	1.619	95.55
6 p.m.	0.6652	40.6	1.13	54.95

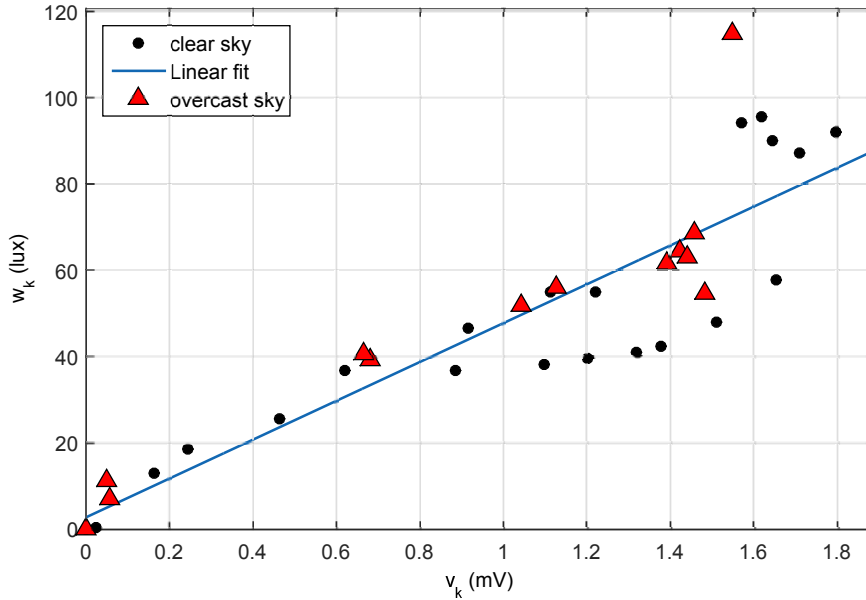
 Table 3.1: Daylight measurements at zone k under different daylight conditions.


Figure 3.12: Calibration mapping.

measurements were found to be linear and a best linear fit for function $f_{k,j}(\cdot)$ was obtained from the measurements.

3.5.3 Performance evaluation

The daylight sensing LED luminaires were controlled using the open-loop control law (3.8), while the reference photodetector based lighting system was controlled using (3.9). The following scenarios capturing changes in occupancy and daylight

were emulated over time:

Initial state: No occupancy; no daylight

- [A] Occupancy in zone k and zone j ; no daylight.
- [B] Occupancy in zone k and zone j ; no daylight; reflective object placed in both zones.
- [C] Occupancy in zone k and zone j ; daylight present; reflective object placed in both zones.
- [D] Occupancy only in zone k ; daylight present; reflective object in both zones.
- [E] Occupancy only in zone k ; daylight present; reflective object removed from both zones.
- [F] No occupancy; daylight present.

For the closed-loop controller, photodetector measurements x_k and x_j were used to update dimming levels l_k and l_j using (3.9). For the control parameters, we chose the following parameters $K_P = 0.5/X_k$, $K_I = 0.5K_P$, $J = 8$, and $\epsilon_k = 0.05X_k$. The photodetector set-points corresponding to occupancy were determined to be $z_k = 100.3$ lux and $z_j = 98.7$ lux. The non-occupancy set-points were obtained by applying a scaling by 0.6.

For the open-loop controller with daylight sensing luminaires, luminaire measurements v_k and v_j were collected via UART links and the dimming levels were computed using (3.8) to update the luminaires.

In Figs. 3.13 and 3.14, we show the illumination performance of the benchmark system and the proposed system respectively. For the benchmark system, the dimming levels of luminaires, the ceiling-mounted photodetector measurements and workspace-mounted photodetector measurements are shown respectively in Figs. 3.13a, 3.13b, and 3.13c. First, we consider a dark environment with no occupancy. This is followed by scenario [A]: local occupancy in both zones after 30 s. Luminaire k and j dim up to reach the desired illumination level of 250 lux. Around 200 s, the scenario is changed to [B] wherein a white colored object is placed at both zones to test the system robustness against reflectance changes. In this situation, due to the higher reflectivity of the object, more light is reflected back to the ceiling-mounted photodetectors. Consequently, both luminaires dim down as a response to the increased illuminance seen at the photodetectors. As such, the workspace-mounted photodetectors record a lower illuminance values at both zones. Then in the scenario [C], daylight is introduced after another 100 s, making under-illumination more obvious. From about

400 s, in the scenario [D] there is non-occupancy in zone j and luminaire j dims down to reach 150 lux. Due to decreased contribution from luminaire j , under-illumination in zone k is more severe. In scenario [E], the reflective object is removed around 480 s, which alleviates under-illumination in both zones, but their desired illumination levels are still not met due to the presence of daylight. Finally, in the scenario [F], there is unoccupancy in both zones and the luminaires turn off.

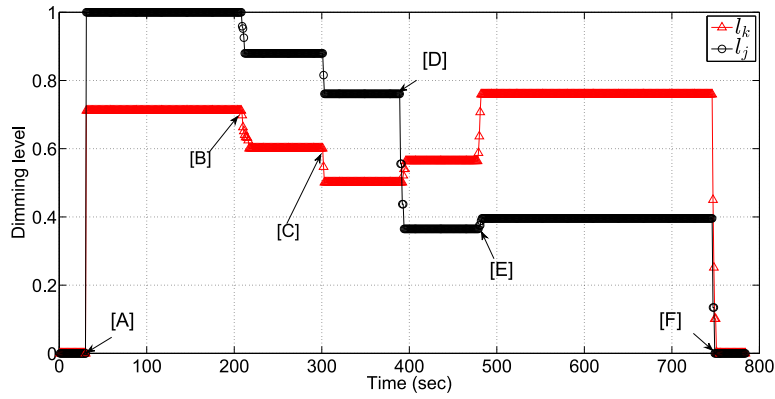
For the proposed system, the dimming levels of luminaires, the photovoltage measurements at the luminaires and workspace-mounted photodetector measurements are shown respectively in Figs. 3.14a, 3.14b, and 3.14c. In scenario [A], there is local occupancy in both zones around 30 s. Luminaire k and j dim up to reach the desired illumination level of 250 lux. Note that the photovoltage measurements at the luminaires are zero, i.e. artificial light is not detected. After around 120 s, a white colored object is placed in both zones. The dimming of the luminaires remains unchanged. Subsequently, in the scenario [C], at around 200 s daylight is introduced. In response, luminaire k dims down. The luminaire j does not react since the contribution of luminaire k becomes lesser as determined by the open-loop control law (3.8). In scenario [D], around 350 s there is local occupancy only in zone k with daylight in both zones. The corresponding luminaire dims down. In scenario [E], around 550 s, there is local occupancy only in zone k and the reflective object is removed from both zones. The dimming level of luminaire j goes slightly higher since less daylight component is reflected back to the luminaire. The dimming level of luminaire k does not increase since it already reaches the maximum. Note from the Fig. 3.14c that the illuminance at the workspace under luminaire j is maintained close to the desired levels within the permissible deadband of 10%. The illuminance at the workspace under luminaire k is also within the deadband for scenarios A, B and C. Afterwards, it falls slightly below the lower bound of desired level since the luminaire reaches its maximum dimming level and there is a lower contribution from the neighboring luminaire.

3.6 Conclusions

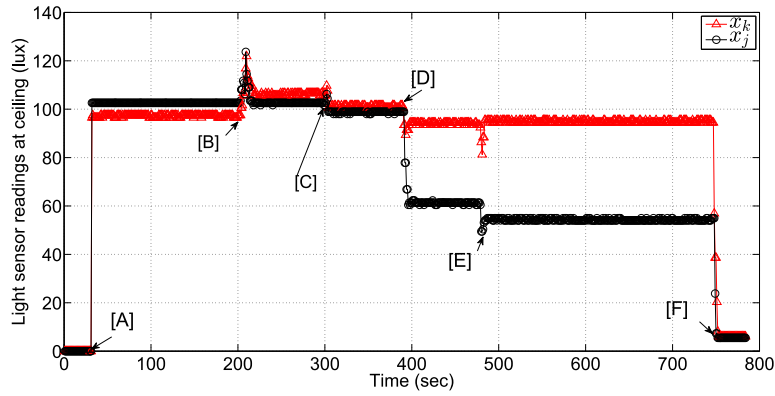
We presented a LED luminaire prototype that can provide the dual functionality of illumination and daylight sensing. The proposed solution avoids the extra cost and installation complexity involved in current lighting control systems that use external photodetectors. Two driver protocols for performing daylight sensing while providing illumination were proposed. Protocol 2 led to only a nominal loss in light output and was chosen for implementation in the luminaire prototype.

3.6. CONCLUSIONS

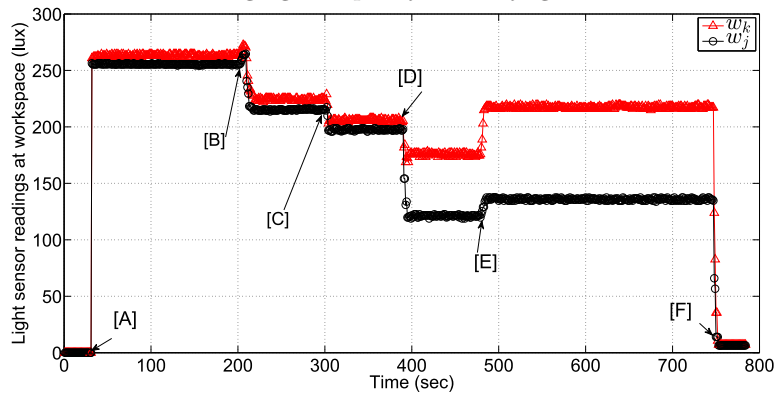
An open loop control method based on the sensed daylight values and knowledge of calibration was used to obtain the dimming levels of the luminaires to adapt to daylight and occupancy changes. The performance of the proposed daylight sensing lighting control system was compared with a photodetector based system and shown to be more robust in the presence of reflectance changes in the environment.



(a) Dimming levels of luminaires in the two zones over time with changing occupancy and daylight.

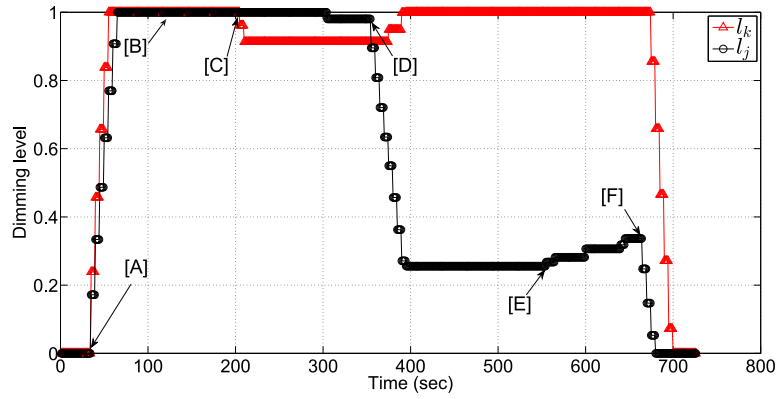


(b) Ceiling-mounted photodetector measurements in the two zones over time with changing occupancy and daylight.

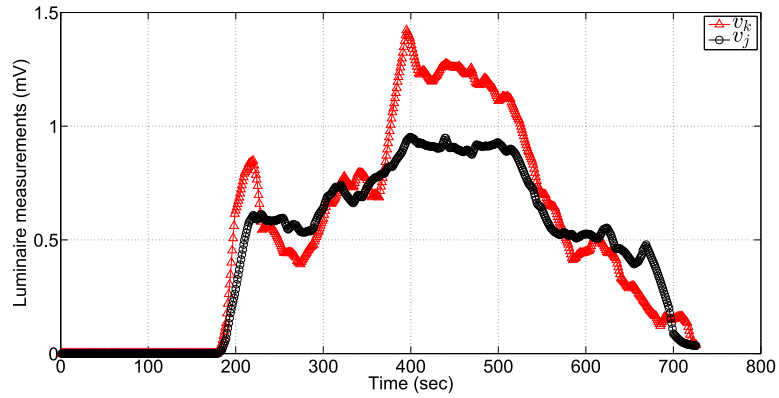


(c) Workspace-mounted photodetector measurements in the two zones over time with changing occupancy and daylight.

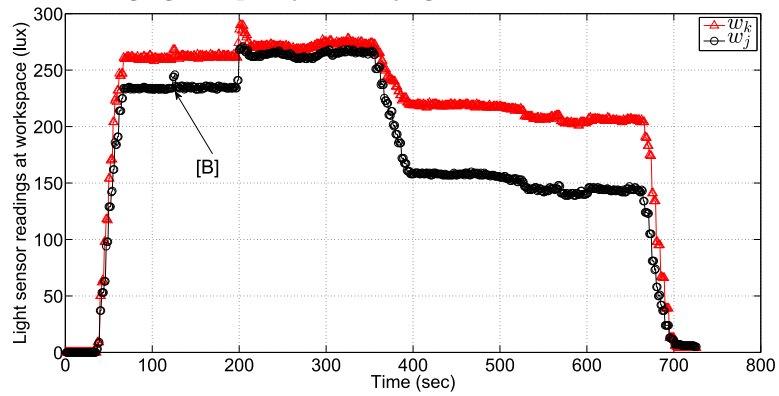
Figure 3.13: Benchmark system performance.



(a) Dimming levels of luminaires in the two zones over time with changing occupancy and daylight.



(b) Photovoltage measurements at the two luminaires over time with changing occupancy and daylight.



(c) Workspace-mounted photodetector measurements in the two zones over time with changing occupancy and daylight.

Figure 3.14: Daylight sensing luminaire system performance.

REFERENCES

- [1] D. Caicedo and A. Pandharipande, “Distributed illumination control with local sensing and actuation in networked lighting systems,” *IEEE Sensors Journal*, vol. 13, no. 3, pp. 1092–1104, 2013.
- [2] S. Tanaka, M. Yoshikata, M. Miki, and T. Hiroyasu, “An evolutionary optimization algorithm to provide individual illuminance in workplaces,” in *IEEE International Conference on Systems, Man and Cybernetics*, pp. 941–947, October 2009.
- [3] N. van de Meughevel, A. Pandharipande, D. Caicedo, and P. van den Hof, “Distributed lighting control with daylight and occupancy adaptation,” *Energy and Buildings*, vol. 75, pp. 321–329, 2014.
- [4] A. Pandharipande and D. Caicedo, “Smart indoor lighting systems with luminaire-based sensing: A review of lighting control approaches,” *Energy and Buildings*, vol. 104, pp. 369–377, 2015.
- [5] A. Bierman, “photosensors, dimming and switching systems for dayling harvesting, national lighting product information program publications,” October 2007, accessed September 2015. [Online]. Available: http://www.lrc.rpi.edu/programs/nlpip/pdf/view/sr_photosensors.pdf
- [6] European Committee for Standardization, “EN 12464-1:2002. Light and lighting. Lighting of work places. Part 1: Indoor work places,” 2002.
- [7] S. Afshari and S. Mishra, “Decentralized feedback control of smart lighting systems,” in *ASME 2013 Dynamic Systems and Control Conference*, pp. 1–10, 2013.
- [8] D. Caicedo, A. Pandharipande, and F. M. J. Willems, “Light sensor calibration and dimming sequence design in distributed lighting control systems,” in *IEEE 11th International Conference on Networking, Sensing and Control*, pp. 344–349, 2014.
- [9] D. Caicedo, A. Pandharipande, and F. M. J. Willems, “Illumination gain estimation and tracking in a distributed lighting control system,” in *IEEE Conference on Control Applications*, pp. 1650–1655, 2014.
- [10] A. Pandharipande and S. Li, “Illumination and light sensing for daylight adaptation with an LED array: Proof-of-principle,” *39th Annual Conference of the IEEE Industrial Electronics Society*, pp. 6081–6086, November 2013.

-
- [11] F. M. Mims, *Siliconconnections: Coming of Age in the Electronic Era*. New York, NY, USA: McGraw-Hill, 1986.
- [12] S. Li and A. Pandharipande, “LED-based color sensing and control,” *IEEE Sensors Journal*, vol. 15, no. 11, pp. 6116–6124, November 2015.
- [13] P. Dietz, W. Yerazunis, and D. Leigh, “Very low-cost sensing and communication using bidirectional LEDs,” *5th International Conference on Ubiquitous Computing*, pp. 175–191, 2003.
- [14] G. Corbellini, K. Aksit, S. Schmid, S. Mangold, and T. R. Gross, “Connecting networks of toys and smartphones with visible light communication,” *IEEE Communications Magazine*, vol. 52, no. 7, pp. 72–78, July 2014.
- [15] E. Schubert, *Light-Emitting Diodes*. Cambridge University Press, 2006.
- [16] C. Martiny and M. Wendt, “Intrinsic sensing and color control of multiLED lamp-modules,” *Philips Research, Eindhoven, The Netherlands, Tech. Rep. PR-TN 2006/00195*, 2006.
- [17] Y. Zhu, N. Narendran, and Y. Gu, “Investigation of the optical properties of YAG: Ce phosphor,” in *6th International Conference on Solid State Lighting*, p. 63370S, September 2006.
- [18] *Hamamatsu, Characteristic and Use of Infrared Detectors, Technical Information SD-12*. HAMAMATSU, November 2004.
- [19] M. G. Villalva, J. R. Gazoli, and E. R. Filho, “Modeling and circuit-based simulation of photovoltaic arrays,” in *Proceedings Brazilian Power Electronics Conference*, pp. 1244–1254, September 2009.

Chapter 4

Unidirectional visible light communication and illumination with LEDs*

Visible light communication (VLC) with light emitting diodes (LEDs) has attracted interest for interactive and networked lighting control, and consumer infotainment applications. In this paper, we propose a LED system for jointly achieving unidirectional VLC while providing flicker-free illumination. At the transmitter, a redundant run-length limited encoding scheme and multi-level dimming is considered for data transmission, with a wide dimming range. The receiver uses on-off keying (OOK) and uses the OFF periods for VLC reception. It is allowed to be asynchronous to the transmitter, with a phase offset within a preset range. A key feature of the proposed system is that no dedicated devices are used for transmission/reception, with the LEDs used for these functions. We design a functional prototype of this system and evaluate the communication bit error rate and illumination flicker performance experimentally.

*This chapter has been published as: S. Li, A. Pandharipande and F. M. J. Willems, “Unidirectional visible light communication and illumination with LEDs”, *IEEE Sensors Journal*, vol. 16, no. 23, pp. 8617-8626, October 2016.

4.1 Introduction

Visible light communication (VLC) refers to communication in the visible part of the electromagnetic spectrum. In VLC, information is transmitted by modulating the light output of the transmitting device to a receiving device that can decode the information. Given the flexibility with which light emitting diodes (LEDs) can be controlled, VLC with LEDs has attracted significant attention. A number of applications in interactive and networked lighting control, consumer electronics, indoor positioning and connected vehicles [1], [2], [3], [4], [5], [6], have considered LED based VLC. Many of these applications require low-medium data rates, with a minimal impact on illumination. In this paper, we consider a system with a LED transmitter and LED receiver that achieves VLC, while providing flicker-free illumination. A key feature of the proposed system is that no dedicated light sensors are used for VLC reception; the LEDs provide illumination and also serve as VLC receivers.

A number of works have considered VLC systems with LEDs as transmitters and photodetectors as VLC receivers [1], [7], [8], [9], [10], [11], [12]. A dual-purpose LED driver with a constant current source and a buck converter was proposed in [7] for illumination control and VLC transmission using variable pulse position modulation. In [1], the performance of an indoor LED lighting system that provides illumination and VLC with photodetectors was analyzed. A hybrid VLC scheme to support communication between luminaires and off-the-shelf cameras as well as photodetectors was considered in [12]. In [8], a platform for distributed, multi-hop VLC was presented. Full-duplex VLC across luminaires in an indoor lighting system was proposed in [9], [10], with advanced signal processing techniques for dealing with self-interference at photodetectors. The reader is referred to [11] for a recent overview on VLC.

While the property of LEDs as spectrum-selective light sensors has been known [13], [14], their use for sensing in lighting applications has received closer attention only recently [15], [16]. The use of LEDs as receivers has been further explored in [17], [18], [19], [20] to achieve VLC for LED-to-LED communications in consumer toys and entertainment applications. Due to the nature of these applications, limited attention was given to illumination constraints. Simple PHY and MAC layer protocols to enable slotted communications with LED devices were considered in these works. Fast synchronization schemes with a dedicated synchronization preamble [17, 18] or idle patterns [19] before each frame were considered. An improvement was proposed in [20] by considering a physical layer protocol based on a slotting structure and 2-pulse position modulation for data transmission. Two dedicated synchronization intervals were used to determine the direction of phase offset between two devices. To compensate phase offset, the

duration of the following ON slot was either increased or decreased. An embedded Linux platform with an opto-electronic transceiver front-end, OpenVLC, was presented in [21] for LED-to-LED communications with software-based primitives such as sampling, symbol detection and coding/decoding. Using this platform, intra-frame bidirectional VLC was presented in [22]. In [23], [24], Manchester encoding with on-off keying (OOK) was considered for two-way VLC with LEDs for enhancing the system data rates and synchronization methods were proposed.

The primary function of LEDs is to provide illumination. Given the interest in LED based VLC applications, we consider the question: can VLC transmission and reception be achieved with LEDs, without using dedicated transmitters/receivers, while providing illumination? We show design feasibility of such a system in this paper. We consider unidirectional VLC between two LED devices in a peer-to-peer topology. The two LED devices have identical design. Each device can be configured with software to serve either as a VLC transmitter or a receiver. A number of technical challenges arise in such a design.

- [i] How should information be encoded at the LED VLC transmitter that facilitates decoding at the LED receiver?
- [ii] How does the decoding mechanism work, given that the LED is used for both VLC reception and providing illumination?
- [iii] How should the LED system be designed to realize reliable VLC and flicker-free illumination?

These challenges are addressed in subsequent sections in this paper. At the transmitter, data is encoded using a standard run-length limited (RLL) code with carefully added redundancy bits to facilitate decoding. The encoded data is modulated using on-off keying and added to a pulse width modulation (PWM) signal waveform, which is then transmitted. The receiver is allowed to be asynchronous, in particular, with a phase offset locked within a preset range. The receiver is OOK modulated with 50% duty cycle, and the OFF periods are used for VLC reception. We design a functional single LED prototype transmitter/receiver and evaluate the performance of the system. The communication performance, in terms of bit error rate (BER), and illumination flicker performance of the system are studied experimentally.

4.2 System structure

In this section, we provide an overview of the VLC system structure. The proposed system is illustrated in Fig. 5.1, wherein a transmitter communicates to

CHAPTER 4. UNIDIRECTIONAL VISIBLE LIGHT COMMUNICATION AND ILLUMINATION WITH LEDs

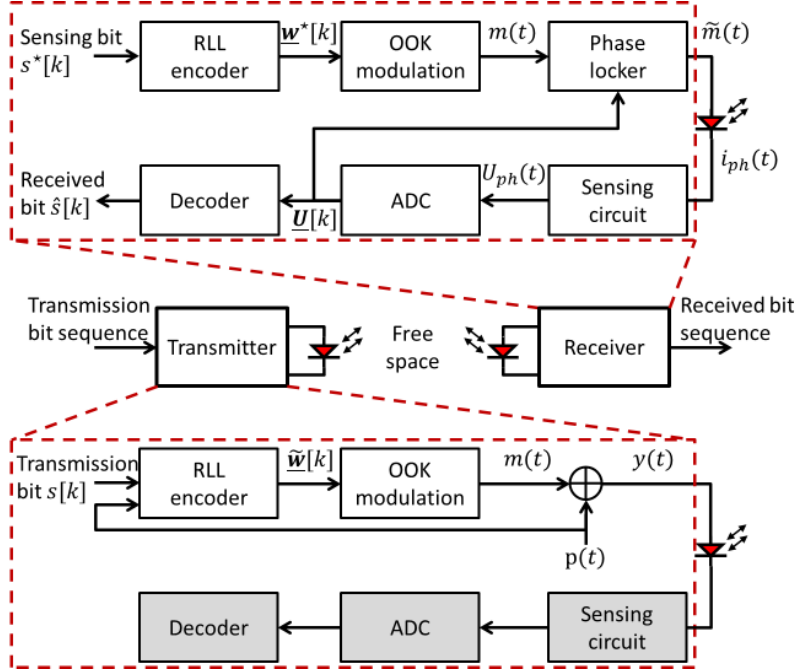


Figure 4.1: System structure and transmitter/receiver block diagrams.

a receiver by emitting an optical signaling waveform. The receiver modulates its light output in such a way that the transmitted optical signal can be decoded while providing flicker-free illumination using the same LED. The input of the transmitter is a bit sequence, with the k -th transmission bit denoted by $s[k]$. It is encoded using a xByB RLL encoder into a binary codeword $\underline{w}[k] = (w_1[k], \dots, w_y[k])$. To aid decoding, we add redundant bits to $\underline{w}[k]$ and denote the redundant codeword by $\tilde{\underline{w}}[k]$. The resulting codeword is OOK modulated into a square waveform $m(t)$ and added to a carrier waveform $p(t)$. Signal $p(t)$ is a PWM waveform with a duty cycle Q . Further, signal $p(t)$ is fed into the RLL encoder to aid injection of redundant bits. The superposed waveform $y(t)$ is the optical signal emitted by the LED. The sensing circuit, analog-to-digital converter (ADC) and decoder are activated only in receiving mode.

The input of the receiver is a dedicated sensing bit sequence with the k -th bit denoted by $s^*[k]$. It is selected such that the corresponding codeword $\underline{w}^*[k] = (\dots, 0, 1, 0, 1, 0, 1, \dots)$ is with equal number of 1s and 0s. It is OOK modulated into a signal $m(t)$ that directly dims the LED with a 50% duty cycle square wave. The same LED is used to receive $y(t)$ in the OFF periods of $m(t)$. A sensing circuit is built to convert the photocurrent signal $i_{ph}(t)$ into

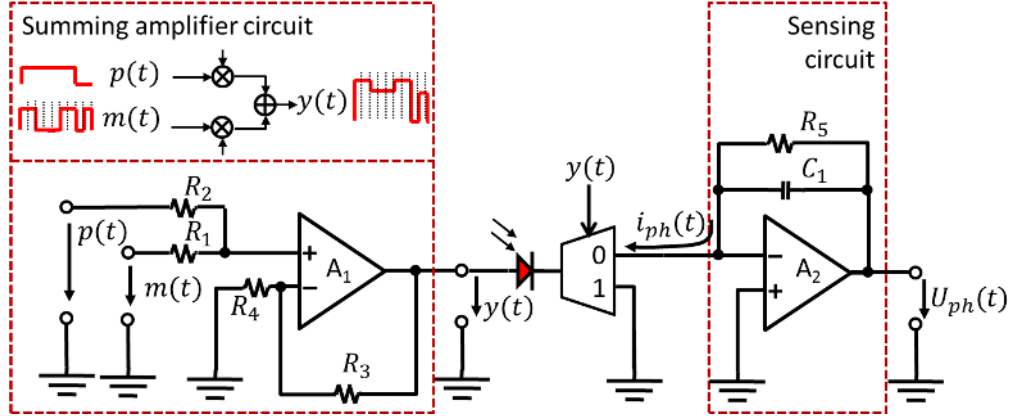


Figure 4.2: Transmitter/receiver front-end schematic.

a voltage signal $U_{ph}(t)$, which is sampled and quantized into a sample vector $\underline{U}[k] = (U_1[k], \dots, U_N[k])$. A decoder is built to recover $s[k]$ from the partially received optical signal. The output of the decoder is a received bit $\hat{s}[k]$. Further, the sample vector $\underline{U}[k]$ is fed into a phase-lock unit that keeps the transmitter and the receiver asynchronous. Specifically, their phase-offset is locked within a preset range, which aids correct decoding. The phase-lock unit outputs a waveform $\tilde{m}(t)$ as a shift of signal $m(t)$. The sensing circuit, encoder, decoder and phase-lock unit are detailed in the following sections.

4.3 Front-end design

The schematic of the transmitter/receiver front-end is shown in Fig. 4.2, including a LED, a summing amplifier circuit and a sensing circuit. The summing amplifier generates a multi-level dimming signal $y(t)$ in volt as a weighted sum of the PWM signal $p(t)$ in volt and the modulation signal $m(t)$ in volt, given by

$$\begin{aligned}
 y(t) &= \frac{R_3 + R_4}{R_4} \cdot \frac{\frac{m(t)}{R_1} + \frac{p(t)}{R_2}}{\frac{1}{R_1} + \frac{1}{R_2}} \\
 &= G_{A1} \cdot \left(\frac{\alpha}{1 + \alpha} m(t) + \frac{1}{1 + \alpha} p(t) \right).
 \end{aligned} \tag{4.1}$$

The weighting factors are determined by resistors R_1 to R_4 , among which $\frac{R_3 + R_4}{R_4}$ is the op-amp gain G_{A1} and $\frac{R_2}{R_1}$ defines the modulation index α ($0 < \alpha \leq 1$). Due to the non-linear current-voltage characteristic of LEDs, the cathode pin of

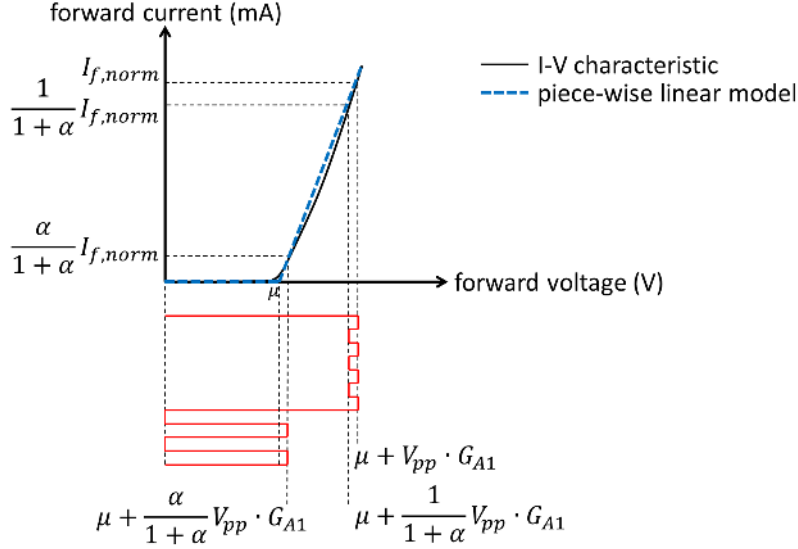


Figure 4.3: LED current-voltage characteristic and its piece-wise linear model.

the LED is reverse-biased to provide the minimum forward voltage μ . This is better understood with the piece-wise linear model of LED current-voltage I-V characteristic shown in Fig. 4.3. We assume that signals $p(t)$ and $m(t)$ have an equal amplitude V_{pp} and stay in phase. Their frequencies f_p and f_m are above twice the mains frequency for flicker-free illumination. There are W number of xByB RLL codewords carried per PWM cycle. The waveform $y(t)$ is directly applied to the LED for dimming. Its peak amplitude and the maximum rated forward voltage $V_{f,\max}$ of the LED satisfy:

$$G_{A1} \cdot V_{pp} < V_{f,\max} - \mu. \quad (4.2)$$

In addition to dimming, signal $y(t)$ also configures a multiplexer that interfaces the LED to a sensing circuit. For $y(t) > 0$, the LED is forward-biased to emit light. For $y(t) = 0$, the LED is zero-biased to generate a photocurrent $i_{ph}(t)$ in response to the received optical signals. The sensing circuit implements a transimpedance amplifier (TIA) and outputs a photovoltage signal

$$U_{ph}(t) = R_5 \cdot i_{ph}(t). \quad (4.3)$$

The photocurrent $i_{ph}(t)$ is linearly related to the incident radiation intensity by the LED responsivity \mathfrak{R}_λ . A noise-reducing capacitor C_1 is connected to the feedback resistor R_5 for better stability.

We now formulate the design trade-off between communication and illumination performance. The dimming level λ ($0 < \lambda < 100\%$) is determined by the ratio between the average of $y(t)$ per T_p cycle to the nominal LED forward voltage $V_{f,\text{norm}}$ minus μ . It is calculated as follows.

1. We first consider $Q = 1$. Due to DC balance of the RLL codeword, signal $m(t)$ has a 50% duty cycle and is added to a DC voltage level. The resulting dimming level is

$$\begin{aligned}\lambda^{(1)} &= \frac{1}{2} \cdot \frac{G_{A1} \cdot V_{pp}}{V_{f,\text{norm}} - \mu} + \frac{1}{2} \cdot \frac{1}{1 + \alpha} \cdot \frac{G_{A1} \cdot V_{pp}}{V_{f,\text{norm}} - \mu} \\ &= \frac{2 + \alpha}{2 + 2\alpha} \cdot \beta,\end{aligned}\tag{4.4}$$

$$\text{with } \beta = \frac{G_{A1} \cdot V_{pp}}{V_{f,\text{norm}} - \mu} \quad (1 \leq \beta < \frac{V_{f,\text{max}} - \mu}{V_{f,\text{norm}} - \mu}).$$

2. We then consider $Q = 0$. The LED is purely driven by a modulation signal $m(t)$ with a 50% duty cycle, which results in a dimming level

$$\begin{aligned}\lambda^{(0)} &= \frac{1}{2} \cdot \frac{\alpha}{1 + \alpha} \cdot \frac{G_{A1} \cdot V_{pp}}{V_{f,\text{norm}} - \mu} \\ &= \frac{\alpha}{2 + 2\alpha} \cdot \beta.\end{aligned}\tag{4.5}$$

Assume $\beta = 1$, for any $0 < Q < 1$. We calculate the dimming level by

$$\begin{aligned}\lambda &= Q \cdot \lambda^{(1)} + (1 - Q) \cdot \lambda^{(0)}, \\ &= Q \cdot \frac{2 + \alpha}{2 + 2\alpha} \cdot \beta + (1 - Q) \cdot \frac{\alpha}{2 + 2\alpha} \cdot \beta, \\ &\stackrel{\beta=1}{=} \frac{2}{2 + 2\alpha} \cdot Q + \frac{\alpha}{2 + 2\alpha}.\end{aligned}\tag{4.6}$$

Therefore, the dimming level λ is influenced by the modulation index α . Specifically, a small α has the advantage of a wide dimming range at the cost of reduced signal-to-noise ratio. Thus, in applications where illumination matters, a transmitter can configure $\alpha = 0.1$ in order to achieve a wide dimming range between 5% and 95%. For systems where illumination can be traded for reliable communication, the transmitter may configure $\alpha = 1$ resulting in a dimming range between 25% and 75%.

4.4 Physical layer protocol

The PHY layer protocol contains mechanisms for redundant RLL encoding/decoding, semi-synchronization and flicker mitigation.

CHAPTER 4. UNIDIRECTIONAL VISIBLE LIGHT COMMUNICATION
AND ILLUMINATION WITH LEDS

Algorithm 1 Redundant encoding scheme

- 1: *Input 1*: any x-bit to y-bit RLL encoder
- 2: *Input 2*: $W \cdot x$ number of transmission bits \underline{s}
- 3: *Input 3*: the duty cycle Q of PWM signal $p(t)$
- 4: *Output*: a bit sequence $\underline{\tilde{w}} = (b_1, \dots, b_{z+4})$, $z = W \cdot y$
- 5: RLL codewords $(w_1, \dots, w_z) \leftarrow \text{xByB_encoder}(\underline{s})$
- 6: $p(t)$ falling edge position $I \leftarrow \lfloor \frac{T_p}{T_b} \cdot Q \rfloor$
- 7: $b_1 \leftarrow 1$
- 8: $(b_2, \dots, b_{I-1}) \leftarrow (w_1, \dots, w_{I-2})$
- 9: $(b_I, b_{I+1}) \leftarrow (1, 0)$
- 10: $(b_{I+2}, \dots, b_{z+3}) \leftarrow (w_{I-1}, w_z)$
- 11: $b_{z+4} \leftarrow 0$

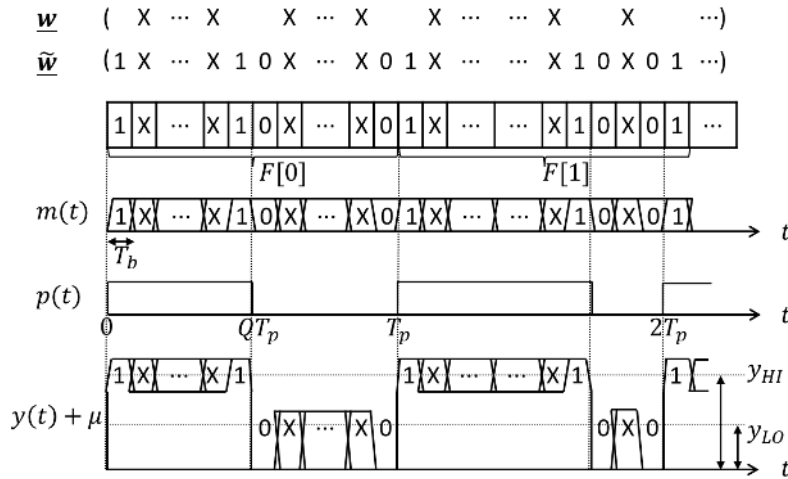


Figure 4.4: Frame structure and the corresponding waveform.

4.4.1 Encoding scheme and PHY frame structure

We explain the redundant encoder using the pseudo code in Algorithm 1. The encoder takes a sequence of transmission bits \underline{s} as input. It first derives a sequence of RLL codeword bits $\underline{w} = (w_1, \dots, w_z)$ with length $z = W \cdot y$ bits using an existing xByB RLL encoder. The encoder then adds 4 redundant bits at certain positions. Two redundant bits $(b_{z+4}, b_1) = (0, 1)$ are added at position of the rising edge of PWM signal $p(t)$. Another pair of bits $(b_I, b_{I+1}) = (1, 0)$ are added at the falling edge position I . As such, there are $I - 2$ number of RLL codeword bits transmitted in the ON period of signal $p(t)$, and $z - I + 2$ number of codeword

Algorithm 2 Decoding scheme

```

1: Input: sample vector  $\underline{U}[k]$  at  $k$ -th bit duration
2:  $\underline{D}[k] \leftarrow \nabla \underline{U}[k]$ 
3:  $d[k] \leftarrow \underset{D_n[k] \in \{D_1[k], D_2[k], \dots, D_{N-1}[k]\}}{\operatorname{argmax}} |D_n[k]|$ 
4: if  $d[k] > \Gamma$  then
5:    $(\hat{s}[k], \hat{s}[k+1]) \leftarrow (0, 1)$ 
6: else if  $d[k] < -\Gamma$  then
7:    $(\hat{s}[k], \hat{s}[k+1]) \leftarrow (1, 0)$ 
8: else
9:   if  $U_{\frac{N}{2}}[k] > \gamma$  then
10:     $(\hat{s}[k], \hat{s}[k+1]) \leftarrow (1, 1)$ 
11:   else
12:     $(\hat{s}[k], \hat{s}[k+1]) \leftarrow (0, 0)$ 
13: Output: a pair of received bits  $(\hat{s}[k], \hat{s}[k+1])$ .

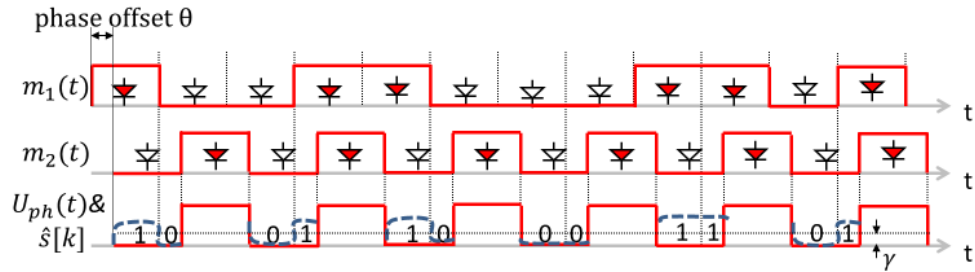
```

bits transmitted in its OFF period. The encoder outputs a codeword vector $\tilde{\underline{w}}$ with a total of $z + 4$ bits. This codeword vector is still DC-balanced since the redundant bits are with equal number of 1s and 0s per T_p cycle.

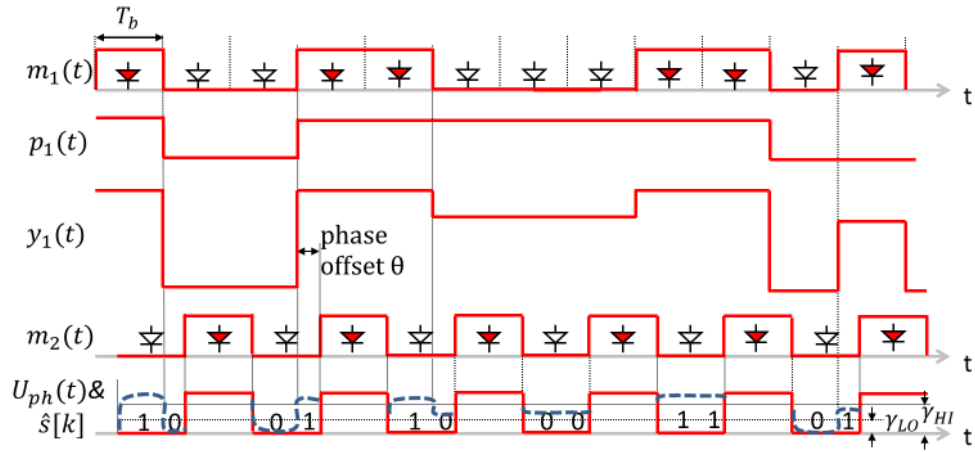
We now describe the PHY frame structure. Fig. 5.3 illustrates two PHY frames $F[0]$ and $F[1]$. Each frame consists of a $(z + 4)$ -bit codeword vector $\tilde{\underline{w}}$ that is output by the encoder. We denote the bits in \underline{w} with 'X' and highlight the redundant bits in $\tilde{\underline{w}}$. The corresponding modulation signal $m(t)$ is time-aligned with the beginning of a PWM cycle and is depicted over cycles. We assume the PWM cycle T_p is an integer multiple of the bit duration T_b . The ratio $\kappa = \frac{T_p}{T_b}$ determines the number of levels that the PWM duty cycle Q can reach. An exemplary signal $y(t)$ that is biased by μ is depicted in Fig. 5.3 for better understanding of the multi-level dimming scheme.

4.4.2 Decoding scheme

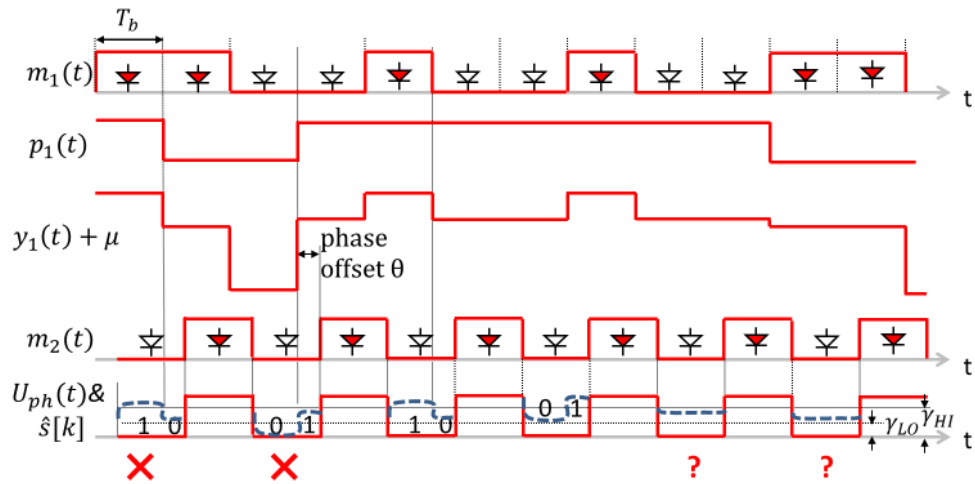
We explain the decoding scheme using the pseudo code in Algorithm 2. The input of the decoder is an N -dimensional sample vector $\underline{U}[k] = (U_1[k], \dots, U_N[k])$. We detect edges in $\underline{U}[k]$ using its first-order derivative $\underline{D}[k] = (D_1[k], \dots, D_{N-1}[k])$, which is approximated by the difference between two consecutive samples (current sample minus the previous one). A scalar variable $d[k]$ is assigned with the derivative that has the maximum absolute value, from which we derive two received bits $(\hat{s}[k], \hat{s}[k+1])$. The mapping relation is listed in steps 4 to 12 and can be better understood using the exemplary signaling waveforms shown in Fig. 5.4.



(a) Decoding of bi-level dimming signal $m_1(t)$.



(b) Decoding of multi-level dimming signal $y_1(t)$.



(c) Failed decoding of multi-level dimming signal $y_1(t)$.

Figure 4.5: Decoding scheme.

It illustrates an asynchronous communication between a transmitter L1 and a receiver L2 with a phase-offset $\theta > 0$.

We start with decoding of a bi-level signal $m_1(t)$ as shown in Fig. 4.5a. L1 does not add redundant bits since $Q = 0$. In the OFF period of $m_2(t)$, L2 measures a photovoltage signal $U_{ph}(t)$ in response to $m_1(t)$. It is highlighted with the blue dashed curve and is used for decoding in two steps:

1. The decoder first calculates $d[k]$ (step 3 in Algorithm 2). The case $d[k] > \Gamma$, where $\Gamma > 0$ implements a band gap option, indicates a rising edge in response to the transmission of $(s[k], s[k+1]) = (0, 1)$. Similarly, $d[k] < -\Gamma$ maps to the transmission of $(s[k], s[k+1]) = (1, 0)$. If all derivatives fall into the band gap $[-\Gamma, \Gamma]$, the decoder continues with step 2.
2. This step implements thresholding:

$$(\hat{s}[k], \hat{s}[k+1]) = \begin{cases} (0, 0) & , \frac{1}{N} \sum_{j=1}^N U_j[k] < \gamma, \\ (1, 1) & , \text{otherwise,} \end{cases}$$

where $\gamma > 0$ is a threshold voltage.

Decoding of a multi-level dimming signal requires a threshold that is adaptive to the signal $p(t)$. Specifically, the receiver uses a larger threshold for $0 < t < QT_p$ and a smaller one for $QT_p < t < T_p$. An exemplary decoding of a multi-level dimming signal $y_1(t)$ that is biased by μ is shown in Fig. 4.5b. L2 uses γ_{HI} for thresholding in ON period of $p_1(t)$ and γ_{LO} in its OFF period. Therefore, L2 needs to detect the moment when the signal $p(t)$ switches between ON and OFF periods, so as to select a proper value of γ for thresholding. We consider respectively the rising edge and falling edge detection.

1. Rising edge detection: the receiver detects a rising edge of $p(t)$ signal if $d[k] > \gamma_{\text{HI}}$ or an element in $\underline{U}[k]$ becomes greater than γ_{HI} .
2. Falling edge detection: the receiver detects a falling edge if $d[k] < -\gamma_{\text{HI}}$ or an element in $\underline{U}[k]$ drops close to 0.

This edge detection approach makes use of the redundant bits added at the edge positions of signal $p(t)$ and can be verified with the signal $U_{ph}(t)$ shown in Fig. 4.5b. Knowledge of edges of $p(t)$ in turn allows the decoder to remove the redundant bits.

Redundancy-aided decoding not only correctly relates $d[k]$ to the transmitted bits $(s[k], s[k+1])$, but also benefits with an adaptive thresholding that is independent of the modulation index α . Fig. 4.5c illustrates the failure of decoding signal

CHAPTER 4. UNIDIRECTIONAL VISIBLE LIGHT COMMUNICATION
AND ILLUMINATION WITH LEDS

$y_1(t)$ without redundancy. Error bits are observed when $(s[k], s[k + 1]) = (0, 0)$ and $(s[k], s[k + 1]) = (1, 1)$ are transmitted at the edge positions of $p_1(t)$. Further, L2 cannot determine a proper value of γ to compare with in the last two sensing intervals, especially when the modulation index α approaches 1 (signals $m_1(t)$ and $p_1(t)$ are with similar amplitudes).

Threshold γ can be derived from a calibration phase, during which a PHY frame is communicated from a certain distance d . At the transmitter side, we can derive two voltage levels y_{HI} and y_{LO} (see Fig. 5.3) as

$$y_{\text{HI}} = \frac{1}{2} \left(G_{\text{A1}} \cdot V_{pp} + \frac{1}{1 + \alpha} \cdot G_{\text{A1}} \cdot V_{pp} \right) + \mu,$$

$$y_{\text{LO}} = \frac{1}{2} \cdot \frac{\alpha}{1 + \alpha} \cdot G_{\text{A1}} \cdot V_{pp} + \mu.$$

At the receiver side, we calculate two threshold values

$$\gamma_{\text{HI}} = \Phi(y_{\text{HI}}(t), d) \cdot \mathfrak{R}_\lambda \cdot R_5,$$

$$\gamma_{\text{LO}} = \Phi(y_{\text{LO}}(t), d) \cdot \mathfrak{R}_\lambda \cdot R_5,$$

where $\Phi\{\cdot\}$ relates the LED forward voltage to the light intensity measured from the distance d . The threshold value is then given by

$$\gamma = \begin{cases} \gamma_{\text{HI}} & , 0 < t < QT_p, \\ \gamma_{\text{LO}} & , QT_p < t < T_p. \end{cases}$$

The proposed calibration scheme assumes a fixed communication distance between the two LED devices and that the external light conditions do not change rapidly. In order to support low mobility scenarios and be robust against ambient light changes (e.g. slow daylight variations), an adaptive threshold scheme may be employed. This topic is beyond the scope of the current work and is a topic of further investigation.

4.4.3 Semi-synchronization scheme

So far, we have assumed a phase-offset $\theta > 0$ between L1 and L2. In practice θ may decrease to 0 due to the clock drift. Exemplary waveforms corresponding to $\theta = 0$ are shown in Fig. 4.6a, wherein the receiver L2 detects only one bit per sensing interval. Consequently, decoding fails when two neighboring transmission bits are different.

In this section, we describe the phase-lock unit (Fig. 5.1), which implements a semi-synchronization scheme to achieve a sufficient phase-offset for correct decoding. In Fig. 4.6b, optical waveforms are shown, depicting how a receiver is

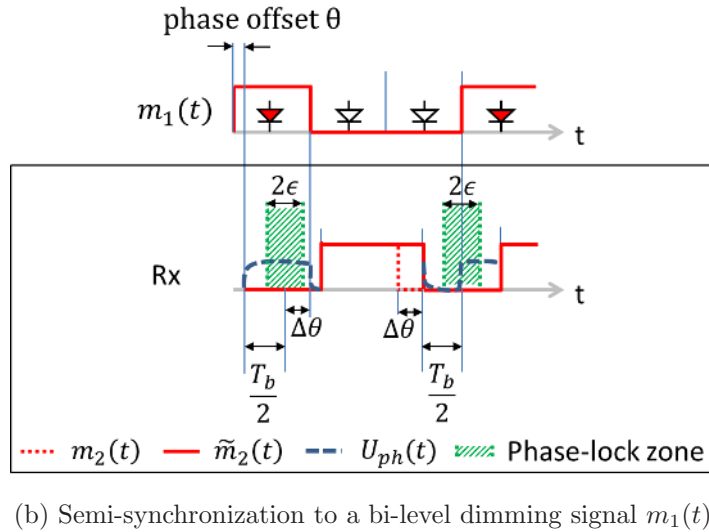
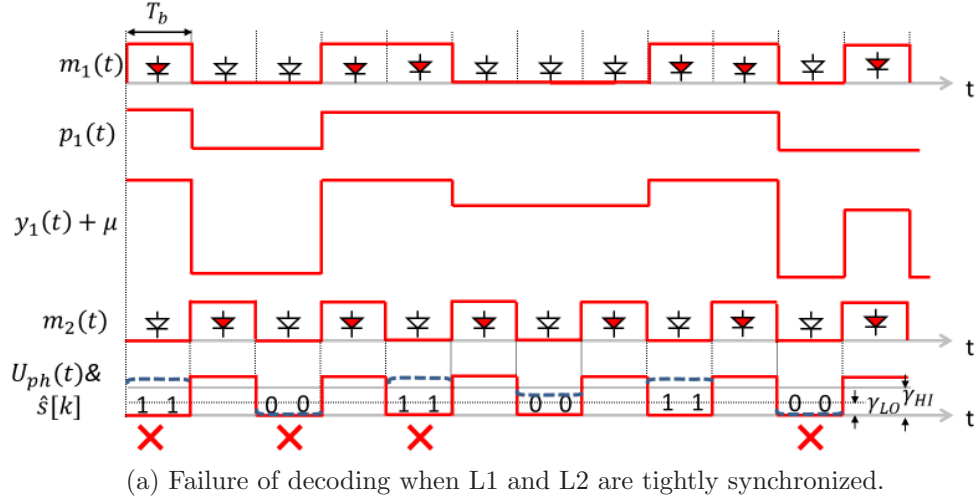


Figure 4.6: Semi-synchronization.

semi-synchronized to a bi-level dimming signal $m_1(t)$. We define a phase-lock zone that is centered at the middle of a sensing interval of the receiver and has a range $\left(\frac{T_b}{2} - \epsilon, \frac{T_b}{2} + \epsilon\right)$. The receiver first determines the position of edge $d[k]$ in $\underline{D}[k]$ (step 3 in Algorithm 2), χ . Based on the relative position of χ and the

phase-lock zone, the phase-lock unit outputs a shifted waveform $\tilde{m}_2(t)$ given as

$$\tilde{m}_2(t) = \begin{cases} m_2(t + \Delta\theta), & \chi \in (0, \epsilon) \\ m_2(t - \Delta\theta), & \chi \in \left(\frac{T_b}{2} + \epsilon, T_b\right) \\ m_2(t), & \text{otherwise.} \end{cases}$$

We define $\Delta\theta$ as the deviation of $d[k]$ from the center of the phase-lock zone and measure it in second by

$$\Delta\theta = \left| \chi - \lfloor \frac{N}{2} \rfloor \right| \cdot \frac{1}{f_s},$$

where N and f_s are respectively the sample vector $\underline{U}[k]$ dimension and the ADC sampling frequency.

Phase compensation applies only if $d[k]$ drifts out of the phase-lock zone and is disabled otherwise. Note that there is no synchronization overhead since the receiver reuses its sensing interval for both decoding and the measurement of $\Delta\theta$. Further, the transmitter and receiver communicate asynchronously for most of the time, enabled by the 2ϵ -wide phase-lock zone.

4.4.4 Flicker mitigation

In multi-level dimming and PWM dimming techniques, attention should be given to the flicker that may result. The flicker threshold is influenced by several factors, including the frequency of the light modulation and modulation depth. In this section, we evaluate both the visible and non-visible parts of flicker that is potentially produced by the proposed dimming scheme.

Visible flicker is usually perceived at frequencies below twice the mains frequency f_0 ($f_0 = 100$ Hz for a 50 Hz mains frequency and $f_0 = 120$ Hz for a 60 Hz mains frequency). Therefore, to eliminate visible flicker, the frequency of the PWM signal $p(t)$ is constrained as

$$\frac{1}{T_p} > f_0 \Rightarrow T_p < \frac{1}{f_0}.$$

Since T_p corresponds to the PHY frame length and each frame consists of $(z + 4)$ number of T_b slots, an upper bond of T_b is

$$T_b < \frac{1}{z + 4} \cdot \frac{1}{f_0}, \quad (Q > 0).$$

For $Q = 0$, $y(t) = m(t)$ and the LED is driven by the modulated square wave with its OFF period determined by the run-length of 0 bits in the RLL codeword.

Denote the maximum run-length of 0 bits with Ω_0 , we have another upper bound of T_b for $Q = 0$ as

$$\frac{1}{\Omega_0 \cdot T_b} > f_0 \Rightarrow T_b < \frac{1}{f_0 \cdot \Omega_0}, \quad (Q = 0).$$

Evaluation on non-visible flicker is of concern due to its physiological and stroboscopic effects. We quantify the non-visible flicker produced by the proposed coding scheme using two metrics: percent flicker and flicker index [25].

Percent flicker

Percent flicker ρ is defined as the difference between the minimum and maximum light output E during a flicker waveform cycle:

$$\rho = \frac{E_{\max} - E_{\min}}{E_{\max} + E_{\min}}.$$

Accordingly, we derive ρ within a complete T_p cycle as

$$\rho(t) = \begin{cases} \rho^{\text{ON}} = \frac{\Phi\{G_{A1} \cdot V_{pp} + \mu\} - \Phi\{G_{A1} \cdot \frac{1}{1+\alpha} \cdot V_{pp} + \mu\}}{\Phi\{G_{A1} \cdot V_{pp} + \mu\} + \Phi\{G_{A1} \cdot \frac{1}{1+\alpha} \cdot V_{pp} + \mu\}}, & 0 < t < QT_p \\ \rho^{\text{OFF}} = \frac{\Phi\{G_{A1} \cdot \frac{\alpha}{1+\alpha} \cdot V_{pp} + \mu\} - 0}{\Phi\{G_{A1} \cdot \frac{\alpha}{1+\alpha} \cdot V_{pp} + \mu\} + 0} = 1, & QT_p < t < T_p, \end{cases}$$

where ρ^{ON} and ρ^{OFF} are percent flicker values in the ON and OFF periods of $\rho(t)$. The average percent flicker per T_p cycle is therefore the weighted sum

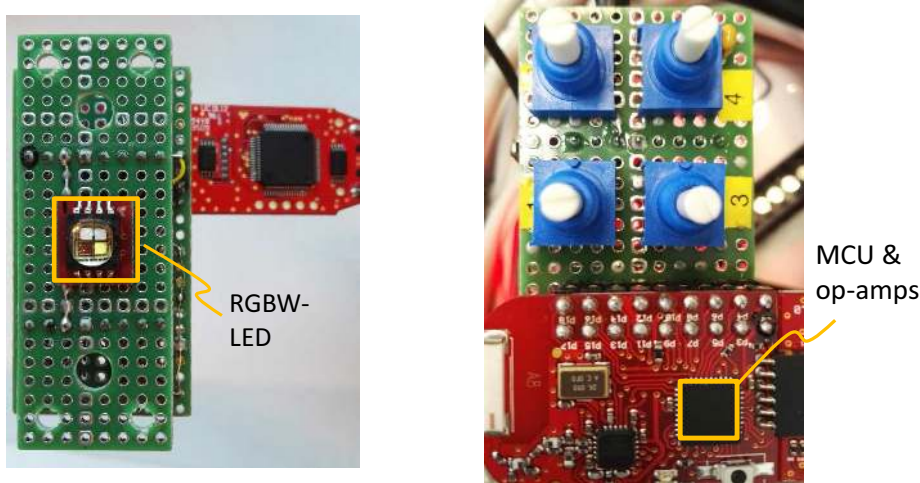
$$\bar{\rho} = Q\rho^{\text{ON}} + (1 - Q)\rho^{\text{OFF}}. \quad (4.7)$$

Flicker index

Flicker index σ is the ratio of the area that lies between dimming signal $y(t) + \mu$ and its average, to the entire area below $y(t) + \mu$ during one T_p cycle. The average flicker index per T_p is given by

$$\bar{\sigma} = \frac{\oint \Phi\{y(t) + \mu\} dt}{\int_0^{T_p} \Phi\{y(t) + \mu\} dt}, \quad (4.8)$$

where the numerator is a line integral of $\Phi\{y(t) + \mu\}$ along a curve that shapes the area between $y(t) + \mu$ and its average. Obviously, both $\bar{\rho}$ and $\bar{\sigma}$ are functions of duty cycle Q . Their relationship is studied experimentally in Section 6.6.



(a) Side A with a commercial RGBW color LED as transceiver front-end. (b) Side B with MCU, integrated op-amps and resistor network.

Figure 4.7: Designed prototypes.

4.5 Experimental Results

In this section, we describe our prototype implementation and evaluate the system performance.

4.5.1 Prototype implementation

The two sides of the designed prototype are shown in Fig. 6.9. Side A consists of a single CREE XLamp MC-E color LED with individually addressable red, green, blue and white (RGBW) color LED chips in one package. We select the red LED chip and drive it with two general purpose input / output (GPIO) ports of a micro-controller unit (MCU) MSP430F2274 on side B. The rated values for the red LED chip are $V_{f,\text{norm}} = 2.1$ V, $V_{f,\text{max}} = 2.5$ V and $\mu = 1.8$ V. The MCU integrates two op-amps which implement the summing amplifier circuit and TIA. An internal feedback resistor network (R_3 and R_4 in Fig. 4.2) of the op-amp A1 is used to configure its gain G_{A1} . Since it is difficult to directly provide a negative voltage $-\mu = -1.8$ V (Fig. 4.2), the LED cathode pin is connected to ground. To compensate, the MCU programs the op-amp gain G_{A1} in such a way that the LED is properly biased. The DC offset μ serves as a design parameter, which makes the proposed PHY protocol applicable to any LED devices that are dimmed with either current or voltage signals. For example, if $m(t)$, $p(t)$ and

$y(t)$ are current signals, the LED light output is linearly related to the amplitude of signal $y(t)$. Accordingly, we simply set $\mu = 0$. The TIA is connected to a feedback resistor $R_5 = 500 \text{ k}\Omega$ and a noise reducing capacitor $C_1 = 2.2 \text{ pF}$. It outputs a photovoltage $U_{ph}(t)$ that is sampled by a 10-bit ADC on the MCU. The ADC operates at a sampling frequency $f_s = 200 \text{ kHz}$ and converts $N = 30$ samples per T_b slot. The resulting sample vector $\underline{U}[k]$ is filtered with a 3-tap median filter in order to reduce the shot noise. The filter output is fed to the decoder that is implemented in MCU software.

Two prototypes L1 and L2 are placed at a distance $d = 10 \text{ cm}$, communicating via a line-of-sight (LOS) path. We configure L1 to be the transmitter and L2 the receiver. L1 implements a standard 4B6B RLL encoder and transmits 10^4 codeword bits to L2. Two 4B6B codewords and four redundant bits form one PHY frame, which has 16 bits in total. Each frame is carried in one PWM cycle. We choose $T_p = 8 \text{ ms}$ and $T_b = 500 \text{ }\mu\text{s}$ for flicker-free illumination. The communication and illumination performance trade-off is evaluated using two configurations of the modulation index: $\alpha = 1$ and $\alpha = 0.1$.

4.5.2 Calibration and semi-synchronization

Before communication, we first calibrate the threshold values γ_{HI} and γ_{LO} using the above settings. Fig. 4.8 illustrates the waveform of $y_1(t) + \mu$ on channel 0 and $m_2(t) + U_{ph}(t)$ on channel 1 of a NI ELVISmx oscilloscope. Three cursors values $U_{ph}(t_1)$, $U_{ph}(t_2)$ and $U_{ph}(t_3)$ correspond to the peak light intensity when the transmitting LED is respectively driven by $p_1(t) + m_1(t)$, $p_1(t)$ and $m_1(t)$. Two threshold values are derived as

$$\gamma_{\text{HI}} = \frac{U_{ph}(t_1) + U_{ph}(t_2)}{2} \approx \begin{cases} 693 \text{ mV}, & \alpha = 1, \\ 1090 \text{ mV}, & \alpha = 0.1. \end{cases}$$

Similarly, we derive

$$\gamma_{\text{LO}} = \frac{U_{ph}(t_3) + 0}{2} \approx \begin{cases} 184 \text{ mV}, & \alpha = 1, \\ 80 \text{ mV}, & \alpha = 0.1. \end{cases}$$

Threshold values γ_{HI} and γ_{LO} are converted to ADC values and locally stored at the MCU of L2, which implements the multi-level decoding scheme listed in Algorithm 2 with a band-gap option $\Gamma = 30 \text{ mV}$. The decoded bits are communicated to a computer, where the bit error rate is calculated. In order to better demonstrate the impact of phase offset on communication performance, the BER value is calculated per 100 decoded bits and is plotted over 100 samples. The sampling period T_s is around 180 ms.

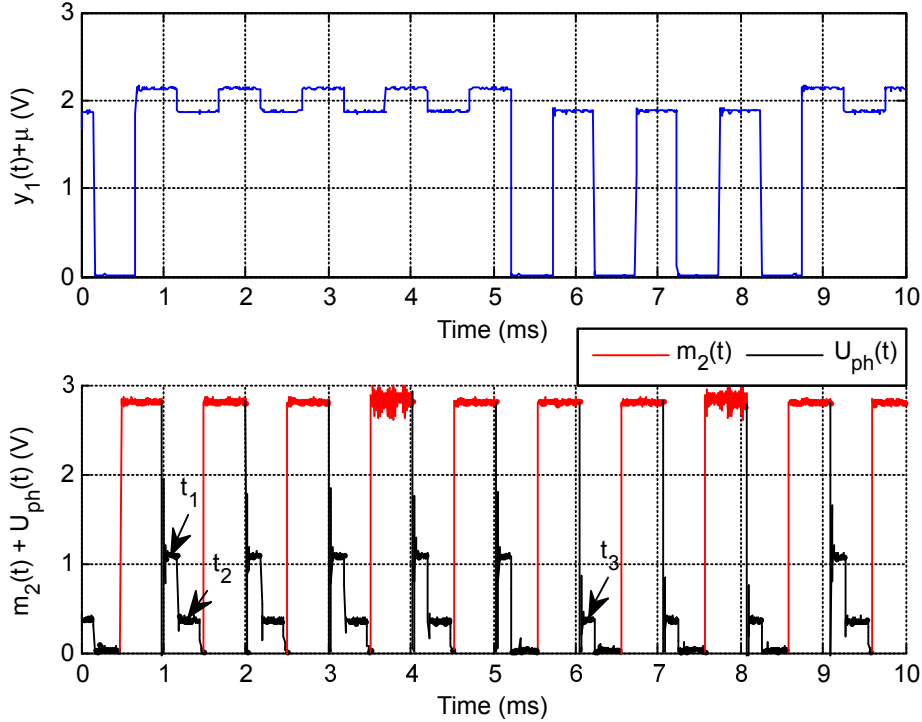


Figure 4.8: Waveform depicting threshold calibration ($\alpha = 1$).

The BER values given by a drifted transmitter and receiver are shown in Fig. 4.9. About 75 samples are with zero bit error and are replaced by a 10^{-6} value in the log scale plot. The remaining BER values are in a range between 0.05 and 0.5 due to clock drift between L1 and L2. The peak BER values correspond to a scenario wherein L1 and L2 are incidentally in phase. Afterwards, BER values start to decrease as the phase offset accumulates. An ideal eye opening measurement is at the moment when the edges of $y_1(t)$ are aligned with the middle of the L2 sensing interval.

In Fig. 4.10, we show the BER values given by a semi-synchronized transmitter and receiver. We chose $\epsilon = \frac{T_b}{4} = 125 \mu\text{s}$ and show the synchronization frequency and resulting BER values. Again, zero values are replaced by 10^{-6} in the log scale plot. A total of 10^4 data bits are decoded correctly with an average of 1.66 synchronizations per 100 bits (50 ms).

Detailed waveforms of $y_1(t) + \mu$ and $m_2(t) + U_{ph}(t)$ depicting the semi-synchronization process are shown in Fig. 4.11, with $\epsilon = 125 \mu\text{s}$. During the first two sensing intervals (0.5 ms, 1 ms) and (1.5 ms, 2 ms), L2 respectively de-

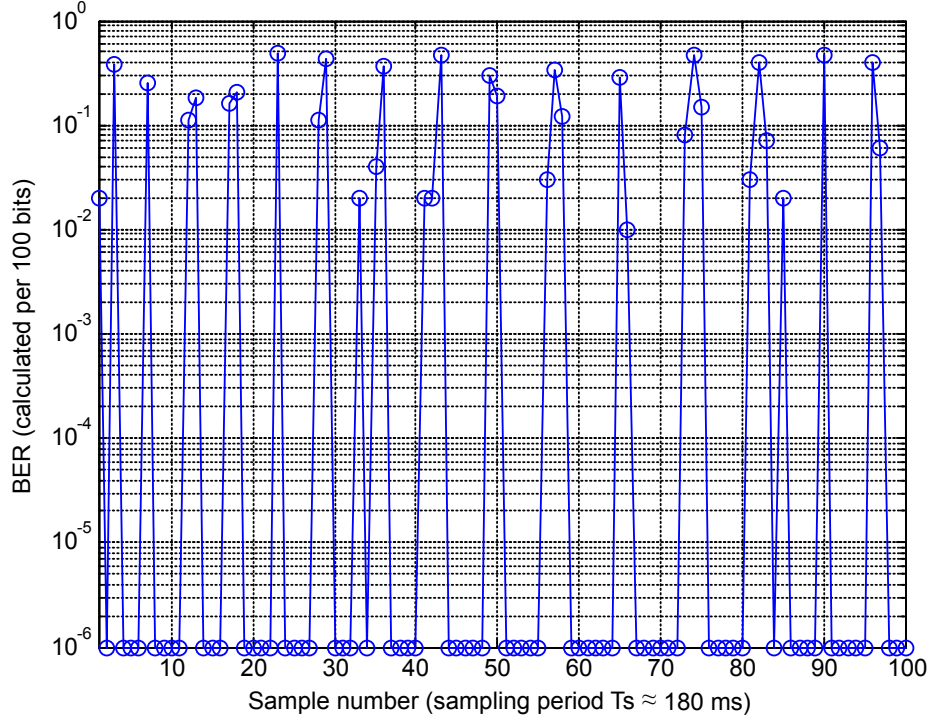


Figure 4.9: BER plot of drifted transmitter and receiver ($\alpha = 1$).

etects a falling edge χ that is within its phase-lock zone and close to the border. Accordingly, L2 does not implement semi-synchronization until the third sensing interval (2.5 ms, 3 ms), during which χ drifts out of the phase-lock zone. Consequently, L2 advances signal $m_2(t)$ by reducing the ON period duration starting around 3 ms. In the fourth sensing interval, L2 observes a edge χ that is aligned with the center of its phase-lock zone.

Frequent semi-synchronization by changing the ON period duration of signal $m_2(t)$ will affect the illuminance level of L2. In order to minimize this impact, L2 would choose a wide phase-lock zone with a theoretical upper bond of $2\epsilon = T_b - \frac{2}{f_s}$. In practice, this bound cannot be achieved due to ringing artifact that is highlighted in Fig. 4.11 using signal $U_{ph}(t)$ at $t \approx 15.5$ ms. It represents the step response of the TIA and is in the form of an overshoot followed by ringing. The amplitude and settling time are determined by the received light intensity $\Phi\{y_1(t) + \mu, d\}$ and the bandwidth [26] of the TIA. In our implementation, L2 has a settling time around 50 μ s. During this time slot L2 cannot detect χ due to a high noise level and the semi-synchronization scheme would fail. Filters

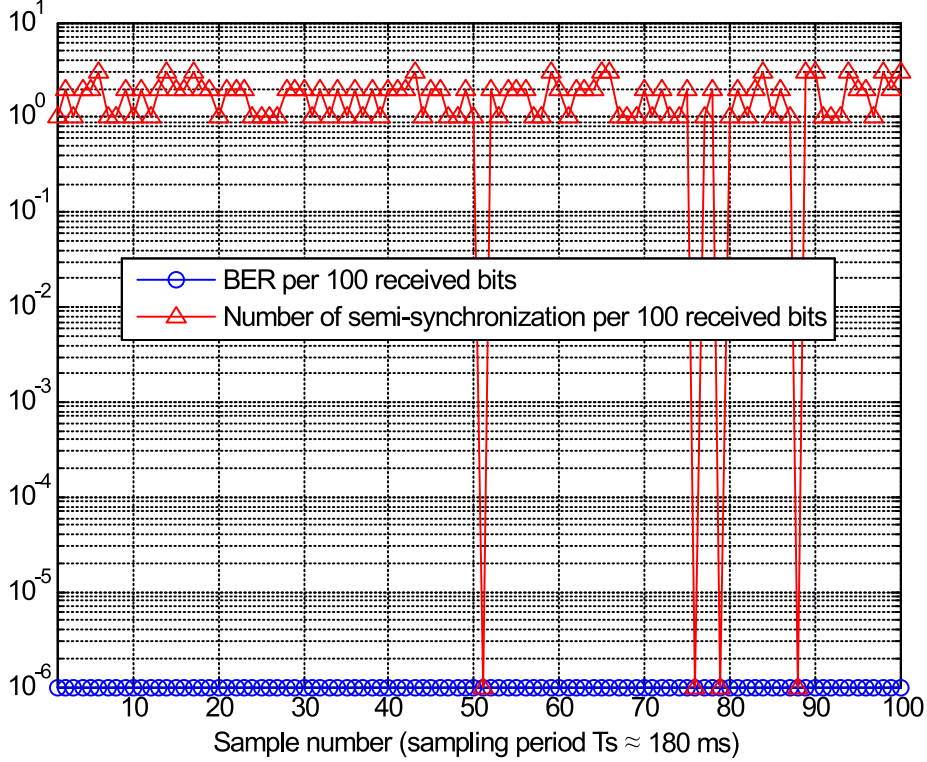


Figure 4.10: BER plot of phase-locked transmitter and receiver ($\alpha = 1$).

exist to eliminate overshoot and reduce ringing, but at the cost of complexity. Instead, L2 assigns its sensing interval with $T_b + 50 \mu\text{s}$ and the ON period of $m_2(t)$ with $T_b - 50 \mu\text{s}$. At the beginning of each sensing interval, L2 has to wait for $50 \mu\text{s}$ before collecting $\underline{U}[k]$. This approach ensures a successful semi-synchronization at a small 5% illuminance loss. Dimming compensation can be achieved by driving LEDs with current that is slightly above its nominal value. We use this approach and study the impact of ϵ on communication performance.

4.5.3 Communication performance

In Fig. 4.12, we demonstrate the impact of the phase-lock zone width on the BER and semi-synchronization frequency. The x-axis is the normalized ϵ range with respect to the bit duration T_b , resulting in a range between 0 and 0.5. We chose a step of $\frac{1}{14}$ according to the dimension of sample vector $\underline{U}[k]$ ($N = 30$). Again, the zero values are replaced by 10^{-6} values in the log scale plot. The BER values

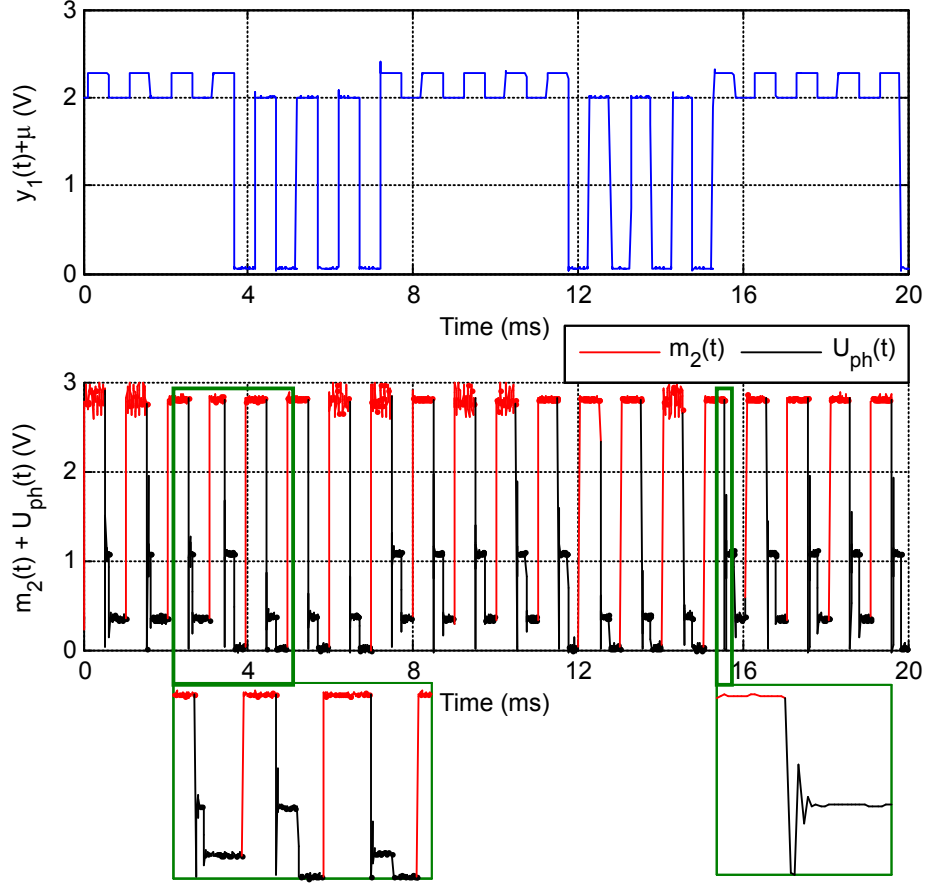


Figure 4.11: Waveform depicting semi-synchronization scheme ($\alpha = 1$).

and the semi-synchronization frequency are averaged over 10^4 decoded bits.

1. We first consider $\alpha = 1$. As ϵ increases from 0 to $\frac{6}{14}T_b$, the semi-synchronization frequency decreases from 6.35 to 0.22. Meanwhile, L2 can still achieve zero bit error rate. In case $\epsilon = \frac{T_b}{2}$, the phase-lock unit allows χ to drift within the entire sensing interval T_b . As such, the synchronization frequency drops to 0. The corresponding BER value increases as a result to 0.022 in this test.
2. For $\alpha = 0.1$, L1 and L2 can stay semi-synchronized in a range between $\epsilon = 0$ and $\epsilon = \frac{6}{14}T_b$. However, the average BER value is around 10^{-4} . This is because the received signal power is 10 times smaller and is comparable to

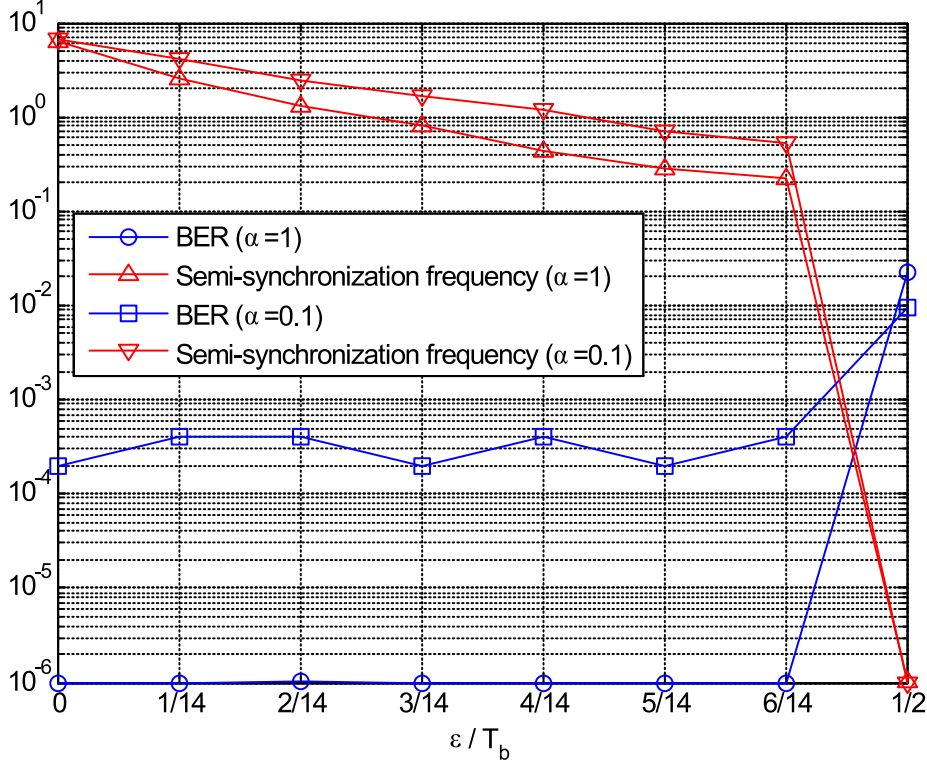


Figure 4.12: Impact of phase-lock zone width on BER and semi-synchronization frequency.

the Johnson noise power from the TIA and the shot noise from the incident light.

The plot of BER vs communication distance is shown in Fig. 4.13. The x-axis is the LOS path distance d , which is varied from 5 cm to 25 cm in steps of 5 cm. The threshold values γ_{HI} and γ_{LO} are calibrated at $d = 10$ cm. The modulation index α equals 1 and the phase-lock zone parameter is $\frac{\epsilon}{T_b} = \frac{3}{14}$. During communication, there is a background light level around 50 lux. The BER value is calculated per 10^5 received bits at each distance. The zero BER values are replaced by 10^{-6} in order to show in the log scale plot. Within a range of ± 5 cm around the calibration distance, unidirectional communication is achieved with BER less than 10^{-3} . BER increases above 10^{-2} at $d = 20$ cm due to reduced signal-to-noise ratio. At $d = 25$ cm, semi-synchronization starts to fail, which increases the BER. Due to the reduced light power with distance, the average of the sample vector $\underline{U}[k]$ decreases and approaches the threshold,

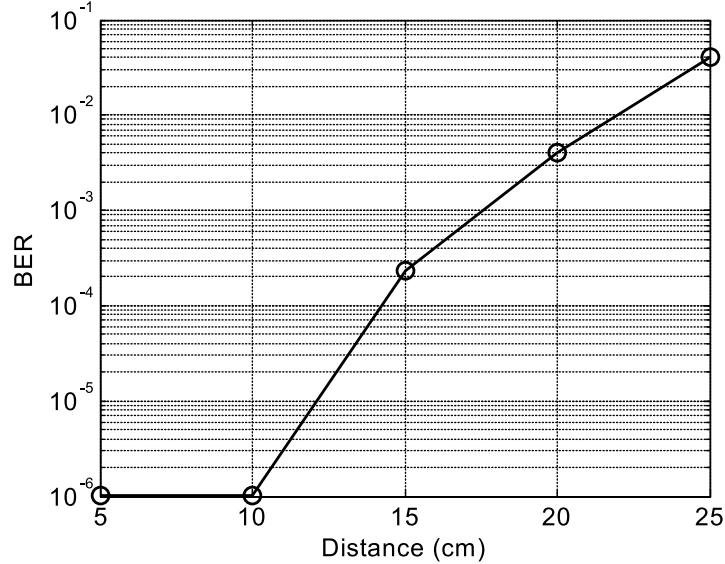


Figure 4.13: Plot of BER over communication distance.

thereby increasing the BER.

4.5.4 Illumination performance

We now evaluate the multi-level dimming performance using two metrics: flicker percent flicker ρ and flicker index σ , which are functions of duty cycle Q . The duty cycle Q of transmitter L1 increases from $\frac{1}{16}$ to $\frac{15}{16}$ at steps of $\frac{1}{16}$. Receiver L2 stays in sensing mode and measures the light intensity $\Phi\{y_1(t) + \mu, d\}$ at a distance $d = 10$ cm. The measurements are collected for one T_p cycle and are communicated to a PC, where $\bar{\rho}$ and $\bar{\sigma}$ are calculated for different Q values using (4.7) and (4.8). Their relationship is shown in Fig. 4.14 and benchmarked against a conventional PWM signal with an amplitude $V_{pp} = V_{f,\text{norm}}$.

1. Percent flicker: in a range between $Q = \frac{3}{16}$ and $Q = \frac{15}{16}$, we achieve a percent flicker $\bar{\rho}$ that is better than the benchmark for both $\alpha = 1$ and $\alpha = 0.1$. At $Q = \frac{1}{16}$, $\bar{\rho}$ equals 1 as a result of a light output that flashes in short and low-frequency bursts. At $Q = \frac{15}{16}$, $\bar{\rho}$ is dominated by the modulation signal $m(t)$ and approaches 50% for $\alpha = 1$ and 5% for $\alpha = 0.1$. The modulation index affects both the dimming range and the percent flicker. Specifically, smaller the value of α , the lower the percent flicker and wider the dimming range.

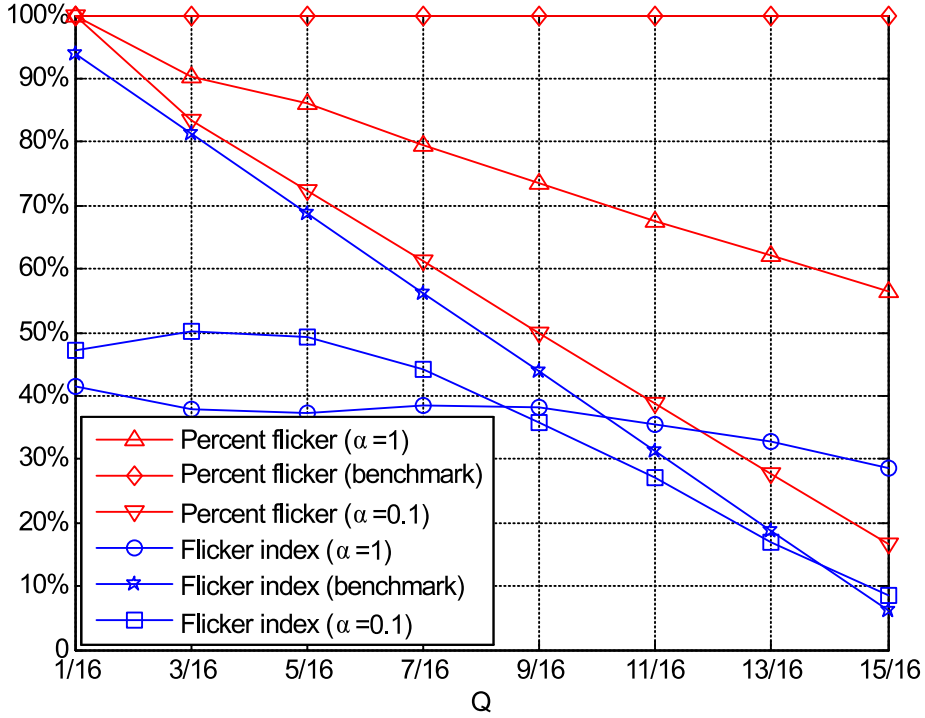


Figure 4.14: Relationship between flicker metrics and duty cycle.

2. Flicker index is influenced by both the modulation index α and the PWM duty cycle Q . In a range between $Q = \frac{1}{16}$ and $Q = \frac{9}{16}$, the flicker index is smaller than the benchmark for both $\alpha = 0.1$ and $\alpha = 1$ due to the existence of signal $m(t)$. As Q increases, the flicker index corresponding to $\alpha = 0.1$ approaches the benchmark since the PWM signal $p(t)$ starts to dominate. On the other hand, the flicker index given by $\alpha = 1$ is worse than the benchmark at $Q \approx 1$, which is caused by the signal $m(t)$ with a 100% modulation depth.

4.6 Conclusions and discussions

We presented the design and evaluation of a prototype system with two LED devices for asynchronous communication while also providing illumination. The devices use the LEDs themselves for data transmission and reception, without additional dedicated light sensors. The built prototype was evaluated in terms of BER and illumination flicker performance. We showed that reliable communica-

tion at a rate of a few kbps was achievable, with illumination flicker comparable to conventional PWM dimming.

Reliable VLC was demonstrated over a short distance (about 10 cm) in this paper with a single LED. When scaling to luminaires with hundreds of LEDs (and possibly high power LEDs), we expect that a VLC range in the order of meters becomes feasible. To see this, consider a transmitter with M LEDs and a receiver with N_e LEDs branches in parallel. It can be shown that the effective VLC range is improved by a factor of $\sqrt{M \cdot N_e}$ [23]. As an example, consider RGB LED strips with 5 tri-color RGB LED chips in series and 24 such branches in parallel, i.e. $M = 5 \times 24 = 120$ and $N_e = 24$. This results in a communication range of $\sqrt{120 \times 24} \times 10 \text{ cm} \approx 536.7 \text{ cm}$.

In the proposed system, there was no acknowledgement (ACK) mechanism. One way of incorporating an ACK signal is by having the two LED devices time-share the channel and switch between transmit and receive operations following a MAC protocol. Yet another possibility is to use bi-directional VLC [24] to incorporate an ACK signal. The design of ACK mechanisms is beyond the scope of this paper and is a topic of further investigation.

The proposed VLC system was considered under a scenario of no mobility, that is, the transmitter and receiver locations were fixed. In some applications, the devices may have limited mobility. In this case, an adaptive threshold technique may be employed wherein the receiver adapts threshold parameters γ_{HI} and γ_{LO} to the incident light power. The design of such schemes and performance evaluation of such systems are topics of future research.

REFERENCES

- [1] T. Komine and M. Nakagawa, “Fundamental analysis for visible-light communication system using LED lights,” *IEEE Transactions on Consumer Electronics*, vol. 50, no. 1, pp. 100–107, February 2004.
- [2] H. Yang, T. C. W. Schenk, J. W. M. Bergmans, and A. Pandharipande, “Enhanced illumination sensing using multiple harmonics for LED lighting systems,” *IEEE Transactions on Signal Processing*, vol. 58, no. 11, pp. 5508–5522, 2010.
- [3] S. Rajagopal, R. D. Roberts, and S. K. Lim, “IEEE 802.15.7 visible light communication: modulation schemes and dimming support,” *IEEE Communications Magazine*, vol. 50, no. 3, pp. 72–82, March 2012.
- [4] G. Corbellini, K. Aksit, S. Schmid, S. Mangold, and T. R. Gross, “Connecting networks of toys and smartphones with visible light communication,” *IEEE Communications Magazine*, vol. 52, no. 7, pp. 72–78, July 2014.
- [5] C. B. Liu, B. Sadeghi, and E. W. Knightly, “Enabling vehicular visible light communication (V2LC) networks,” in *Proceedings of the Eighth ACM International Workshop on Vehicular Inter-networking*, pp. 41–50, 2011.
- [6] 802.15.7 IEEE standard for local and metropolitan area networks, *part 15.7: Short Range Wireless Optical Communication Using Visible Light*, 2011.
- [7] K. Modepalli and L. Parsa, “Dual-purpose offline LED driver for illumination and visible light communication,” *IEEE Transactions on Industry Applications*, vol. 51, no. 1, pp. 406–419, January 2015.
- [8] L. Klaver and M. Zuniga, “Shine: A step towards distributed multi-hop visible light communication,” *IEEE 12th International Conference on Mobile Ad Hoc and Sensor Systems*, pp. 235–243, 2015.
- [9] H. Yang and A. Pandharipande, “Full-duplex relay VLC in LED lighting triangular system topology,” *6th International Symposium on Communications, Control and Signal Processing*, pp. 85–88, May 2014.
- [10] H. Yang and A. Pandharipande, “Full-duplex relay VLC in LED lighting linear system topology,” *Annual Conference of the IEEE Industrial Electronics Society*, pp. 6075–6080, November 2013.

-
- [11] P. H. Pathak, X. Feng, P. Hu, and P. Mohapatra, “Visible light communication, networking, and sensing: A survey, potential and challenges,” *IEEE Communications Surveys Tutorials*, vol. 17, no. 4, pp. 2047–2077, 2015.
- [12] N. Rajagopal, P. Lazik, and A. Rowe, “Hybrid visible light communication for cameras and low-power embedded devices,” in *Proceedings of the 1st ACM MobiCom Workshop on Visible Light Communication Systems*, pp. 33–38, July 2014.
- [13] F. M. Mims, *Siliconconnections: Coming of Age in the Electronic Era*. New York, NY, USA: McGraw-Hill, 1986.
- [14] P. Dietz, W. Yerazunis, and D. Leigh, “Very low-cost sensing and communication using bidirectional LEDs,” *5th International Conference on Ubiquitous Computing*, pp. 175–191, 2003.
- [15] S. Li and A. Pandharipande, “LED-based color sensing and control,” *IEEE Sensors Journal*, vol. 15, no. 11, pp. 6116–6124, November 2015.
- [16] S. Li, A. Pandharipande, and F. M. J. Willems, “Daylight sensing LED lighting system,” *IEEE Sensors Journal*, vol. 16, no. 9, pp. 3216–3223, May 2016.
- [17] D. Giustiniano, N. O. Tippenhauer, and S. Mangold, “Low-complexity visible light networking with LED-to-LED communication,” *IFIP Wireless Days*, pp. 1–8, November 2012.
- [18] S. Schmid, G. Corbellini, S. Mangold, and T. R. Gross, “An LED-to-LED visible light communication system with software-based synchronization,” *IEEE Globecom Workshops*, pp. 1264–1268, December 2012.
- [19] Schmid, Stefan, G. Corbellini, S. Mangold, and T. R. Gross, “LED-to-LED visible light communication networks,” *Proceedings of the Fourteenth ACM International Symposium on Mobile Ad Hoc Networking and Computing*, pp. 1–10, 2013.
- [20] S. Schmid, G. Corbellini, S. Mangold, and T. R. Gross, “Continuous synchronization for LED-to-LED visible light communication networks,” *3rd International Workshop in Optical Wireless Communications*, pp. 45–49, September 2014.
- [21] Q. Wang, D. Giustiniano, and D. Puccinelli, “An open-source research platform for embedded visible light networking,” *IEEE Wireless Communications*, vol. 22, no. 2, pp. 94–100, 2015.

CHAPTER 4. UNIDIRECTIONAL VISIBLE LIGHT COMMUNICATION AND ILLUMINATION WITH LEDS

- [22] Q. Wang and D. Giustiniano, “Intra-frame bidirectional transmission in networks of visible LEDs,” *IEEE/ACM Transactions on Networking*, vol. 24, no. 6, pp. 3607–3619, December 2016.
- [23] S. Li, A. Pandharipande, and F. M. J. Willems, “Redundant run-length limited encoding for two-way visible light communication,” *Annual Conference of the IEEE Industrial Electronics Society*, pp. 4706–4712, October 2016.
- [24] S. Li, A. Pandharipande, and F. M. J. Willems, “Two-way visible light communication and illumination with LEDs,” *IEEE Transactions on Communications*, vol. 65, no. 2, pp. 740–750, February 2017.
- [25] M. S. Rea, *IESNA Lighting Handbook: Reference and Application, Ninth Edition*. New York, NY, USA: Illuminating Engineering Society, 2000.
- [26] T. Wang and B. Erhman, “Compensate transimpedance amplifiers intuitively,” Texas Instruments Application Report No. SBOA055A, March 2005, accessed June 2016. [Online]. Available: <http://www.ti.com/lit/an/sboa055a/sboa055a.pdf>

Chapter 5

Adaptive visible light communication and illumination with LEDs*

Visible light communication (VLC) with light emitting diodes (LEDs) has attracted interest in different applications like consumer infotainment, interactive lighting and networked lighting control. In this paper, we consider a peer-to-peer VLC system wherein an LED is used for both VLC transmission and reception, while providing flicker-free illumination. We specifically propose an adaptive VLC system to extend the reliable communication range and deal with ambient light changes and LED device portability that can occur in indoor VLC applications. At the transmitter, a weighted combination of a pulse width modulation signal and a redundant run-length limited encoded on-off keying (OOK) signal is used for data transmission. The weights are adapted to the target dimming level and to enhance the signal-to-noise ratio. The LED receiver uses OOK and the OFF periods therein for VLC reception. An adaptive threshold detection scheme is proposed for decoding. The communication performance of the proposed system is evaluated with a prototype implementation and compared with a non-adaptive VLC system.

*This chapter has been submitted to: S. Li, A. Pandharipande and F. M. J. Willems, "Adaptive visible light communication and illumination with LEDs", *IEEE Journal on Selected Areas in Communications Special Issue on Localisation, Communication and Networking with VLC*.

5.1 Introduction

Visible light communication (VLC) refers to optical communication in the visible part, 375–780 nm, of the electromagnetic spectrum. In VLC, the light output of the transmitting device is modulated to embed information that can be received and decoded at a receiving device. Given the flexibility with which light emitting diodes (LEDs) can be controlled, VLC with LEDs has attracted significant attention in applications like consumer electronics, interactive and networked lighting control [1–5]. Many of these applications require low-medium data rates, with a minimal impact on illumination. For such applications, there has been recent interest in the use of LEDs for both VLC transmission and reception [6–11]. This is in contrast to works [12–14] where high data rate VLC systems have been considered with LEDs and *dedicated* light sensors. For a recent review on indoor VLC, see [15].

While the spectrum-selective light sensing property of LEDs as light sensors has been known for long [16, 17], it has been only recently exploited for indoor lighting applications like color sensing [18] and daylight sensing [19]. The use of LEDs as receivers has been further explored in [6–9] to achieve VLC for LED-to-LED communications in consumer toys and entertainment applications, and in [10, 11] to achieve two-way VLC and for unidirectional VLC in [20] while maintaining certain illumination constraints. A key feature of such systems is that no dedicated light sensors are used for VLC reception; the LEDs provide illumination and also serve as VLC receivers. We consider operational scenarios where the ambient light levels may vary and the LED devices have limited portability, thus limiting the effective communication range of such VLC systems. To address this problem, we consider an *adaptive VLC* system, with parameter adaptation at both the transmitter and the receiver.

Simple PHY and MAC layer protocols to enable slotted communications with LED devices using 2-pulse position modulation were considered in [6–9]. An embedded Linux platform with an opto-electronic transceiver front-end, Open-VLC, was presented in [21] for LED-to-LED communications with software-based primitives such as sampling, symbol detection and coding/decoding. Using this platform, intra-frame bidirectional VLC was presented in [22]. In [10, 11], Manchester encoding with on-off keying (OOK) was considered for two-way VLC with LEDs for enhancing the system data rates and synchronization methods were proposed.

In [20], unidirectional VLC between two LED devices in a peer-to-peer topology was considered. At the transmitter, data was encoded using a standard run-length limited (RLL) code with carefully added redundancy bits to facilitate decoding. The encoded data was modulated using OOK and added to a pulse

width modulation (PWM) signal waveform, which was then transmitted. The receiver was OOK modulated with 50% duty cycle, and the OFF periods were used for VLC reception. The receiver and transmitter were allowed to be asynchronous, in particular, with a phase offset locked within a preset range. The proposed calibration scheme at the receiver in [20] assumed a fixed communication distance between the two LED devices and that the ambient light conditions did not change rapidly. Ambient light changes (e.g. slow daylight variations) can however limit the effective communication range in such a system.

To address this problem, we consider an adaptive VLC system. At the transmitter side, we consider a weighted combination of a PWM signal and a redundant RLL encoded OOK signal. The weights are designed to achieve a target dimming level and enhance the transmit signal-to-noise ratio (SNR), that in turn increases the effective communication range. At the receiver, a method for adaptive threshold detection is proposed to deal with ambient light changes and device portability. We compare the proposed adaptive VLC system with the non-adaptive VLC system [20] in terms of bit error rate (BER) performance using an experimental single LED system prototype.

5.2 System structure

In this section, we provide an overview of the VLC system structure. The proposed system is illustrated in Fig. 5.1, wherein a transmitter communicates an information bit sequence to a receiver, while providing a preset dimming level. The receiving LED is OOK modulated and receives the transmitted optical signal when in OFF state.

One input of the transmitter is the information bit sequence $\underline{\mathbf{s}}$. Every x bits of $\underline{\mathbf{s}}$ is encoded using a standard xByB RLL encoder into a y -bit codeword $\underline{\mathbf{w}} = (w_1, \dots, w_y)$. The codeword is DC-balance, with equal number of 1s and 0s. To aid decoding, the transmitter inserts redundant bits into the codeword at positions that are determined by the duty cycle Q of a PWM dimming signal $p(t)$. The updated codeword, denoted by $\tilde{\underline{\mathbf{w}}}$, is modulated into a square wave signal $m(t)$ using OOK. Signals $m(t)$ and $p(t)$ are weighted and summed, resulting in a voltage signal $y(t)$,

$$y(t) = c_m m(t) + c_p p(t). \quad (5.1)$$

The weighting factors c_m and c_p are functions of the modulation index α ($0.1 \leq \alpha \leq 1$). Both the duty cycle Q and the modulation index α are derived from a look-up table (LUT), whose entry is a target dimming level λ^* as another transmitter input. Signal $y(t)$ is DC-biased, with μ being the LED switch-ON

CHAPTER 5. ADAPTIVE VISIBLE LIGHT COMMUNICATION AND ILLUMINATION WITH LEDS

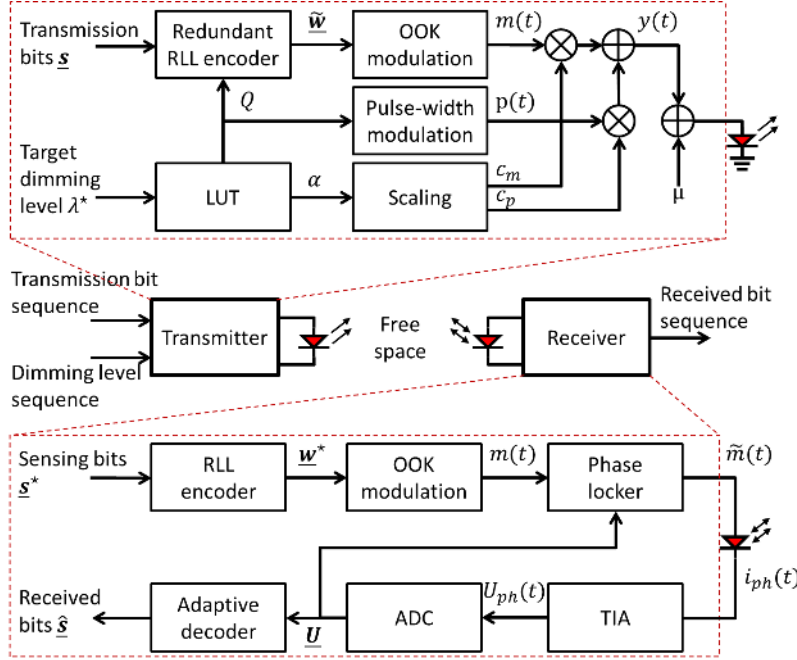


Figure 5.1: System structure and transmitter/receiver block diagrams.

voltage. The DC offset μ can be better understood from the LED piece-wise linear model [23] in Fig. 5.2. We assume that signals $m(t)$ and $p(t)$ are with unit amplitude and show an exemplary waveform of signal $y(t) + \mu$ below the I-V curve in Fig. 5.2. A scalar voltage value V_{margin} determines a range $[\mu, \mu + V_{\text{margin}}]$, within which the LED can be safely dimmed by applying a forward voltage $y(t) + \mu$. The final output is a voltage signal $y(t) + \mu$, which drives the transmitting LED.

The input of the receiver is a dedicated sensing bit sequence \underline{s}^* . It is selected such that the corresponding RLL codeword $\underline{w}^* = (\dots, 0, 1, 0, 1, 0, 1, \dots)$ is with alternating 1 and 0. It is OOK modulated into a signal $m(t)$ that directly dims the LED at a 0.5 dimming level. The same LED is used to receive optical signals in the OFF periods of $m(t)$. A transimpedance amplifier (TIA) is used to convert the photocurrent signal $i_{ph}(t)$ into a voltage signal $U_{ph}(t)$, which is sampled and quantized into a sample vector $\underline{U} = (U_1, \dots, U_N)$ with a 10-bit analog-to-digital converter (ADC). An adaptive decoder is designed to recover \underline{s} from the partially received optical signal, offering robustness to ambient light changes within a certain range. The output of the decoder is a received bit $\hat{\underline{s}}$. Further, the sample vector \underline{U} is fed into a phase lock unit. It locks the phase-

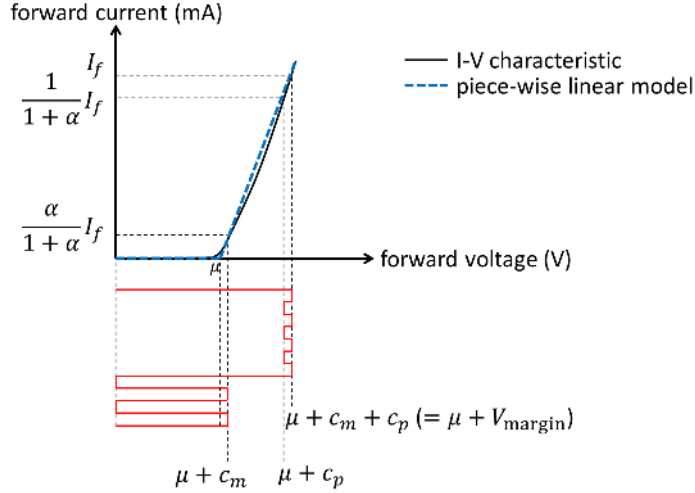


Figure 5.2: LED current-voltage characteristic and its piece-wise linear model.

offset between the transmitter and the receiver within a preset range, which aids correct decoding. The phase lock unit outputs a waveform $\tilde{m}(t)$ as a shift of signal $m(t)$. The phase lock unit has been described in our previous work [20]. In the following two sections, we explain the adaptive functionality of the transmitter and the receiver.

5.3 Adaptive VLC transmitter

In this section, we first formulate the trade-off between illumination and communication performance, which motivates the adaptation of modulation index α to the target dimming level λ^* . Then, the proposed adaptive modulation scheme is described in detail.

5.3.1 Redundant encoder and frame structure

Let W be the number of xByB RLL codewords carried per frame and each frame is transmitted per PWM period. With xByB RLL encoder, every x information bits are encoded into y codeword bits. To encode a frame, the encoder takes a sequence of transmission bits $\underline{s} = (s_1, \dots, s_{W \times x})$ as input. It first derives a sequence of RLL codeword bits $\underline{w} = (w_1, \dots, w_z)$ with length $z = W \times y$ bits using an existing xByB RLL encoder. We denote the bits in \underline{w} with 'X'. We assume that both the PWM period T_p and its ON period QT_p are integer multiple

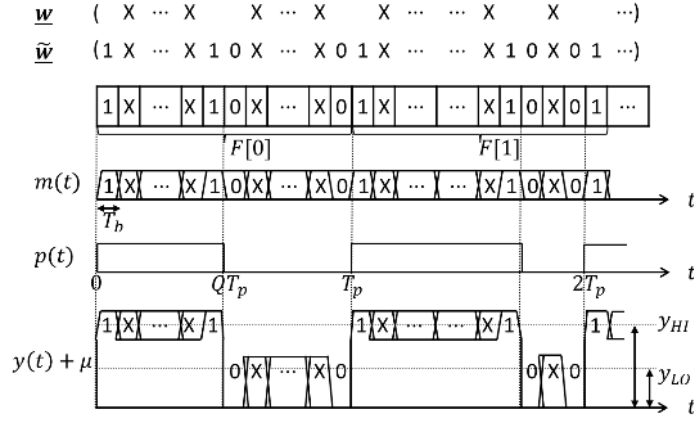


Figure 5.3: Frame structure and redundant encoding.

of bit duration T_b , as shown in Fig. 5.3. To aid decoding, the encoder adds 4 redundant bits at certain positions. Two redundant bits (0, 1) are added at the rising edge of the PWM signal $p(t)$. Another pair of bits (1, 0) are added at the falling edge position. In Fig. 5.3, the redundant bits in \tilde{w} are highlighted. Each frame consists of a $(z + 4)$ -bit codeword vector \tilde{w} that is output by the encoder. Two exemplary PHY frames $F[0]$ and $F[1]$ are illustrated Fig. 5.3. The existence of redundant bits determines the upper and lower bounds of PWM duty cycle Q ,

$$\frac{2}{z+4} \leq Q \leq \frac{z+2}{z+4}. \quad (5.2)$$

In case $Q = \frac{2}{z+4}$, there is no codeword bits transmitted in the ON period of PWM signal. Only two redundant bits (1, 1) are carried. In case $Q = \frac{z+2}{z+4}$, there is no codeword bits but a pair of redundant bits (0, 0) in the OFF period of PWM signal.

5.3.2 Dimming support

Assuming signals $m(t)$ and $p(t)$ are with unit amplitude, we define the modulation index α as the ratio between the amplitude of the weighted OOK signal and the amplitude of the weighted PWM carrier signal:

$$\alpha = \frac{c_m}{c_p} \quad (0.1 \leq \alpha \leq 1), \quad (5.3)$$

where $c_m = \frac{\alpha}{1+\alpha}V_{\text{margin}}$ and $c_p = \frac{1}{1+\alpha}V_{\text{margin}}$. The transmitter achieves a dimming level given by

$$\begin{aligned}\lambda(Q, \alpha) &= \frac{Qc_p + \frac{1}{2}c_m}{V_{\text{margin}}} \\ &= \frac{2}{2+2\alpha}Q + \frac{\alpha}{2+2\alpha},\end{aligned}\tag{5.4}$$

which reflects the trade-off between illumination and communication performance. Specifically, a small α (e.g. $\alpha = 0.1$) has the advantage of achieving a wide dimming range at the cost of reduced SNR. For systems where illumination can be traded for reliable communication, the transmitter may increase α (e.g. $\alpha = 1$). Given a target dimming level λ^* , multiple (Q, α) pairs can satisfy $\lambda(Q, \alpha) = \lambda^*$. Among these solutions, the transmitter chooses the largest possible α in order to enhance SNR. This is realized by the adaptive modulation scheme.

5.3.3 Adaptive modulation

We propose an adaptive scheme, based on table lookup, to achieve the target dimming level λ^* while increasing the SNR. The lookup table relates an achieved dimming level range $[\lambda(\frac{2}{z+4}, \alpha), \lambda(\frac{z+2}{z+4}, \alpha)]$ to a certain modulation index α . The dimming level range reflects the contribution of PWM signal on illumination given a certain modulation index. The tables consists of ten entries corresponding to $\alpha \in \{0.1, 0.2, \dots, 1.0\}$. For each α , the transmitter achieves a dimming range with a lower bound of $\lambda(\frac{2}{z+4}, \alpha)$. This is because there are at least two bits (a pair of redundant bits (1, 1)) in the ON period of signal $p(t)$. Similarly, the upper bound of a dimming range is determined by $\lambda(\frac{z+2}{z+4}, \alpha)$, since there are at least two bits (a pair of redundant bits (0, 0)) in the OFF period of signal $p(t)$. Given a target dimming level λ^* , the transmitter first finds the maximum value of α from the lookup table that satisfies the constraint

$$\lambda(\frac{2}{z+4}, \alpha) \leq \lambda^* \leq \lambda(\frac{z+2}{z+4}, \alpha).\tag{5.5}$$

It then calculates Q using Eq.(5.4) for the selected α and the target dimming level λ^* .

We show an exemplary lookup table in Table 5.1. We select $z = 30$, i.e. 30 codeword bits are transmitted per frame, so as to achieve a maximum dimming range between 0.1 and 0.9 when $\alpha = 0.1$. Let the target dimming level $\lambda^* = 0.75$. The transmitter first searches Table 5.1 and determines the maximum possible modulation index to be $\alpha = 0.7$. It then calculates the PWM duty cycle to be

Table 5.1: Lookup table for adaptation of modulation index.

Dimming range	α	Dimming range	α
[0.0989, 0.9011]	0.1	[0.2243, 0.7757]	0.6
[0.1324, 0.8676]	0.2	[0.2405, 0.7595]	0.7
[0.1606, 0.8394]	0.3	[0.2549, 0.7451]	0.8
[0.1849, 0.8151]	0.4	[0.2678, 0.7322]	0.9
[0.2059, 0.7941]	0.5	[0.2794, 0.7206]	1.0

$Q \approx 0.9250$ using Eq. (5.4). To make the PWM signal period T_p an integer multiple of bit duration T_b , the ON period of signal $p(t)$ is chosen as

$$\begin{aligned}
 QT_p &= R\{[Q(z+4)]\}T_b, \\
 &= R\{[0.9250 \times 34]\}T_b, \\
 &= R\{32\}T_b, \\
 &= 32T_b,
 \end{aligned} \tag{5.6}$$

where the function $R\{a\}$ is given by

$$R\{a\} = \begin{cases} 2, & \text{if } a < 2, \\ z+2, & \text{if } a > z+2, \\ a, & \text{otherwise.} \end{cases} \tag{5.7}$$

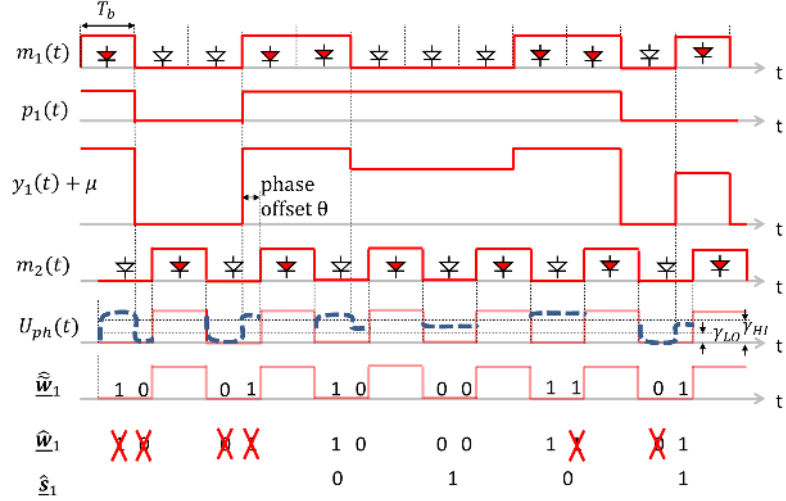
This limits QT_p in a valid range between $2T_b$ and $(z+2)T_b$. The rounding error is evaluated in Section 6.6.

5.4 Adaptive VLC receiver

At the receiver side, we first briefly introduce the LED sensing front-end, the phase-lock unit and the decoder. We refer the reader to our previous work [20] for design details, and primarily focus on the adaptive threshold scheme proposed to improve the system robustness against ambient light changes and support limited LED device portability.

5.4.1 LED sensing front-end and phase-lock unit

At the moment a receiving LED is switched OFF (i.e. in the OFF period of OOK signal $m(t)$), it is zero-biased to sense the optical signal. Specifically, it converts the photocurrent signal $i_{ph}(t)$ into a photovoltage signal $U_{ph}(t)$ using


 Figure 5.4: Decoding of multi-level dimming signal $y_1(t)$.

a transimpedance amplifier. Signal $U_{ph}(t)$ is sampled and fed to the phase-lock unit. It locks the phase-offset between the transmitter and the receiver within a preset range, which aids correct decoding.

5.4.2 Decoder

Waveforms depicting the decoding of a multi-level signal $y(t)$ are shown in Fig.5.4. We add lower index to signals $m(t)$, $p(t)$ and $y(t)$ in order to differentiate between transmitter L1 and receiver L2. The receiver L2 measures a photovoltage signal $U_{ph}(t)$ in response to the transmitted optical signal $y_1(t)$. It is highlighted with the dashed curve. We define an index, $k = 1, 2, \dots$, to denote the k -th sensing interval at receiver L2, i.e. the k -th OFF period of signal $m_2(t)$ in Fig. 5.4. During the k -th sensing interval, the measured photovoltage signal $U_{ph}(t)$ is sampled and quantized into a sample vector $\mathbf{U}^k = (U_1^k, \dots, U_N^k)$ and is used to decode two transmitted bits $(\hat{w}_{2k-1}, \hat{w}_{2k})$ in two steps:

1. The decoder first calculates sample differences of the sample vector \mathbf{U}^k and finds the one with maximum absolute value, $|d^k|$. The case $d^k > \Gamma$, where $\Gamma > 0$ implements a band gap option, indicates a rising edge in response to the transmission of $(\tilde{w}_{2k-1}, \tilde{w}_{2k}) = (0, 1)$. Similarly, $d^k < -\Gamma$ maps to the transmission of $(\tilde{w}_{2k-1}, \tilde{w}_{2k}) = (1, 0)$. If all differences fall into the band gap $[-\Gamma, \Gamma]$, the decoder continues with step 2.

2. This step implements thresholding:

$$(\hat{w}_{2k-1}, \hat{w}_{2k}) = \begin{cases} (0, 0) & , \frac{1}{N} \sum_{j=1}^N U_j^k < \gamma, \\ (1, 1) & , \text{otherwise,} \end{cases} \quad (5.8)$$

where $\gamma > 0$ is a threshold voltage and equals

$$\gamma = \begin{cases} \gamma_{\text{HI}} & , 0 < t < QT_p, \\ \gamma_{\text{LO}} & , QT_p < t < T_p, \end{cases} \quad (5.9)$$

$\gamma_{\text{HI}} > 0$ and $\gamma_{\text{LO}} > 0$ are threshold values in volt. They are used respectively in ON and OFF periods of signal $p(t)$ for thresholding (Eq. (5.8)). Threshold values γ_{HI} and γ_{LO} can be obtained in a calibration phase [20], during which a PHY frame is communicated at a fixed distance under stable ambient light conditions. Decoding of a multi-level dimming signal requires a threshold that is adaptive to the signal $p(t)$. Therefore, L2 needs to detect the moment when the signal $p(t)$ switches between ON and OFF periods, so as to select a proper value of γ for thresholding. We consider respectively the rising edge and falling edge detection.

1. Rising edge detection: the receiver detects a rising edge of $p(t)$ signal if $d^k > \gamma_{\text{HI}}$ or an element in $\underline{\mathbf{U}}^k$ becomes greater than γ_{HI} .
2. Falling edge detection: the receiver detects a falling edge if $d^k < -\gamma_{\text{HI}}$ or an element in $\underline{\mathbf{U}}^k$ becomes less than γ_{LO} .

This edge detection approach makes use of the redundant bits added at the edge positions of signal $p(t)$ and can be verified with the signal $U_{ph}(t)$ shown in Fig. 5.4. Knowing the edges of $p(t)$ in turn allows decoder to remove the redundant bits from $\hat{\underline{\mathbf{w}}}_1$, resulting in an estimated codeword $\hat{\underline{\mathbf{w}}}_1 = (1, 0, 0, 0, 1, 1)$ and an estimated information bit sequence $\hat{\underline{\mathbf{x}}}_1 = (0, 1, 0, 1)$.

5.4.3 Adaptive threshold

We propose an adaptive threshold scheme, by which γ_{HI} and γ_{LO} are adapted to dynamic ambient light conditions and communication distance changes. We assume a portability scenario and slow ambient light fluctuation such that the impact on the receiver measurement can be regarded as a constant offset during communication of at least one PHY frame. Under this condition, the photovoltage samples that are collected within one PHY frame period can be partitioned into K clusters. The cluster number K corresponds to the number of different illumination levels that can be output by the transmitter, and is determined in Algorithm 3.

Algorithm 3 Adaptive threshold

```

1: Input 1: a sequence of sample vector  $\underline{\mathbf{U}}^\dagger[n]$  collected during  $n$ -th PHY frame
2: Input 2: estimated duty cycle  $\hat{Q}$  of PWM signal  $p_1(t)$ 
3: Output:  $\gamma_{\text{HI}}[n+1]$  and  $\gamma_{\text{LO}}[n+1]$  for decoding of  $(n+1)$ -th PHY frame
4: if  $\hat{Q} = \frac{2}{z+4}$  then
5:    $K \leftarrow 3$ 
6: else if  $\hat{Q} = \frac{z+2}{z+4}$  then
7:    $K \leftarrow 3$ 
8: else
9:    $K \leftarrow 4$ 
10:  $(c_1, c_2, \dots, c_K) \leftarrow \kappa\{\underline{\mathbf{U}}^\dagger[n]\}$ 
11:  $\gamma_{\text{HI}}[n+1] \leftarrow \frac{c_K + c_{K-1}}{2}$ 
12:  $\gamma_{\text{LO}}[n+1] \leftarrow \frac{c_1 + c_2}{2}$ 
13: if  $\hat{Q} = \frac{z+2}{z+4}$  then
14:    $\Gamma[n+1] \leftarrow c_K - \gamma_{\text{HI}}[n+1]$ 
15: else
16:    $\Gamma[n+1] \leftarrow \gamma_{\text{LO}}[n+1] - c_1$ 

```

The updating rule is describe in Algorithm 3. One input to the algorithm a vector of the total ADC samples $\underline{\mathbf{U}}^\dagger[n]$ collected by receiver L2 when receiving the n -th PHY frame $F[n]$. Note that the PHY frame length corresponds to $(z+4)$ number of bit duration at the receiver side and half of them are sensing intervals. In each sensing interval, N number of ADC samples are collected. Therefore, the dimension of $\underline{\mathbf{U}}^\dagger[n]$ is 1-by- $(\frac{z+4}{2}N)$. Another input is the estimated duty cycle \hat{Q} of PWM signal $p_1(t)$, by using the decoded redundant bits position. Specifically,

$$\hat{Q} = \begin{cases} \frac{2}{z+4}, & \text{if no information bit is received for } 0 < t < QT_p, \\ \frac{z+2}{z+4}, & \text{if no information bit is received for } QT_p < t < T_p. \end{cases} \quad (5.10)$$

In cases $\hat{Q} = \frac{2}{z+4}$ and $\hat{Q} = \frac{z+2}{z+4}$, the dimming signal $y_1(t)$ are with only three different illumination levels (i.e. $K = 3$). Otherwise, we assign $K = 4$. The function $\kappa\{\cdot\}$ implements a K -means clustering algorithm [24] and outputs K centroid locations in an ascending order, i.e. $c_1 < c_2 < \dots < c_K$. The threshold γ_{HI} is assigned with the average value of the two largest centroid locations, and γ_{LO} with the average of the two smallest centroid locations. The updated threshold $\gamma_{\text{HI}}[n+1]$ and $\gamma_{\text{LO}}[n+1]$ are used for decoding of a subsequent frame $F[n+1]$.

In addition to γ_{HI} and γ_{LO} , the receiver also adapts the band gap option Γ per frame using steps 14 to 18 in Algorithm 3. Recall that Γ is used to

detect the rising / falling edges of signal $y(t)$ in the first step of decoding. As the communication distance increases, the maximum absolute value of sample difference $|d^k|$ decreases following the inverse square law. As such, Γ must be adapted to portability for correct decoding. Depending on the estimated duty cycle \hat{Q} , a receiver updates Γ with two rules.

1. In case no information bits are carried in the OFF period of PWM signal, i.e. $\hat{Q} = \frac{z+2}{z+4}$, the cluster number $K = 3$ and the cluster centroid locations satisfy $c_1 < c_2 < c_3$. The receiver applies the first rule to update Γ with the difference between c_3 and the updated threshold $\gamma_{\text{HI}}[n+1] = \frac{c_3+c_2}{2}$, i.e.

$$\Gamma[n+1] = c_3 - \frac{c_3 + c_2}{2} = \frac{c_3 - c_2}{2}. \quad (5.11)$$

2. In case at least one information bit is carried in the OFF period of PWM signal, the receiver uses the second rule to update Γ with the difference between c_1 and the updated threshold $\gamma_{\text{LO}}[n+1] = \frac{c_1+c_2}{2}$ ($c_1 < c_2$), i.e.

$$\Gamma[n+1] = \frac{c_1 + c_2}{2} - c_1 = \frac{c_2 - c_1}{2}. \quad (5.12)$$

5.5 Experimental results

In this section, we describe our prototype implementation and evaluate the system performance.

5.5.1 Prototype implementation

For the adaptive transmitter, random transmission bits are generated and encoded using 4B6B line code in a Matlab testbench. There are five codewords plus four redundant bits per PHY frame, which gives $x = 4$, $y = 6$, $W = 5$ and $z = 30$. Each frame is carried by one PWM period. We choose $T_b = 500 \mu\text{s}$ and $T_p = 17 \text{ ms}$. The achieved data rate is given by $\frac{1}{T_b} \times \frac{z}{z+4} \times \rho \approx 1176 \text{ bps}$, where $\rho = \frac{2}{3}$ is the 4B6B RLL code rate. The modulation signals $m(t)$, $p(t)$ and their weighted summation $y(t)$ are realized using the analog output channel of a NI myDAQ acquisition card. The voltage signal $y(t)$ is fed into a unit gain buffer, which increases the load current up to 40 mA. The buffer is realized using an integrated operation amplifier (op-amp) of a micro-controller unit (MCU) TI MSP430F2274. The op-amp output directly drives a single CREE XLamp CM-E color LED for illumination and optical signal transmission. There are

individually addressable red, green, blue and white color LED chips on one package, among which only the red LED chip has been used. Its switch-ON voltage $\mu = 1.8$ V and is output from the same analog channel.

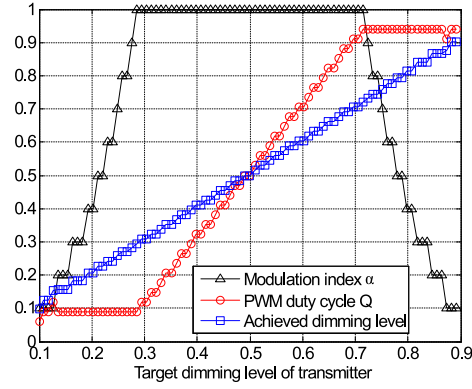
For the adaptive receiver, the sensing bit sequence is locally generated by another MCU, which further implements the RLL encoding, OOK modulation and semi-synchronization with its software. The receiving front-end is a red LED chip of the same type and is driven by the general purpose input/output ports of the MCU. The TIA is implemented with an integrated op-amp of the MCU, with a 500 k Ω feedback resistor and a 2.2 pF noise reducing capacitor. Due to the limited computational resource on the MCU, both decoder and adaptive threshold algorithm are implemented with PC software. The TIA output is communicated to the PC using an analog input channel of a data acquisition card, at a rate of $N = 100$ samples per sensing slot (one T_b). Initially, both the transmitting and receiving LEDs are placed in a dark room, facing each other via a line-of-sight path.

5.5.2 Dimming support

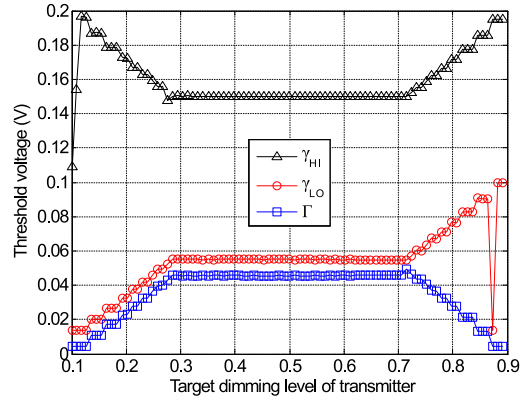
We now study the adaptive behavior of the proposed system under dynamic target dimming levels. The stimuli $\lambda^* = (0.10, 0.11, \dots, 0.89, 0.90)$ is loaded into the Matlab testbench. The communication distance is fixed at $d = 15$ cm in dark room conditions. In Fig. 5.5 (a), we show the adaptation of transmitter parameters, including the modulation index α and the PWM duty cycle Q . As λ^* increases from 0.1 to 0.5, the value of α is increased before Q . This is because for each target dimming level, the transmitter first selects the maximum possible α from Table 5.1. It then calculates Q using Eq. (5.4). As λ^* approaching 0.9, PWM duty cycle Q reaches the upper bound $\frac{z+2}{z+4}$. As such, the transmitter decreases α to trade SNR for higher illumination level. The difference between achieved dimming level and λ^* is caused by rounding error of Q and is below 3% for $0.1 \leq \lambda^* \leq 0.9$.

In Fig. 5.5 (b), we show the adaptation of decoder threshold to modulation index changes. The value of γ_{HI} is inversely proportional to α . This is because the centroid position c_{k-1} is inversely proportional to α , and so is $\gamma_{\text{HI}} = \frac{c_K + c_{K-1}}{2}$. The value of γ_{LO} is proportional to α for $0.1 < \lambda^* < 0.7$. This is because the centroid position c_2 increases over α , and so is $\gamma_{\text{LO}} = \frac{c_1 + c_2}{2}$. The value of γ_{LO} is inversely proportional to α as λ^* approaching 0.9. This is because Q has reached its upperbound, which gives a cluster number $K = 3$ (step 6. in Algorithm 3). The value $\gamma_{\text{LO}} = \frac{c_1 + c_2}{2} = \frac{c_1 + c_{K-1}}{2}$ is inversely proportional to α . The relation between Γ and α can be explained in a similar way. There is a spike at the beginning of γ_{HI} , where $QT_p = 2T_b$. According to step 12 in Algorithm 3, the

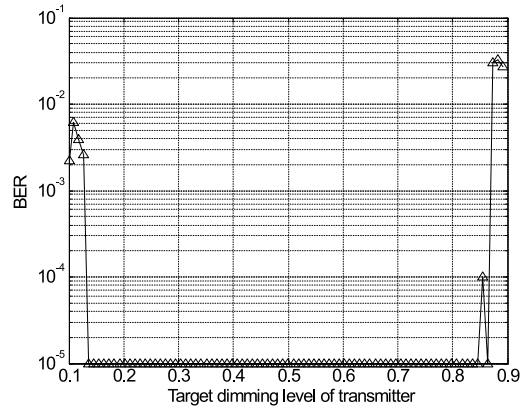
CHAPTER 5. ADAPTIVE VISIBLE LIGHT COMMUNICATION AND ILLUMINATION WITH LEDS



(a) Adaptation of modulation index and PWM duty cycle to dimming level.

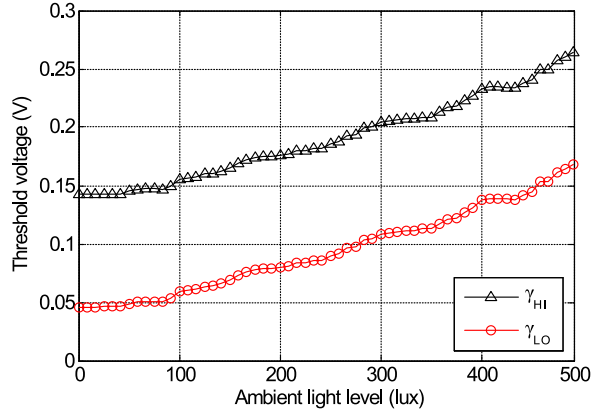


(b) Adaptation of decoder threshold to dimming level.

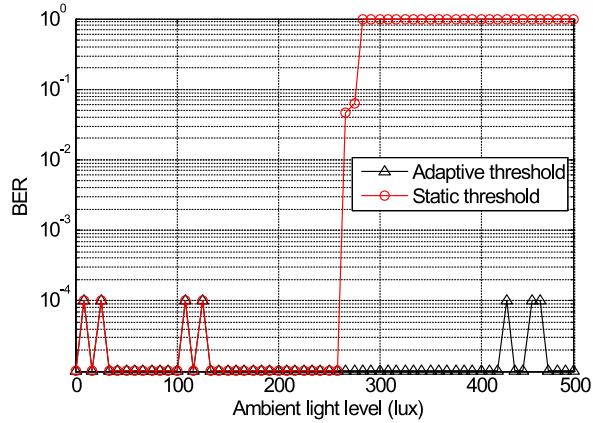


(c) BER vs dimming level.

Figure 5.5: Adaptation of the system to dimming level changes of the transmitter.



(a) Adaptation of threshold voltage to ambient light level changes.



(b) Robustness of adaptive receiver against ambient light level changes.

Figure 5.6: Adaptation of the system to ambient light level changes.

cluster number $K = 3$ and γ_{HI} is lowered by the centroid position of the middle cluster, c_2 . There is another spike near the end of γ_{LO} , where $\lambda^* = 0.87$. From Table 5.1, it gives $\alpha = 0.1$. From Eq. (5.4), it gives $Q = \frac{31}{34}$. According to step 13 in Algorithm 3, the cluster number $K = 4$ and γ_{LO} is lowered by the centroid position c_2 .

The BER plot is shown in Fig. 5.5 (c), which is calculated per 10^4 transmitted information bits. Zero bit error is replaced by 10^{-5} in order to show in the log scale plot. For values $\alpha \geq 0.2$, the system achieves unidirectional communication with $BER < 10^{-3}$. BER goes beyond 10^{-3} only when $\alpha = 0.1$, due to limited SNR for the selected communication distance of $d = 15$ cm.

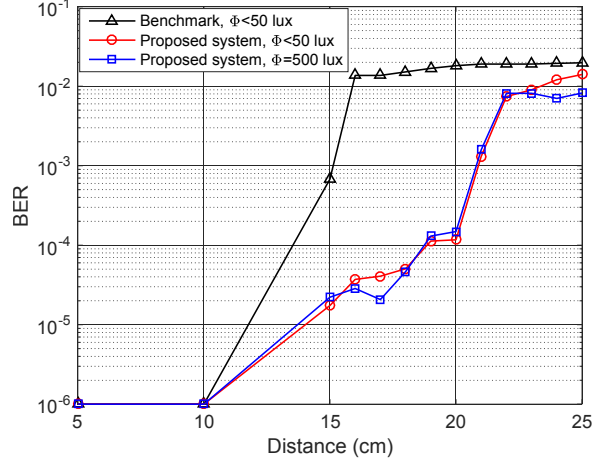


Figure 5.7: Plot of BER over communication distance.

5.5.3 Communication performance

We now study adaptation of the receiver to ambient light changes. We fix $\lambda^* = 0.5$ (which gives $\alpha = 1$) and the communication distance $d = 15$ cm. The ambient light is increased gradually from 0 lux till 500 lux. The plot of adaptive threshold over time is shown in Fig. 5.6 (a). We select the system presented in [20] as a benchmark, which implements a static threshold decoder at the receiver and features $\alpha = 1$ at the transmitter. Their communication performance is compared by showing the BER plot in Fig. 5.6 (b). Denote the ambient light level with Φ , the benchmark system fails to decode at $\Phi \approx 260$ lux, followed by a loss of semi-synchronization at $\Phi \approx 280$ lux. From then on, the decoded bit sequence is longer than the transmitted one due to the failure of removing the redundant bits. In this case, the BER value is assigned with 1. In comparison, the proposed system shows robustness against ambient light changes in a range between 0 and 500 lux.

The same benchmark is used to highlight the robustness of the proposed system against dynamic communication distance (portability), which is shown in Fig. 5.7. For the proposed system, we set $\lambda = 0.53$ ($\alpha = 1$). The communication distance is changed from 5 cm to 15 cm in steps of 5 cm, and in steps of 1 cm till a distance of 25 cm. At each position, BER is calculated per 10^5 transmitted information bits under two configurations of ambient light level: $\Phi < 50$ lux (dark room condition) and $\Phi = 500$ lux. Compared with the benchmark, the proposed system extends the communication distance (with $\text{BER} < 10^{-3}$) from 15 cm to 20 cm, which is about 33% improvement regardless of ambient light

changes. At distances greater than $d = 20$ cm, communication deteriorates because of small SNR. Considering the communication range scaling analysis in [20], assuming RGB (red, green, blue) LED strips with 5 tri-color RGB LED chips in series and 24 such branches in parallel are used as transmitter and receiver, the communication range increase of 5 cm is scaled to 2 m.

5.6 Conclusions and discussions

We presented the design of a LED based VLC system where the LED is used for adaptive VLC transmission and reception, as well as for illumination. In the proposed design, the modulation index at the transmitter as well as calibration detection thresholds at the receiver are adapted to react to changes in ambient illumination conditions and limited LED device portability. Using an experimental prototype system, we showed that an increase of almost 33% in reliable communication distance can be obtained in comparison to a non-adaptive VLC system.

Under the choice of a single, low-power LED as transceiver, the reliable VLC range was demonstrated to be 20 cm. If a RGB LED strip with 5 tri-color RGB LED chips in series and 24 such branches in parallel were to be used as transceiver, we expect the effective communication range to scale to about 8 m [20] and thus suitable for low to medium rate indoor applications.

The proposed adaptive threshold scheme in Algorithm 1 can also be used in two-way VLC system [10], [11], with appropriate parameter modifications. Performance analysis of an adaptive two-way VLC system is a topic of future study.

REFERENCES

- [1] T. Komine and M. Nakagawa, “Fundamental analysis for visible-light communication system using LED lights,” *IEEE Transactions on Consumer Electronics*, vol. 50, no. 1, pp. 100–107, February 2004.
- [2] K. Warmerdam, A. Pandharipande, and M. Zuniga, “Visible light communications for sensing and lighting control,” *IEEE Sensors Journal*, vol. 16, no. 17, pp. 6718–6726, September 2016.
- [3] S. Rajagopal, R. D. Roberts, and S. K. Lim, “IEEE 802.15.7 visible light communication: modulation schemes and dimming support,” *IEEE Communications Magazine*, vol. 50, no. 3, pp. 72–82, March 2012.
- [4] G. Corbellini, K. Aksit, S. Schmid, S. Mangold, and T. R. Gross, “Connecting networks of toys and smartphones with visible light communication,” *IEEE Communications Magazine*, vol. 52, no. 7, pp. 72–78, July 2014.
- [5] 802.15.7 IEEE standard for local and metropolitan area networks, *part 15.7: Short Range Wireless Optical Communication Using Visible Light*, 2011.
- [6] D. Giustiniano, N. O. Tippenhauer, and S. Mangold, “Low-complexity visible light networking with LED-to-LED communication,” *IFIP Wireless Days*, pp. 1–8, November 2012.
- [7] S. Schmid, G. Corbellini, S. Mangold, and T. R. Gross, “An LED-to-LED visible light communication system with software-based synchronization,” *IEEE Globecom Workshops*, pp. 1264–1268, December 2012.
- [8] Schmid, Stefan, G. Corbellini, S. Mangold, and T. R. Gross, “LED-to-LED visible light communication networks,” *Proceedings of the Fourteenth ACM International Symposium on Mobile Ad Hoc Networking and Computing*, pp. 1–10, 2013.
- [9] S. Schmid, G. Corbellini, S. Mangold, and T. R. Gross, “Continuous synchronization for LED-to-LED visible light communication networks,” *3rd International Workshop in Optical Wireless Communications*, pp. 45–49, September 2014.
- [10] S. Li, A. Pandharipande, and F. M. J. Willems, “Redundant run-length limited encoding for two-way visible light communication,” *Annual Conference of the IEEE Industrial Electronics Society*, pp. 4706–4712, October 2016.

-
- [11] S. Li, A. Pandharipande, and F. M. J. Willems, “Two-way visible light communication and illumination with LEDs,” *IEEE Transactions on Communications*, vol. 65, no. 2, pp. 740–750, February 2017.
- [12] Y. Wang, L. Tao, X. Huang, J. Shi, and N. Chi, “8-Gb/s RGBY LED-based WDM VLC system employing high-order CAP modulation and hybrid post equalizer,” *IEEE Photonics Journal*, vol. 7, no. 6, pp. 1–7, December 2015.
- [13] R. X. G. Ferreira, E. Xie, J. J. D. McKendry, S. Rajbhandari, H. Chun, G. Faulkner, S. Watson, A. E. Kelly, E. Gu, R. V. Penty, I. H. White, D. C. O’Brien, and M. D. Dawson, “High bandwidth GaN-based micro-LEDs for multi-Gb/s visible light communications,” *IEEE Photonics Technology Letters*, vol. 28, no. 19, pp. 2023–2026, October 2016.
- [14] L. Grobe, A. Paraskevopoulos, J. Hilt, D. Schulz, F. Lassak, F. Hartlieb, C. Kottke, V. Jungnickel, and K. D. Langer, “High-speed visible light communication systems,” *IEEE Communications Magazine*, vol. 51, no. 12, pp. 60–66, December 2013.
- [15] D. Karunatilaka, F. Zafar, V. Kalavally, and R. Parthiban, “LED based indoor visible light communications: State of the art,” *IEEE Communications Surveys Tutorials*, vol. 17, no. 3, pp. 1649–1678, thirdquarter 2015.
- [16] F. M. Mims, *Siliconconnections: Coming of Age in the Electronic Era*. New York, NY, USA: McGraw-Hill, 1986.
- [17] P. Dietz, W. Yerazunis, and D. Leigh, “Very low-cost sensing and communication using bidirectional LEDs,” *5th International Conference on Ubiquitous Computing*, pp. 175–191, 2003.
- [18] S. Li and A. Pandharipande, “LED-based color sensing and control,” *IEEE Sensors Journal*, vol. 15, no. 11, pp. 6116–6124, November 2015.
- [19] S. Li, A. Pandharipande, and F. M. J. Willems, “Daylight sensing LED lighting system,” *IEEE Sensors Journal*, vol. 16, no. 9, pp. 3216–3223, May 2016.
- [20] S. Li, A. Pandharipande, and F. M. J. Willems, “Unidirectional visible light communication and illumination with LEDs,” *IEEE Sensors Journal*, vol. 16, no. 23, pp. 8617–8626, December 2016.
- [21] Q. Wang, D. Giustiniano, and D. Puccinelli, “An open-source research platform for embedded visible light networking,” *IEEE Wireless Communications*, vol. 22, no. 2, pp. 94–100, 2015.

CHAPTER 5. ADAPTIVE VISIBLE LIGHT COMMUNICATION AND
ILLUMINATION WITH LEDS

- [22] Q. Wang and D. Giustiniano, “Intra-frame bidirectional transmission in networks of visible LEDs,” *IEEE/ACM Transactions on Networking*, vol. 24, no. 6, pp. 3607–3619, December 2016.
- [23] E. Schubert, *Light-Emitting Diodes*. Cambridge University Press, 2006.
- [24] T. Hastie, R. Tibshirani, and J. Friedman, *The Elements of Statistical Learning*. New York, NY, USA: Springer-Verlag, 2009.

Chapter 6

Two-way visible light communication and illumination with LEDs*

Visible light communications (VLC) with light emitting diodes (LEDs) has attracted applications like data communications, lighting control and light interaction. In this paper, we propose a system by which two LED devices are used for two-way VLC while also providing illumination. We consider Manchester encoding with on-off keying for transmission. A reception scheme in which the LEDs themselves are used as receivers by sensing in the off periods is considered. A synchronization scheme to achieve frame- and symbol-level synchronization is also proposed. A prototype of the proposed system is designed and the communication performance is evaluated.

*This chapter has been published as: S. Li, A. Pandharipande and F. M. J. Willems, "Two-way visible light communication and illumination with LEDs", *IEEE Transactions on Communications*, vol. 65, no. 2, pp. 740-750, February 2017.

6.1 Introduction

Visible light communication (VLC) refers to communication in the visible part of the spectrum. This involves a VLC transmitter that transmits information by modulating its light output and a receiver that is capable of decoding the transmitted information. Embedding information by modulating light output has become easier with the advent of light emitting diodes (LEDs). A number of applications in lighting control, light interaction and infotainment networking [1], [2], [3], [4] make use of VLC with LEDs. In addition to being used as transmitters, LEDs have been recently used as light sensors in different applications [5], [6], [7]. However limited work exists on the use of LEDs as receivers, with the notable exception of the body of works [8], [9], [10], [11], [12], [13]. In this paper, we consider the use of LEDs as transceivers to achieve two-way communication, while providing basic illumination.

In the proposed system, we use LEDs as both transmitters and receivers in two-way VLC, without using additional dedicated light sensors as receivers. Two-way VLC refers to two devices transmitting simultaneously using VLC. In our system, two LED devices transmit information to each other, while additionally serving as sensors to receive this information and providing illumination. The design of this new system brings about a number of technical challenges:

- [i] how should data encoding/decoding be designed to enable LEDs to transmit/receive for a two-way VLC, while also providing illumination without perceivable flicker;
- [ii] how should the LED devices be synchronized for two-way VLC;
- [iii] what are the communication and illumination trade-offs in such a system.

6.1.1 Related work

A number of works have considered VLC systems with LEDs and *dedicated* light sensors as VLC receivers [1], [14], [15], [16], [17], [18], [19], [20], [21], [22], [23]. In [1], the performance of a LED lighting system that provides illumination and VLC with photodetectors was analyzed. The possibility of achieving high data rates with VLC were shown in [14], [16], [21], [22], [23]. A hybrid communication protocol for mixing camera communication with faster modulation designed for photodetectors was considered in [17]. In [18], a platform for distributed, multi-hop VLC was presented. Full-duplex VLC relaying across luminaires in an indoor lighting system was proposed in [19], [20], with advanced signal processing techniques for dealing with self-interference at the photodetector at the relay luminaire. For a recent overview on VLC, see [15].

The use of LEDs as receivers has been explored in [8], [9], [10], [11], [12] to achieve VLC for LED-to-LED communications in consumer toys and entertainment applications. Due to the nature of these applications, limited attention was given to illumination constraints. Simple PHY and MAC layer protocols to enable slotted communications with LED devices were considered in these works. Schemes were proposed to leave devices unsynchronized and transmit a dedicated synchronization preamble [8, 9] or idle patterns [24] before each frame. An improvement was proposed in [10] by considering a physical layer protocol based on a slotting structure. The scheme used 2-pulse position modulation which supports one-way transmission over an unoccupied channel (with the receiving device in sensing mode). It utilized two dedicated synchronization intervals to determine the direction of phase offset between two devices. A stepwise correction was implemented by iteratively changing the subsequent LED ON slot duration. An open source embedded Linux platform with a LED transceiver front-end, OpenVLC, was presented in [11] and [12]. A carrier sensing multiple access/collision detection and hidden avoidance MAC protocol was presented in [12], by which in-band bi-directional transmission was realized in a visible light network of LEDs. This system results in asymmetric data rate, with the achieved data rate in one direction being half of the data rate in the other direction. Also, the illumination level of the receiver depends on its payload and is less than 50%. In [13], we have proposed a LED system for jointly achieving unidirectional VLC while providing flicker-free illumination. The receiving LED is OOK modulated for VLC reception in the OFF periods. It is allowed to be asynchronous to the transmitter, with a phase offset within a preset range.

6.1.2 Contributions and organization of our work

We propose a two-way VLC system that can support simultaneous communication between two LED devices, without the use of dedicated photodetectors, and also provide illumination. The two-way channel was first introduced by Shannon [25] and the achievable rate was analyzed in an information-theoretic setting. Since then, the two-way channel has been studied in different wireless communication systems [26], [27]. The performance of two-way VLC systems has not yet been studied in the literature yet, to the best of our knowledge. Section 6.2 provides an overview of the proposed VLC system. The VLC system rate and illumination are considered and the combination of Manchester coding plus on-off-keying (OOK) modulation is shown to achieve the optimum rate-illumination trade-off. The designed LED transceiver prototype is described

in Section 6.3². The physical layer data frame structure, encoding and decoding schemes are presented in Section 6.4. Our proposed symbol-level synchronization scheme omits dedicated synchronization intervals and reuses the symbol slot for phase offset correction. This is in contrast to past works in VLC that used dedicated synchronization preambles [8, 9] or idle patterns [24]. Both the direction and the amount of phase offset are derived in this way, allowing fast synchronization within one symbol slot. Furthermore, a scheme to compensate for any illumination loss due to phase correction during the synchronization process is proposed. The synchronization and illumination loss compensation schemes are explained in Section 6.5. Experimental results to evaluate the illumination and communication performance of the designed two-way VLC system are presented in Section 6.6. The trade-off between VLC system rate and illumination is analyzed in Appendix 6.A by establishing a connection to the two-way channel. Conclusions are drawn in Section 6.7.

6.2 System structure

The structure of a two-way VLC system with two LED devices is illustrated in Fig. 6.1. It consists of a dual-mode driver and a LED based transceiver communicating over the optical free space medium. The signaling waveform of a LED device is designed such that the transceiver can receive optical signals during the OFF period of the waveform. The LED driver operates in two modes. In the emitting mode of the driver circuit, the LED device is forward-biased to output a constant light level. In the sensing mode, the LED device is switched off to convert the received light power to a photocurrent signal.

Consider a time slotted structure. During each time slot, the LED device is either in the emit or sense state. Only when in the sense state can a LED device decide whether the other one has emitted light or not. Communication and illumination can be expressed by the system response given in Table 6.1. In this table, the first two columns list the four possible states of the two LED devices. For each device, depending on its state, the corresponding transceiver outputs three types of measurements: ‘light’, ‘no light’ and ‘unknown’. Consider the first row. Both transceivers have output ‘no light’ since these devices are in sense state and there is no transmission. Now consider the second row as an example. Transceiver 1 outputs ‘light’ in response to the emit state of LED device 2, and LED device 1 being in sense state. On the other hand, transceiver 2 outputs ‘unknown’ because LED device 2 is in emit state and hence cannot

²A prototype design for such a LED transceiver has been presented in [28] with redundant run-length limited coding schemes being considered.

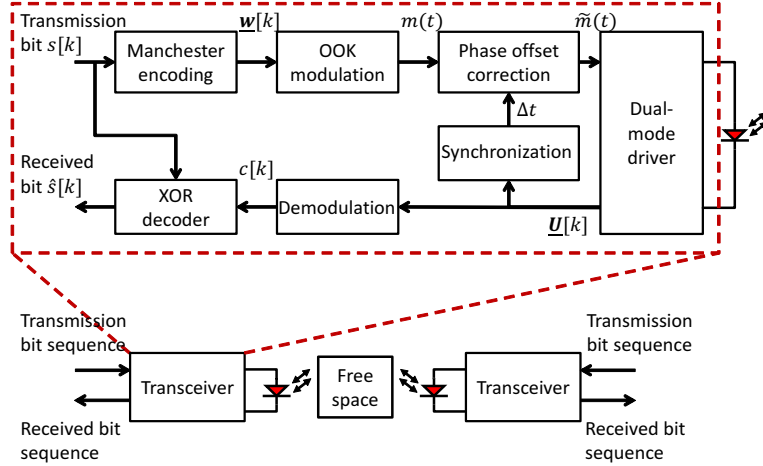


Figure 6.1: System structure and transceiver block diagram.

Table 6.1: System truth table, describing channel outputs given the inputs, for each time slot.

LED device 1	LED device 2	Transceiver 1 measurement	Transceiver 2 measurement
sense	sense	no light	no light
sense	emit	light	unknown
emit	sense	unknown	light
emit	emit	unknown	unknown

decide the state of the other device.

Given this system response, we consider the design of data encoding to enable LEDs to transmit/receive for two-way VLC. We begin by considering the trade-off between the system rate and illumination in such a system. The first contribution of this paper is to establish that the combination of the Manchester coding and OOK modulation achieves optimum system performance in the sense of balancing the rate-illumination trade-off. This encoding scheme achieves a rate-illumination quadruple (0.5, 0.5, 50%, 50%). Rates are equal to 0.5 bit per channel use (time slot) and illumination levels of 50% can be realized, which is optimal. The reader is referred to the Appendix for a detailed analysis and proof.

Consider one of the LED transceiver blocks in Fig. 6.1. The k -th transmission bit $s[k]$ is Manchester encoded into a binary codeword $\underline{w}[k] = (w_1[k], w_2[k])$. We apply OOK modulation to represent the digital codeword with a square wave $m(t)$. During the ON period of the square wave, the LED is forward-biased

to output a constant light level. During the OFF period of the square wave, the LED turns off and outputs photocurrent in response to the incident light power. Switching between the light emitting and sensing modes is realized by the dual-mode driver. The driver converts the photocurrent to a voltage signal and outputs a vector of samples $\underline{U}[k]$. The demodulation and decoding steps require tight synchronization between the transmissions of the two devices. As such, samples are first used in a synchronization scheme to estimate the phase offset Δt between the two LED transceivers. If the two transceivers are determined to be asynchronous, we reshape the square wave $m(t)$ to compensate for the phase error. The resulting square wave is denoted by $\tilde{m}(t)$. Upon synchronization, we extract a binary bit $c[k]$ from $\underline{U}[k]$ by a demodulation scheme. The decoder then performs an exclusive-OR (XOR) operation between $c[k]$ and the transmission bit $s[k]$ to obtain the received bit $\hat{s}[k]$. These schemes will be discussed in detail in the following sections.

6.3 LED transceiver front-end

The LED transceiver front-end is a dual-mode driver circuit that connects the LED devices with the digital baseband modules. Fig. 6.2 illustrates the block diagram of the LED transceiver with front-end details. The transmitting part consists of a Manchester encoder, an OOK modulator and two configurable general-purpose input/output (GPIO) ports. A transmission bit $s[k]$ is encoded and modulated into a square wave $m(t)$. It configures two GPIO ports to switch the LED device between two modes. In the ON period of $m(t)$, the LED device is in emitting mode. In the OFF period of $m(t)$, the sensing mode is activated and the LED device is zero-biased to receive light. A photocurrent $I_{ph}(t)$ is excited and measured by the receiving part of the dual-mode driver.

The receiving part consists of a trans-impedance amplifier (TIA) and an analog-to-digital converter (ADC). The TIA converts the photocurrent to a continuous voltage signal $U_{ph}(t)$ that is quantized using the ADC. The resulting samples $\underline{U}[k] = (U_1[k], \dots, U_{N_s}[k])$ consists of N_s number of 10-bit ADC words and are used for demodulation and decoding. The light sensing and voltage conversion are detailed in Fig. 6.3.

In Fig. 6.3a, we show the current-voltage characteristics of a light sensing LED that operates in short circuit mode. The corresponding load line is highlighted with a red arrow and indicates a zero load resistance. Therefore, we directly measure the photocurrent I_{ph} which is linearly related to the incident light intensity E by the LED responsivity R_λ . The photocurrent equals zero in a dark environment with $E = 0$. As such, the I_{ph} measurements are purely at-

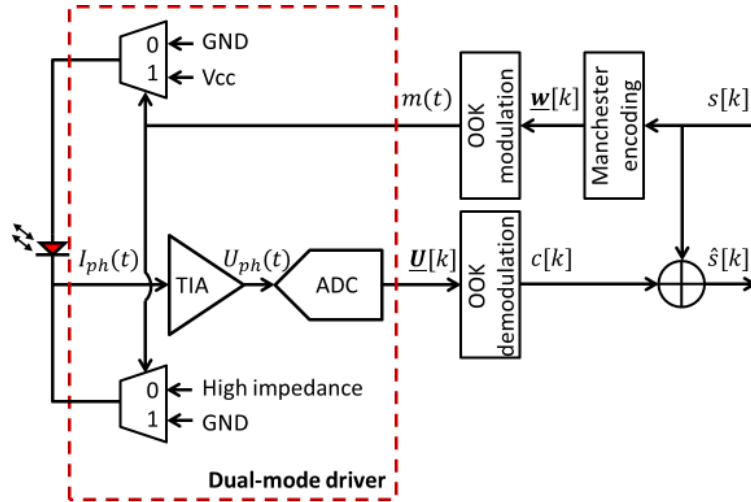


Figure 6.2: Block diagram of LED transceiver front-end.

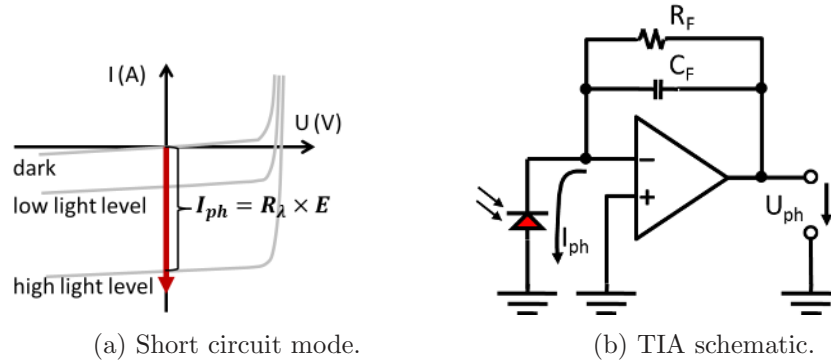


Figure 6.3: Photocurrent to voltage converter using TIA with a light sensing LED operating at short circuit mode.

tributed to the power of the incident optical signal. This is an advantage over the photoconductive mode. Measurements of photocurrent I_{ph} are typically implemented with current-to-voltage converters (i.e. a TIA). It makes the temperature dependence of the output voltage signal much lower and is linearly proportional to a wide range of incident light intensity [29]. photovoltaic mode.

The schematic of a TIA converter is shown in Fig. 6.3b. A feedback resistor R_F is connected between the inverting input of an operational amplifier (op-amp) and its output. This feedback resistor provides gain across the op-amp.

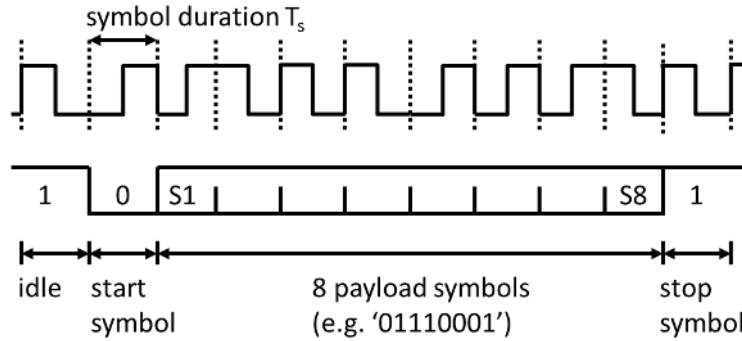


Figure 6.4: Data frame structure.

For indoor situations where low light levels are possible, a large R_F value is chosen so as to convert a weak photocurrent I_{ph} to a voltage signal within the sensing range of the ADC. The output voltage is then $U_{ph} = I_{ph} \times R_F$. Despite a high op-amp gain, a large feedback resistor results in a noisy output signal. To compensate, the feedback resistor connects to a noise reducing capacitor C_F in parallel. The capacitance balances the trade-off between stability and bandwidth of the TIA converter [30].

6.4 Data transmission

In this section, we introduce the physical layer frame structure and the coding scheme, followed by the decoding scheme.

6.4.1 PHY frame structure and coding scheme

We structure a frame with one start symbol S , a number of payload symbols and one stop symbol \bar{S} that is the bit-wise complement of S . Fig. 6.4 illustrates an exemplary frame structure similar to universal asynchronous receiver/transmitter (UART) formatting. It consists of one start symbol $S = '0'$ and eight binary payload symbols $s[1], \dots, s[8]$ followed by one stop symbol $\bar{S} = '1'$. The start symbol indicates the beginning of a frame and informs the receiver of eight incoming payload symbols. The stop symbol is the last symbol of a frame and is followed by another frame or idle symbols. An idle symbol is a symbol \bar{S} ($\bar{S} = '1'$ in considered example) that is filled in between two frames and indicates an idle state. The symbols are Manchester coded and OOK modulated. Therefore, the LED based device is switched off for light sensing during half-time of each symbol

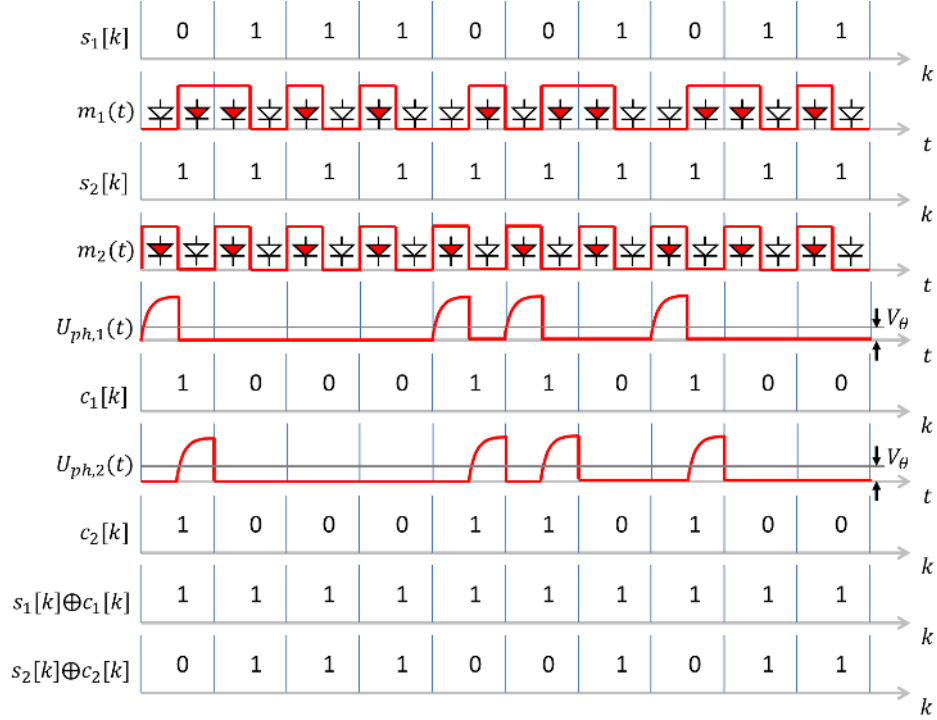


Figure 6.5: Optical signaling waveforms of two symbol-level synchronized transceivers for proposed coding scheme.

duration T_s .discussed below.

6.4.2 Decoding scheme

Fig. 6.5 shows exemplary signaling waveforms depicting the proposed encoding and decoding scheme. We consider a LED transceiver L1 that is synchronized to another transceiver L2 and transmits a data sequence $\underline{s}_1 = (s_1[1], \dots, s_1[10])$. The modulated optical signal $m_1(t)$ is shown over a duration of $10T_s$ in this example. Device L2 stays in idle state and transmits idle symbols as shown by the modulated optical signal $m_2(t)$. In the sensing period of the k -th symbol duration ($k = 1, 2, \dots, 10$), a LED transceiver measures an illumination value

$$l[k] \in \{l_n[k], l_n[k] + \Phi(d)\}, \quad (6.1)$$

where $l_n[k]$ denotes the illumination level that captures the background noise when L1 and L2 are switched off, and $\Phi(d)$ is the illuminance value measured at a certain distance d when a LED transceiver is fully ON.

CHAPTER 6. TWO-WAY VISIBLE LIGHT COMMUNICATION AND ILLUMINATION WITH LEDS

Signals $U_{ph,1}(t)$ and $U_{ph,2}(t)$ are photovoltage signals measured by L1 and L2 at the TIA converter output. The photovoltage signal $U_{ph}(t)$ is linearly related to the received illumination value $l[k]$ by

$$U_{ph}(t) = R_\lambda \times l[k] \times R_F, \quad (6.2)$$

where R_λ is the LED responsivity and R_F is the feedback resistor of the TIA converter. In total N_s voltage samples are collected in each T_s duration. The average value of sample vector $\underline{U}[k] = (U_1[k], \dots, U_{N_s}[k])$ is compared to a threshold voltage V_θ to derive a binary data $c[k]$ as

$$c[k] = \begin{cases} 0 & , \text{if } \frac{1}{N_s} \sum_{j=1}^{N_s} U_j[k] < V_\theta, \\ 1 & , \text{otherwise.} \end{cases} \quad (6.3)$$

We explain the decoding process by considering two scenarios. When L1 and L2 transmit identical symbols (i.e. $s_1[k] = s_2[k] = 0$ or $s_1[k] = s_2[k] = 1$), we can write $s_1[k] = s_2[k] \oplus 0$ with ‘ \oplus ’ being an XOR operator. We thus obtain $c_1[k] = c_2[k] = 0$ using (2). When L1 and L2 transmit different symbols (i.e. $s_1[k] = 0, s_2[k] = 1$ or $s_1[k] = 1, s_2[k] = 0$). This gives $c_1[k] = c_2[k] = 1$. Combining the two cases gives

$$\hat{s}_1[k] = s_2[k] \oplus c_2[k]. \quad (6.4)$$

Similarly, $\hat{s}_2[k]$ is given by

$$\hat{s}_2[k] = s_1[k] \oplus c_1[k]. \quad (6.5)$$

Therefore, the decoder uses knowledge of its transmitted data sequence for retrieving the transmitted bits of the other LED device.

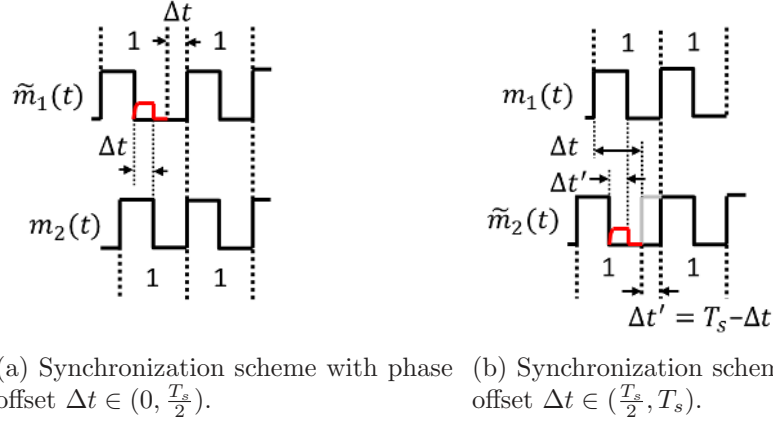
More specifically, it performs an XOR operation between the demodulated binary data sequence \underline{c} and the transmission data sequence \underline{s} . The output is an estimated binary data sequence $\hat{\underline{s}}$. In Fig. 6.5, L1 and L2 estimate

$$\begin{aligned} \hat{\underline{s}}_2 &= \underline{s}_1 \oplus \underline{c}_1 = 0B1111111111, \\ \hat{\underline{s}}_1 &= \underline{s}_2 \oplus \underline{c}_2 = 0B0111001011, \end{aligned} \quad (6.6)$$

which are respectively the transmitted data sequences.

6.5 Synchronization scheme

In the coding scheme described in Section 6.4, two synchronized LED transceivers were assumed. In this section, we propose a symbol-level synchronization scheme which reuses the idle symbol and stop symbol for synchronization. Further, we propose a frame-level synchronization scheme which allows run-time synchronization during two-way VLC.



(a) Synchronization scheme with phase offset $\Delta t \in (0, \frac{T_s}{2})$. (b) Synchronization scheme with phase offset $\Delta t \in (\frac{T_s}{2}, T_s)$.

Figure 6.6: Symbol-level synchronization scheme.

6.5.1 Symbol-level synchronization

Fig. 6.6 illustrates the proposed symbol-level synchronization scheme. Two LED transceivers transmit symbol '1' as shown by the modulated waveforms $\tilde{m}_1(t)$ and $m_2(t)$. Such a symbol is either an idle symbol or a stop symbol. In each symbol duration T_s , there is a falling edge following Manchester coding. Within $(\frac{T_s}{2}, T_s)$, both LED transceivers are switched off to sense with measurements highlighted in red color. Denote the phase offset by Δt . We implement phase compensation by considering two cases.

The first case is shown in Fig. 6.6a with $0 < \Delta t < \frac{T_s}{2}$. The signal $\tilde{m}_1(t)$ is phase-leading and has to compensate with a Δt delay before the next symbol. We derive Δt from the highlighted pulse width as

$$\Delta t = t_0 + \frac{N_p}{f_s}, \quad (6.7)$$

where t_0 , N_p and f_s are respectively the ADC setup time, the number of samples that are above the threshold V_θ and the ADC sampling frequency.

The second case is shown in Fig. 6.6b, where $\frac{T_s}{2} < \Delta t < T_s$. To compensate, a Δt delay should be inserted before the next symbol of signal $m_1(t)$. Alternatively, we consider the signal $\tilde{m}_2(t)$ being phase-leading the signal $m_1(t)$ by $\Delta t' = T_s - \Delta t$ ($0 < \Delta t' < \frac{T_s}{2}$). To compensate, we simply delay the signal $\tilde{m}_2(t)$ by $\Delta t'$ which can be derived from the highlighted pulse width in the sensing period of signal \tilde{m}_2 using (6.7). In conclusion, phase correction is limited within $(0, \frac{T_s}{2})$, which prevents transceivers from correcting phase offset simultaneously.

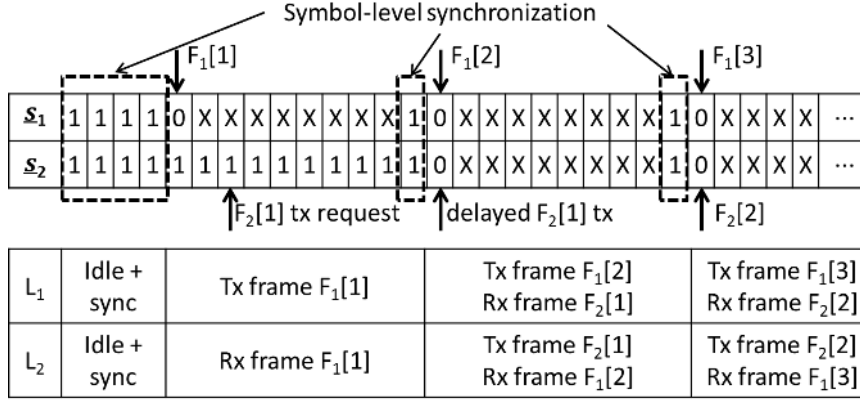


Figure 6.7: Frame-level synchronization scheme.

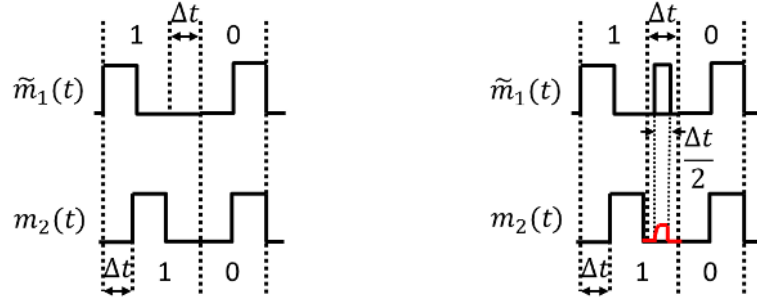
6.5.2 Frame-level synchronization

The symbol-level synchronization scheme not only aligns transceivers at the beginning of communication, but is also run-time active to compensate for clock drift. We propose a frame-level synchronization scheme that aligns the transmitted frame with received frame and executes symbol-level synchronization with the stop symbol of both frames.

Fig. 6.7 illustrates the frame-level synchronization scheme. Consider two LED transceivers L_1 and L_2 . The transmitted data sequence before Manchester coding is given in the upper table, wherein the symbol X denotes a payload bit. Initially, both L_1 and L_2 are at the idle state and execute symbol-level synchronization. Subsequently, L_1 requests to transmit a data frame $F_1[1]$. Since L_2 is idle, frame $F_1[1]$ is transmitted immediately. During $F_1[1]$ transmission, L_2 requests to transmit another frame $F_2[1]$ but delays this transmission until receiving the stop symbol of frame $F_1[1]$. L_1 and L_2 first execute symbol-level synchronization, they then transmit frames $F_1[2]$ and $F_2[1]$ simultaneously. Two-way communication is achieved and a symbol-level synchronization is executed at the stop symbol of each frame.

6.5.3 Illumination loss and compensation

Symbol-level synchronization scheme inserts delay intervals Δt between a certain number of T_s slots. This leads to an illumination loss which is proportional to the amount of phase offset between two LED transceivers L_1 and L_2 . Within



(a) Illumination loss caused by symbol-level synchronization. (b) The proposed waveform for illumination compensation.

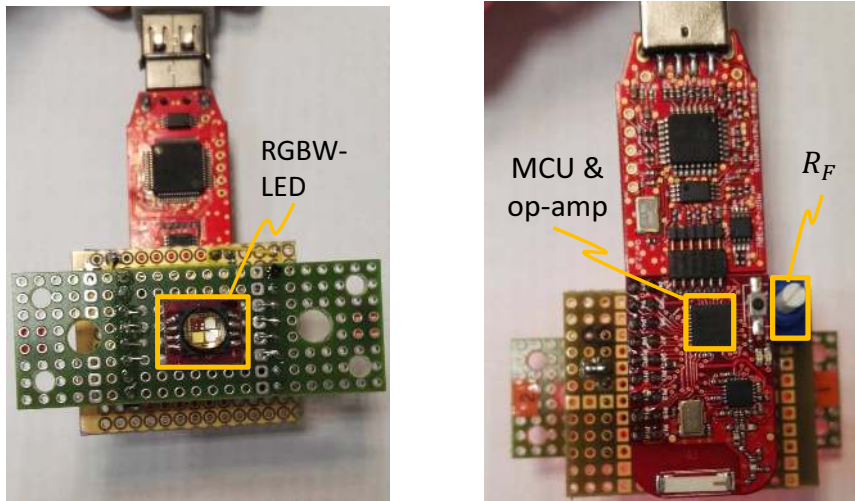
Figure 6.8: Illumination loss and compensation.

one frame, the illumination loss $\eta = \frac{f(\Delta t)}{10 \times T_s} \times 100\% < 5\%$, where

$$f(\Delta t) = \begin{cases} T_s - \Delta t & , \text{if } \Delta t \in (\frac{T_s}{2}, T_s), \\ \Delta t & , \text{if } \Delta t \in (0, \frac{T_s}{2}). \end{cases} \quad (6.8)$$

Fig. 6.8a illustrates a worst case scenario wherein a synchronization symbol '1' is followed by a start symbol '0'. We consider a phase offset Δt that is close to $\frac{T_s}{2}$. Following symbol-level synchronization, L1 delays the start symbol by Δt . This delay interval, together with the previous $\frac{T_s}{2}$ sensing period and the subsequent $\frac{T_s}{2}$ sensing period, forms a long off interval close to $\frac{3}{2}T_s$. The decrease in brightness may cause perceivable flicker. To compensate for the illumination loss and prevent flicker, we propose an illumination compensation scheme. The idea is to replace the Δt delay interval by a square waveform with 50% duty cycle. As such, the average light output within the Δt interval achieves 50% and is same as the illumination level in a complete T_s duration.

Fig. 6.8b illustrates an exemplary waveform for illumination compensation. During the first $\frac{\Delta t}{4}$ interval, the LED transceiver L1 stays off. In the subsequent $\frac{\Delta t}{2}$ interval at center, L1 is switched on to emit light. At the last $\frac{\Delta t}{4}$ interval, L1 is switched off. We design such a waveform for two reasons. First, it delivers a 50% light output for illumination compensation. Second, in response to the waveform, L2 measurements shape a narrow pulse as highlighted with red color. It acts as an identifier since it does not match any of the cases illustrated in Fig. 6.6. Thus, L2 regards it as an illumination compensation behavior of L1 and will not enter the symbol-level synchronization itself.



(a) Side A with a commercial RGBW color LED as transceiver front-end. (b) Side B with MCU, integrated TIA and communication interface.

Figure 6.9: Designed prototypes.

6.6 Experimental results

In this section, we describe the prototype implementation and evaluate the system performance with respect to coding, synchronization, communication rate and illumination level.

6.6.1 Prototype implementation

Two sides of the designed LED prototype device are shown in Fig. 6.9. Side A consists of a single CREE XLamp MC-E color LED with individually addressable red, green, blue and white (RGBW) color LED chips in one package. To illustrate the concepts presented in this paper, we only use the red LED chip and drive it with a constant current of 60 mA. This forward current is provided by two GPIO ports of a micro-controller unit (MCU) MSP430F2274 on side B. The MCU integrates an op-amp which converts the photocurrent to a voltage signal. It is then sampled by a 10-bit ADC on MCU and input to the decoder. Both the decoding and the synchronization schemes are implemented in MCU software.

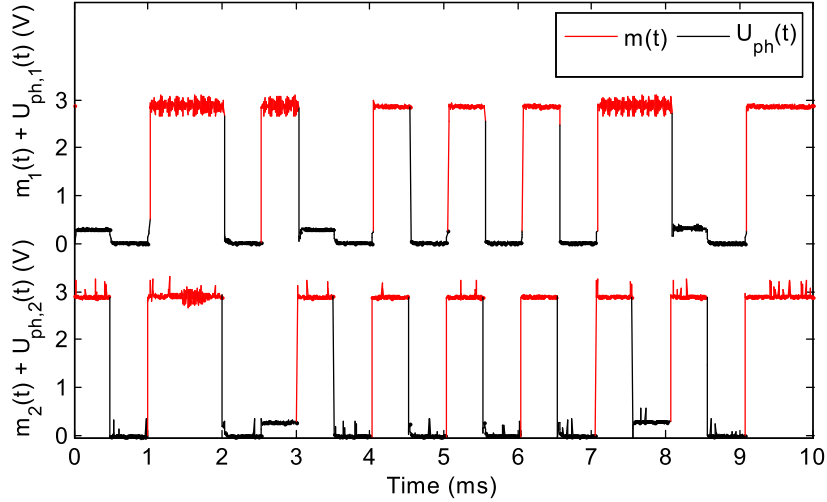


Figure 6.10: Transmitted and detected waveforms of L1 and L2.

6.6.2 Coding performance

We consider two LED prototype devices L1 and L2 that are separated by distance d , with side A facing each other. They both implement VLC with Manchester coding and transmit payload data simultaneously. Specifically, L1 transmits a char symbol 'a' with a binary ASCII code of $\underline{s}_1 = (0, 1, 1, 0, 0, 0, 0, 1)$ and L2 transmits another char symbol '@' with a binary ASCII code of $\underline{s}_2 = (0, 1, 0, 0, 0, 0, 0, 0)$. We have a symbol duration $T_s = 1$ ms and assume a perfect symbol-level and frame-level synchronization between L1 and L2.

The TIA output signal and the modulated signal of L1 and L2 are shown in Fig. 6.10. The x-axis is time in millisecond and y-axis is the voltage measurements in volt. The threshold voltage V_θ is assigned with 100 mV and the starting of first payload symbol is at $t = 500 \mu s$. During the subsequent 8 symbol duration, L1 and L2 demodulator outputs are $\underline{c}_1 = (0, 0, 1, 0, 0, 0, 0, 1)$ and $\underline{c}_2 = (0, 0, 1, 0, 0, 0, 0, 1)$. We decode the data sequences as

$$\begin{aligned}\hat{\underline{s}}_2 &= \underline{s}_1 \oplus \underline{c}_1 = (0, 1, 0, 0, 0, 0, 0, 0), \\ \hat{\underline{s}}_1 &= \underline{s}_2 \oplus \underline{c}_2 = (0, 1, 1, 0, 0, 0, 0, 1).\end{aligned}\tag{6.9}$$

The results are consistent with the transmitted data sequence with zero bit error.

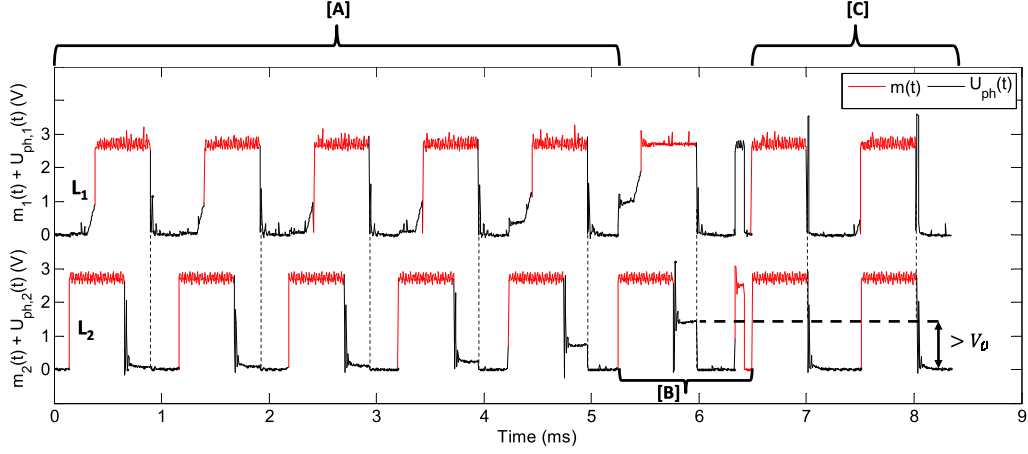


Figure 6.11: Symbol-level synchronization and illumination compensation. Phase [A]: LOS channel is restored by gradually removing an obstruction between two transceivers. Phase [B]: symbol-level synchronization plus illumination compensation. Phase [C]: successful symbol-level synchronization.

6.6.3 Synchronization performance

In Fig. 6.11 we show the synchronization of L1 and L2 using the proposed symbol-level synchronization scheme. Initially, both transceivers are asynchronous and stay at idle state, transmitting symbol '1'. The distance between the devices is chosen to be within the sensing range. The line-of-sight (LOS) path is blocked by a dark object such that synchronization will not be triggered until the object is removed. At stage [A], around 1 ms, we remove the dark object. In response, a positive square wave is observed by L1 and L2 during each sensing period. The square wave amplitude increases as LOS is restored and its width determines the phase offset between L1 and L2. According to Fig. 6.6, L2 is phase-leading and will delay to compensate for the phase offset. This happens at stage [B], where the amplitude of the square wave is beyond a threshold voltage V_θ . In addition, L2 outputs a narrow square wave at the end of this stage [B]. It corresponds to the illumination compensation waveform as illustrated in Fig. 6.8b. At the beginning of stage [C], L1 and L2 are in-phase, as a consequence of the fast synchronization achieved in one symbol duration.

In Fig. 6.12 we show the synchronization of two transceivers L1 and L2 using the proposed frame-level synchronization scheme. At stage [A], two transceivers have been synchronized using the symbol-level synchronization scheme. They are placed within the communication range and both are transmitting idle sym-

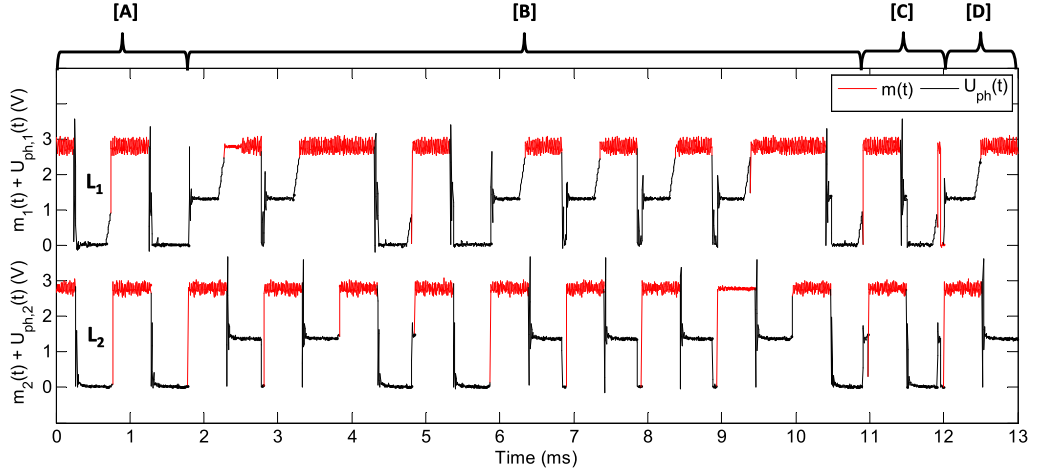


Figure 6.12: Frame-level synchronization and illumination compensation.

bols '1'. At the beginning of stage [B], only L1 is scheduled to transmit a frame (ASCII code of a char symbol 'a'). The corresponding frame symbols are therefore $(0, 0, 1, 1, 0, 0, 0, 0, 1, 1)$ and take 10 ms for transmission. During stage [B], L1 and L2 measure spikes as a consequence of the clock drift. This phase error accumulates over time. Correction is made by the stop symbol of the frame as shown at the stage [C]. In this case, L1 is phase-leading and is delayed to compensate for the phase offset. Two narrow pulses are observed around 12 ms. The upper one with larger amplitude corresponds to the illumination compensation behavior of L1. The other with smaller amplitude is the L2 response to L1. By the end of stage [C], L1 and L2 are time aligned at both symbol-level and frame-level. The start symbol at state [D] indicates transmission of a new frame by L1.

6.6.4 Communication performance

In this section, we evaluate the communication performance with respect to sensing distance, data rate and illumination level. We consider two transceivers L1 and L2 in dark room conditions, communicating via a LOS path at a distance d . A packet P_0 comprising a single physical layer frame is locally stored at each transceiver and is transmitted 1000 times. The threshold voltage V_θ is preset at the transceivers to allow a communication range of at least 10 cm. Before communication, a number of idle symbols ('1') are transmitted to allow symbol-level synchronization. Afterwards, packets are repeatedly transmitted following a manner shown in Fig. 6.12. Upon receiving of a complete packet, the decoder

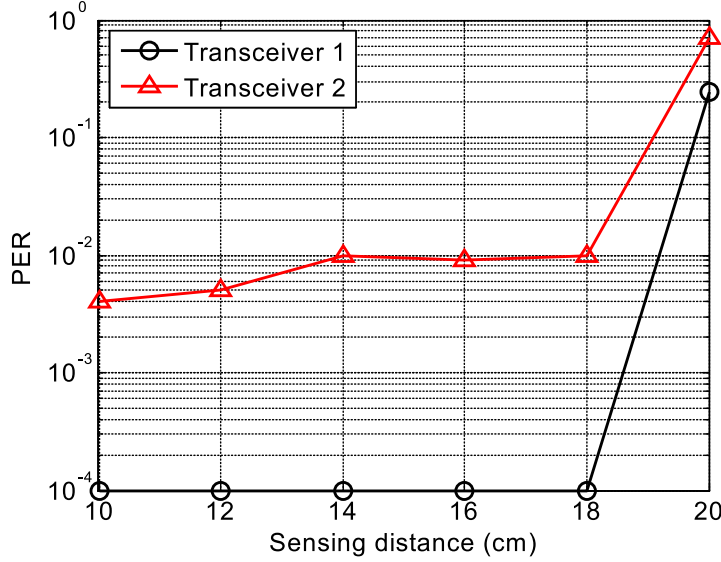


Figure 6.13: Packet error rate over sensing distance d : duty cycle $q = 0.5$, symbol duration $T_s = 1$ ms.

output is compared with the locally stored packet P_0 . The resulting packet error rate (PER) is the performance evaluation metric applied to three experiments below. The zero PER value is replaced with 10^{-4} for plot in log-scale.

Fig. 6.13 shows the impact of sensing distance d on PER. We keep the symbol duration $T_s = 1$ ms. The corresponding data rate $R = 800$ bps, taking into account one start symbol and one stop symbol as the frame overhead. The ON duty cycle q of modulated square wave $m(t)$ is assigned with 0.5 such as to achieve an illumination level of 50%. Sensing distance d is increased from 10 cm till 20 cm in steps of 2 cm and PER is collected at each position. Since the light intensity reduces with propagation distance, the average sample vector \underline{U} decreases over d . It approaches the threshold V_θ at $d = 20$ cm, and a much higher error rate is obtained using the demodulation scheme (6.3). For a luminaire source with α LEDs and a sensing luminaire with β LEDs branches in parallel, it can be shown that the effective sensing range is improved by a factor of $\sqrt{\alpha\beta}$ [28], [31]. Thus a reliable communication range of a few meters is feasible using luminaires with hundreds of LEDs.

Fig. 6.14 shows PER values for different values of data rate R . The sensing distance is fixed at 10 cm and the illumination level at 50%. We change the symbol duration $T_s = 1/R$ in a range between $200 \mu s$ and 1 ms in steps of $200 \mu s$ for the higher data rate scenario and select $T_s = 1$ ms, 2 ms, 4 ms, 6 ms and 8 ms

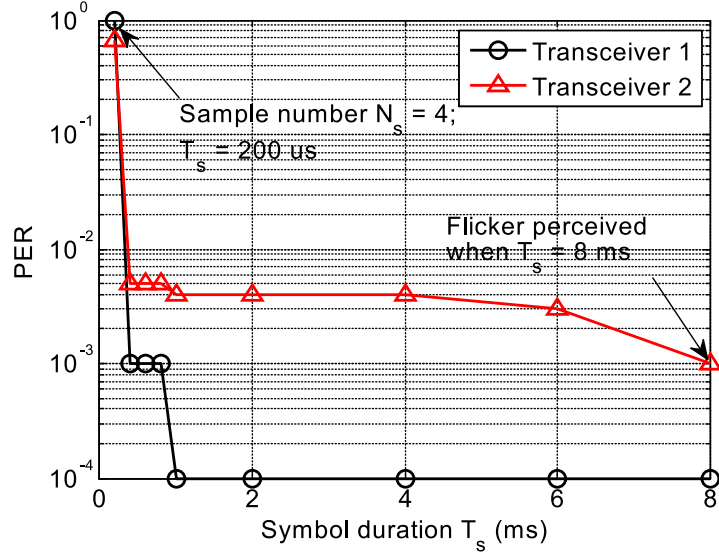


Figure 6.14: Packet error rate over data rate $R = \frac{1}{T_s}$: duty cycle $q = 0.5$, sensing distance $d = 10$ cm.

for the lower data rate case. The largest data rate is achieved at $T_s = 200 \mu s$ at the cost of a high PER value due to limited sample number for successful synchronization and decoding. The PER value drops below 10^{-2} by choosing $T_s = 400 \mu s$, while providing the highest possible data rate $R = 2$ kbps. The lower bound of data rate is found at $T_s = 6$ ms, beyond which perceivable flicker occurs. The upper bound of data rate is mainly determined by three factors: the ADC sampling frequency, the noisy output signal of TIA and the response time of transceiver.

The transceiver response time dominates among these factors, provided we have a sufficient sampling frequency at the ADC and a low-noise broadband amplifier. It is a function of the LED modulation characteristics, in both the illumination and sensing modes.

1. In diodes used for solid-state lamp applications, the current-injected p-n junction area is large. The resulting large capacitance limits the maximum modulation frequency, $f_{3dB}^{(emit)}$, [31] by

$$f_{3dB}^{(emit)} = \frac{\sqrt{3} \ln 9}{\pi(\tau_r + \tau_f)}, \quad (6.10)$$

where τ_r and τ_f are respectively the rise and fall time of the LED and are functions of the LED resistance and capacitance.

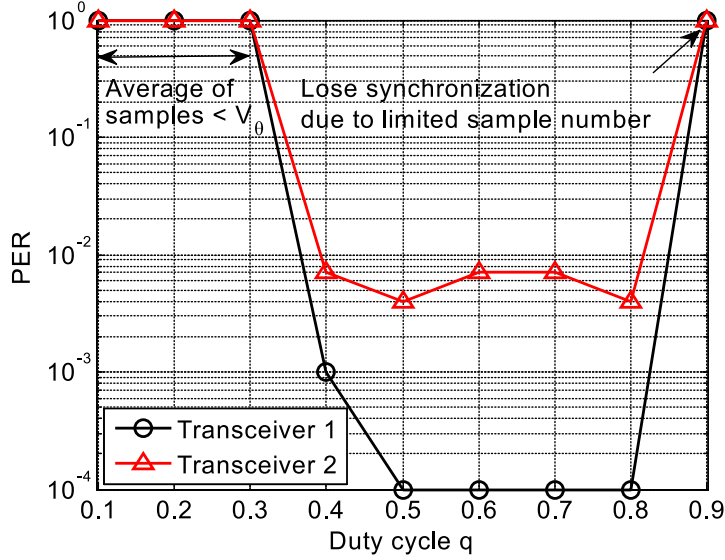


Figure 6.15: Packet error rate over duty cycle q : symbol duration $T_s = 1$ ms, sensing distance $d = 10$ cm.

2. In sensing mode, the LED modulation bandwidth [32] is

$$f_{3\text{dB}}^{(\text{sense})} = \sqrt{\frac{\text{GBW}}{2\pi R_F (C_F + C_D)}}, \quad (6.11)$$

where GBW, R_F , C_F and C_D are respectively the gain bandwidth of the TIA, the feedback resistance, the noise reducing capacitance and the LED equivalent capacitance.

Considering the two scenarios above in which the LED can operate (either sensing or emitting) gives a lower bound of the symbol duration T_s as

$$T_s \geq \frac{2}{\min\left(f_{3\text{dB}}^{(\text{emit})}, f_{3\text{dB}}^{(\text{sense})}\right)}, \quad (6.12)$$

which in turn provides an upper bound for the data rate. Note that the numerator is 2 because there are two slots (one emitting slot and one sensing slot) per symbol duration.

Fig. 6.15 shows the PER performance with respect to illumination level. The sensing distance is fixed at 10 cm and the symbol duration T_s at 1 ms. The illumination level is determined by the ON duty cycle q within a symbol duration

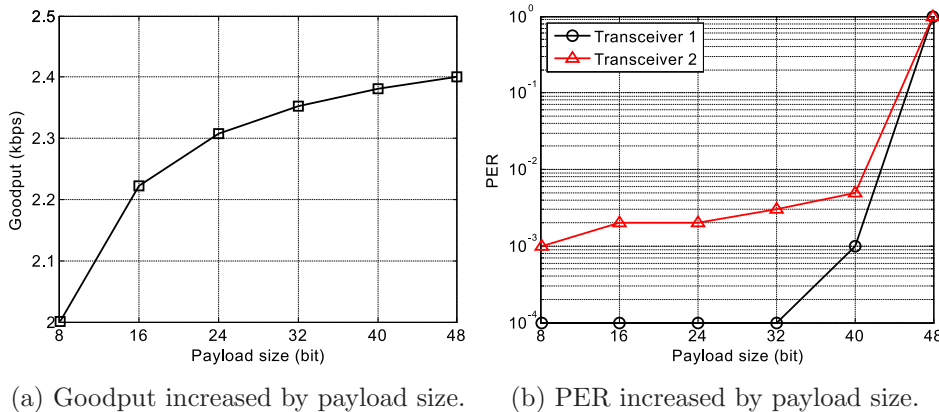


Figure 6.16: Packet error rate over payload size: symbol duration $T_s = 400 \mu\text{s}$, duty cycle $q = 0.5$, sensing distance $d = 10 \text{ cm}$.

T_s . We change q from 10% to 90% in steps of 10%. Small PER values are observed for $40\% \leq q \leq 80\%$. For any q that is below 40%, the average of measured voltage signal is always below the preset threshold V_θ . As such, neither synchronization nor decoding is feasible. For q that is above 80%, only a limited number of samples per T_s are used for synchronization and decoding, leading to a large PER.

Due to the overhead of start and stop symbols, the effective data rate (goodput) is lower than $\frac{1}{T_s}$. The goodput may be increased by transmitting more bits per frame. We study the impact of increasing payload size on goodput and PER in Fig. 6.16. Consider Fig. 6.16a. Let T_s equal $400\mu\text{s}$, a goodput of 2 kbps is achieved by transmitting a 8-bit payload per frame. The goodput approaches an upper bound of 2.5 kbps as the payload size increases. The trade-off between PER and payload size is shown in Fig. 6.16b. The PER values are below 10^{-2} for payload size less than 40 bits. A goodput of 2.381 kbps is achieved in both directions by transmitting a 40-bit payload. Note that the oscillator frequency difference between the two transceivers (0.048 MHz in the setup) generates a phase error which accumulates during the frame transmission. A transceiver corrects the phase error only once at the stop symbol, using symbol-level synchronization. When transmitting a 48-bit payload, the decoding fails in the latter part of each frame. This results in an increase in PER values as shown in Fig. 6.16b.

6.7 Conclusions and discussions

We presented the design of a two-way VLC system with LEDs used as transceivers and also for illumination. We showed that for time-slotted VLC, the combination of Manchester coding and OOK modulation achieves the optimum trade-off between system rate and illumination. This scheme was used for data transmission along with a simple XOR decoding scheme at the receiver. At the receiver, OFF periods in the signal waveform were used for retrieving the transmitted information. We implemented a proof-of-concept LED prototype system with low-power single red LED and showed that data rates in the order of kbps could be achieved at a distance of a few tens of cm. For luminaires with hundreds of LEDs, a communication range in the order of a few meters can thus be feasible.

Two-way VLC is feasible between any two LEDs with overlapped emitting and sensing spectra. The LED material technology determines the spectral characteristics and the LED sensitivity, and as a result on communication performance. A detailed study of the impact of different LED material technologies on communication performance is beyond the scope of this study and is a subject of future work.

Appendix

6.A Rate-illumination trade-off

We consider the two-way communication channel model [25] in order to analyze feasible rate-illumination pairs. The system response considered earlier in Table 6.1 in Section 6.2 can be expressed as a system truth table given in Table 6.A.1. In this table, the input indicates whether the LED is in emitting or sensing mode. The output of the LED is related to the receiving state. For example, if the LED is in sense input state and the other LED is in emit input state, the output will be light. In the table, we have replaced the sensing mode by '0' and the emitting mode by '1' in the input state. Also, we replaced no light by '0', light by '1' and unknown by '?' in the output state. Inputs are named x and outputs y . Each transceiver can replace '?' by '1', since it knows that

Table 6.A.1: System truth table.

input1	input2	output1	output2	x_1	x_2	y_1	y_2	y
sense	sense	no light	no light	0	0	0	0	0
sense	emit	light	unknown	0	1	1	?	1
emit	sense	unknown	light	1	0	?	1	1
emit	emit	unknown	unknown	1	1	?	?	1

'1' means '?' if its input was '1'. This leads to a two-way OR-channel with a common output $y = x_1 \text{OR} x_2$.

The system performance is characterized by the illumination level and communication rate. Consider a block of N slots. In this block, a message $z_1 \in \{1, 2, \dots, M_1\}$ is sent via transceiver L1 to another transceiver L2. Meanwhile, a message $z_2 \in \{1, 2, \dots, M_2\}$ is sent via L2 to L1. Assuming messages are uniform and independent of each other, codewords e_1 and e_2 are selected to transmit them.

$$(x_{11}, x_{12}, \dots, x_{1N}) = e_1(z_1), \quad (6.13)$$

$$(x_{21}, x_{22}, \dots, x_{2N}) = e_2(z_2). \quad (6.14)$$

The probability of a 1 in N -bit codeword determines the illumination value. For

CHAPTER 6. TWO-WAY VISIBLE LIGHT COMMUNICATION AND ILLUMINATION WITH LEDS

some probability distribution Q , the total illumination values accumulate as

$$\Phi_1 = \mathbb{E} \left[\sum_{n=1, N} x_{1n} \right], \quad (6.15)$$

$$\Phi_2 = \mathbb{E} \left[\sum_{n=1, N} x_{2n} \right]. \quad (6.16)$$

The received sequences are decoded at two sides

$$\hat{z}_2 = g_1(y_1, y_2, \dots, y_N, z_1), \quad (6.17)$$

$$\hat{z}_1 = g_2(y_1, y_2, \dots, y_N, z_2), \quad (6.18)$$

where they both use the knowledge about their own message and employ a decoder $g(\cdot)$. The probabilities of error are described by

$$P_{e1} = \Pr\{\hat{z}_1 \neq z_1\}, \quad (6.19)$$

$$P_{e2} = \Pr\{\hat{z}_2 \neq z_2\}. \quad (6.20)$$

We want to find out how large M_1 and M_2 can be, in combination with acceptably small P_{e1} and P_{e2} , and desired total illumination values Φ_1 and Φ_2 . We say that a rate-illumination quadruple $(\rho_1, \rho_2, \lambda_1, \lambda_2)$ is achievable if there exist encoders and decoders that achieve for all $\epsilon > 0$ and large enough N

$$\log_2 M_1 \geq N(\rho_1 - \epsilon), \quad (6.21)$$

$$\log_2 M_2 \geq N(\rho_2 - \epsilon), \quad (6.22)$$

$$\Phi_1 \geq N(\lambda_1 - \epsilon), \quad (6.23)$$

$$\Phi_2 \geq N(\lambda_2 - \epsilon), \quad (6.24)$$

$$P_{e1} \leq \epsilon, \quad (6.25)$$

$$P_{e2} \leq \epsilon. \quad (6.26)$$

First we derive an upper bound on the achievable information rates. In the

derivation F denotes the Fano term.

$$\begin{aligned}
 \log_2 M_1 &\leq H(Z_1) = H(Z_1) - H(Z_1|Y^N, Z_2) + F \\
 &= I(Z_1; Y^N, Z_2) + F \\
 &= I(Z_1; Y^N | Z_2) + F \\
 &= \sum_{n=1}^N I(Z_1; Y_n | Z_2, Y^{n-1}) + F \\
 &\leq \sum_{n=1}^N H(Y_n | Z_2, Y^{n-1}, X_{2n}) + F \\
 &\leq \sum_{n=1}^N H(Y_n | X_{2n}) + F \\
 &\leq \sum_{n=1}^N P(X_{2n} = 0) + F.
 \end{aligned}$$

Similarly we can show that

$$\log_2 M_2 \leq \sum_{n=1}^N P(X_{1n} = 0) + F.$$

Moreover now

$$\begin{aligned}
 \Phi_1 &= \sum_{n=1}^N P(X_{1n} = 1), \\
 \Phi_2 &= \sum_{n=1}^N P(X_{2n} = 1).
 \end{aligned}$$

If a rate-illumination quadruple $(\rho_1, \rho_2, \lambda_1, \lambda_2)$ is achievable, it has to satisfy

$$\begin{aligned}
 \rho_1 + \lambda_2 &\leq \frac{1}{N} \log_2 M_1 + \frac{1}{N} \Phi_2 + 2\epsilon \\
 &\leq \frac{1}{N} \left(\sum_{n=1}^N P(X_{2n} = 0) + F \right) + \frac{1}{N} \sum_{n=1}^N P(X_{2n} = 1) + 2\epsilon \\
 &\leq 1 + F/N + 2\epsilon.
 \end{aligned}$$

For $\epsilon \downarrow 0$ the term F/N disappears and we obtain that

$$\begin{aligned}
 \rho_1 + \lambda_2 &\leq 1, \text{ and similarly that} \\
 \rho_2 + \lambda_1 &\leq 1.
 \end{aligned}$$

CHAPTER 6. TWO-WAY VISIBLE LIGHT COMMUNICATION AND
ILLUMINATION WITH LEDS

The Manchester coding plus OOK modulation has achieved $\rho_1 = \rho_2 = 1/2$ and $\lambda_1 = \lambda_2 = 1/2$, and is therefore optimal in providing illumination and system rate.

REFERENCES

- [1] T. Komine and M. Nakagawa, “Fundamental analysis for visible-light communication system using LED lights,” *IEEE Transactions on Consumer Electronics*, vol. 50, no. 1, pp. 100–107, February 2004.
- [2] H. Yang, T. C. W. Schenk, J. W. M. Bergmans, and A. Pandharipande, “Enhanced illumination sensing using multiple harmonics for LED lighting systems,” *IEEE Transactions on Signal Processing*, vol. 58, no. 11, pp. 5508–5522, 2010.
- [3] S. Rajagopal, R. D. Roberts, and S. K. Lim, “IEEE 802.15.7 visible light communication: modulation schemes and dimming support,” *IEEE Communications Magazine*, vol. 50, no. 3, pp. 72–82, March 2012.
- [4] G. Corbellini, K. Aksit, S. Schmid, S. Mangold, and T. R. Gross, “Connecting networks of toys and smartphones with visible light communication,” *IEEE Communications Magazine*, vol. 52, no. 7, pp. 72–78, July 2014.
- [5] P. Dietz, W. Yeraunus, and D. Leigh, “Very low-cost sensing and communication using bidirectional LEDs,” *5th International Conference on Ubiquitous Computing*, pp. 175–191, 2003.
- [6] S. Li, A. Pandharipande, and F. M. J. Willems, “Daylight sensing LED lighting system,” *IEEE Sensors Journal*, vol. 16, no. 9, pp. 3216–3223, May 2016.
- [7] S. Li and A. Pandharipande, “LED-based color sensing and control,” *IEEE Sensors Journal*, vol. 15, no. 11, pp. 6116–6124, November 2015.
- [8] D. Giustiniano, N. O. Tippenhauer, and S. Mangold, “Low-complexity visible light networking with LED-to-LED communication,” *IFIP Wireless Days*, pp. 1–8, November 2012.
- [9] S. Schmid, G. Corbellini, S. Mangold, and T. R. Gross, “An LED-to-LED visible light communication system with software-based synchronization,” *IEEE Globecom Workshops*, pp. 1264–1268, December 2012.
- [10] S. Schmid, G. Corbellini, S. Mangold, and T. R. Gross, “Continuous synchronization for LED-to-LED visible light communication networks,” *3rd International Workshop in Optical Wireless Communications*, pp. 45–49, September 2014.

CHAPTER 6. TWO-WAY VISIBLE LIGHT COMMUNICATION AND ILLUMINATION WITH LEDS

- [11] Q. Wang, D. Giustiniano, and D. Puccinelli, “An open-source research platform for embedded visible light networking,” *IEEE Wireless Communications*, vol. 22, no. 2, pp. 94–100, 2015.
- [12] Q. Wang and D. Giustiniano, “Intra-frame bidirectional transmission in networks of visible LEDs,” *IEEE/ACM Transactions on Networking*, vol. 24, no. 6, pp. 3607–3619, December 2016.
- [13] S. Li, A. Pandharipande, and F. M. J. Willems, “Unidirectional visible light communication and illumination with LEDs,” *IEEE Sensors Journal*, vol. 16, no. 23, pp. 8617–8626, December 2016.
- [14] H. Elgala, R. Mesleh, and H. Haas, “Indoor optical wireless communication: potential and state-of-the-art,” *IEEE Communications Magazine*, pp. 56–62, September 2011.
- [15] P. H. Pathak, X. Feng, P. Hu, and P. Mohapatra, “Visible light communication, networking, and sensing: A survey, potential and challenges,” *IEEE Communications Surveys Tutorials*, vol. 17, no. 4, pp. 2047–2077, 2015.
- [16] Z. Wu, J. Chau, and T. Little, “Modeling and designing of a new indoor free space visible light communication system,” *16th European Conference on Networks and Optical Communications*, pp. 72–75, July 2011.
- [17] N. Rajagopal, P. Lazik, and A. Rowe, “Hybrid visible light communication for cameras and low-power embedded devices,” in *Proceedings of the 1st ACM MobiCom Workshop on Visible Light Communication Systems*, pp. 33–38, July 2014.
- [18] L. Klaver and M. Zuniga, “Shine: A step towards distributed multi-hop visible light communication,” *IEEE 12th International Conference on Mobile Ad Hoc and Sensor Systems*, pp. 235–243, 2015.
- [19] H. Yang and A. Pandharipande, “Full-duplex relay VLC in LED lighting triangular system topology,” *6th International Symposium on Communications, Control and Signal Processing*, pp. 85–88, May 2014.
- [20] H. Yang and A. Pandharipande, “Full-duplex relay VLC in LED lighting linear system topology,” *Annual Conference of the IEEE Industrial Electronics Society*, pp. 6075–6080, November 2013.
- [21] Y. Wang, L. Tao, X. Huang, J. Shi, and N. Chi, “8-Gb/s RGBY LED-based WDM VLC system employing high-order CAP modulation and hybrid post equalizer,” *IEEE Photonics Journal*, vol. 7, no. 6, pp. 1–7, December 2015.

-
- [22] J. J. D. McKendry, D. Massoubre, S. Zhang, B. R. Rae, R. P. Green, E. Gu, R. K. Henderson, A. E. Kelly, and M. D. Dawson, "Visible-light communications using a CMOS-controlled micro-light-emitting-diode array," *Journal of Lightwave Technology*, vol. 30, no. 1, pp. 61–67, January 2012.
- [23] R. X. G. Ferreira, E. Xie, J. J. D. McKendry, S. Rajbhandari, H. Chun, G. Faulkner, S. Watson, A. E. Kelly, E. Gu, R. V. Penty, I. H. White, D. C. O'Brien, and M. D. Dawson, "High bandwidth GaN-based micro-LEDs for multi-Gb/s visible light communications," *IEEE Photonics Technology Letters*, vol. 28, no. 19, pp. 2023–2026, October 2016.
- [24] Schmid, Stefan, G. Corbellini, S. Mangold, and T. R. Gross, "LED-to-LED visible light communication networks," *Proceedings of the Fourteenth ACM International Symposium on Mobile Ad Hoc Networking and Computing*, pp. 1–10, 2013.
- [25] C. E. Shannon, "Two-way communication channels," *Proceedings of the Fourth Berkeley Symposium on Mathematical Statistics and Probability*, pp. 611–644, 1961.
- [26] T. Koike-Akino, P. Popovski, and V. Tarokh, "Optimized constellations for two-way wireless relaying with physical network coding," *IEEE Journal on Selected Areas in Communications*, vol. 27, no. 5, pp. 773–787, June 2009.
- [27] R. Vaze, K. T. Truong, S. Weber, and R. W. Heath, "Two-way transmission capacity of wireless ad-hoc networks," *IEEE Transactions on Wireless Communications*, vol. 10, no. 6, pp. 1966–1975, June 2011.
- [28] S. Li, A. Pandharipande, and F. M. J. Willems, "Redundant run-length limited encoding for two-way visible light communication," *Annual Conference of the IEEE Industrial Electronics Society*, pp. 4706–4712, October 2016.
- [29] "Vishay semiconductors measurement techniques," July 2012, accessed March 2016. [Online]. Available: <http://www.vishay.com/docs/80085/measrem.pdf>
- [30] "Texas instruments msp430f2274 transimpedance amplifier users guide," August 2014, accessed January 2016. [Online]. Available: <http://www.ti.com/lit/ug/tidu443/tidu443.pdf>
- [31] E. Schubert, *Light-Emitting Diodes*. Cambridge University Press, 2006.

CHAPTER 6. TWO-WAY VISIBLE LIGHT COMMUNICATION AND
ILLUMINATION WITH LEDS

- [32] T. Wang and B. Erhman, “Compensate transimpedance amplifiers intuitively,” Texas Instruments Application Report No. SBOA055A, March 2005, accessed June 2016. [Online]. Available: <http://www.ti.com/lit/an/sboa055a/sboa055a.pdf>

Chapter 7

Conclusions and further research

Conclusions

In this thesis, we explored the use of light emitting diodes (LEDs) as wavelength-selective light sensors, along with providing illumination. This sensing functionality was explored for three applications: color sensing and control, daylight adaptive control and visible light communication (VLC).

7.1 Color sensing and control

In the RGB (red, green, blue) color space, sensing arbitrary colors requires estimation of primary color contributions. In Chapter 2, we proposed two estimation algorithms: the sensitivity matrix based color estimation method and the discrete wavelet transform (DWT) based color estimation method. The estimation was done based on RGB LEDs measurements, without using dedicated optical filters and light sensors.

As light sensors, RGB LEDs are mostly sensitive to light at slightly shorter wavelengths than at which they emit. We constructed a 3-by-3 sensitivity matrix based on the wavelength selectivity of RGB LEDs. Estimation of primary color contributions was then obtained as a solution to a constrained optimization problem, provided that the sensitivity matrix is well-conditioned. One such example was the sensitivity matrix \mathbf{S}_1 in Chapter 2, which characterizes the sensitivity of a ColorTransporter to the light emitted by a source RGB lamp.

The LED material technology determines the LED wavelength selectivity, and has an impact on the color estimation performance using the sensitivity matrix based method. In Chapter 2, we showed that the sensitivity matrix \mathbf{S}_2 , which specifies the sensitivity of a destination RGB lamp to the light emitted by a ColorTransporter, is ill-conditioned. In this case, the sensitivity matrix based method cannot be applied. Instead, we used the DWT based method, where we detected the pulse width modulation (PWM) duty cycle of the emitted red, green and blue light by analyzing singular points in the RGB LEDs measurements. The singular points correspond to the discontinuities of the RGB LEDs measurements. Such discontinuities are of type I and can be efficiently detected with the db1 (Haar) wavelet analysis, which provides the following information: (i) The location of a singular point, i.e. the time instance. (ii) The type and amplitude of a singular point, e.g. the global maximum p_1 and the global minimum n_1 . The above information allows for the duty cycle vector estimation using Eq. (2.11) and Eq. (2.12) in Chapter 2.

In addition to the color estimation algorithms, in Chapter 2 we also proposed a dual-mode LED driver design and a sensing and dimming control protocol

in order to meet the following technical challenges: (i) How to sense without causing flicker in illumination? (ii) How to maintain the low complexity of an interactive LED lamp application? We summarize our contributions towards the first sub-goal of the thesis as follows:

Sub-goal 1: *To develop a prototype system that makes use of the LED wavelength selectivity to provide new ways of light interaction, without dedicated light sensors.*

Contributions:

In Chapter 2, we proposed a LED system prototype with source and destination LED lamps and a LED array as a ColorTransporter device. A color sensing and illumination driver protocol was presented such that the LED lamps could sense color while illuminating without perceivable flicker. A similar protocol was used at the LED array transporter device with the additional use of hardware triggers to have the device operate either in sensing or illumination mode. The LED operates in the photovoltaic sensing mode, wherein the photovoltage is measured across an extra load resistor with limited hardware modification. Two color estimation methods were presented to map the measured photovoltage on the red, green and blue channels to a sensed color. The methods were implemented in micro-controller unit software, which also implemented digital control of power conversion in the illumination mode. The proposed color estimation methods were evaluated using an error metric based on a normalized color RGB model. Evaluation of the sensitivity matrix based method showed that it is possible to detect colors efficiently, provided that the sensitivity matrix is well-conditioned.

Efficient detection of colors in the RGB color space using the inherent wavelength selectivity of multi-color LEDs opens up opportunities to save extra color filters that are otherwise required by: (i) color shift keying modulation in the IEEE 802.15.7 standard [1]; (ii) wavelength division multiplexing multiple-input and multiple-output (MIMO) LED-to-LED VLC system.

Evaluation of the DWT based method showed that it is possible to detect colors efficiently even if the sensitivity matrix is ill-conditioned, with exceptions of monochromatic color. By applying wavelet analysis on the waveform of monochromatic color, we can find only one singular point. However, it can also be treated as two overlapped singular points in response to a mix of two different colors with equal portions. In order to detect monochromatic color, we may consider a suitable combination of both methods.

The perceivable flicker analysis was conducted with a fixed flicker frequency,

which was twice the mains frequency. This frequency is above the critical flicker frequency (CFF) of the human eye for a dynamic luminance level in a range between 0 and 3000 cd/m². As the luminance level goes beyond 3000 cm/m², we may consider decreasing the sensing slot, $t_d + t_s$, using an ADC with a high sampling rate or by taking fewer samples using the same ADC. In practice, flicker sensitivity also depends on the color of the stimulus (the chromatic flicker) and the observer (e.g. location of the stimulus on the retina and the size of the stimulus). Adaptation of the design space to these parameters is a topic of further research.

7.2 Daylight adaptive control

From Fig. 1.4 in Chapter 1, we know that a blue LED is most sensitive to ultraviolet A (UV-A) light and its measurements are largely due to the effect of daylight. Blue LEDs are commonly used to produce white light, with phosphor coating. Such phosphor-converted white (pc-white) LEDs have been widely used to provide general indoor illumination. Therefore, they can be reused as daylight sensors for daylight adaptive lighting control applications, saving extra sensor cost and commissioning effort.

We considered the integration of daylight sensing functionality of pc-white LEDs in a daylight adaptive lighting control system. An array of white LEDs was reused to detect daylight contribution and compensate for it such that the net illumination level meets the desired value. Integration of daylight sensing functionality brought the following technical challenges: (i) How to drive pc-white LEDs for both daylight sensing and illumination, without causing flicker? (ii) How to control the dimming level of pc-LEDs, based on pure daylight measurements? Our contributions towards the second sub-goal of this thesis are as follows:

Sub-goal 2: *To develop an autonomously controlled LED lighting system that can sense and adapt to daylight changes, without dedicated light sensors.*

Contributions:

In Chapter 3, we presented a LED luminaire prototype that can provide the dual functionalities of illumination and daylight sensing. The illumination is determined by controlling a PWM signal. In OFF periods of the PWM signal, the LED luminaire senses daylight contribution. The sensing mode was added with limited hardware changes. For daylight sensing, the LED luminaire was calibrated under daylight conditions. The calibration function relates a photo-

voltage signal measured in OFF periods of PWM signal to an estimated daylight level at the workspace under the luminaire. The LED luminaire was controlled using an open-loop control law. The performance of the proposed daylight sensing lighting control system was compared with a photodetector based lighting control system and shown to offer more robustness in the presence of reflectance changes in the environment. The proposed solution saves extra cost and installation complexity involved in current lighting control systems that use external photodetectors.

The proposed daylight sensing based lighting control system assumed a centralized structure, such that the illumination contribution of one luminaire at the workspace under another luminaire is known at the central controller (via a calibration function). For a distributed structure, an exchange of dimming levels between neighboring luminaires would be required. Such inter-luminaire communication can be realized using RF modules. Alternatively, an optical link between LED luminaires can be incorporated using inter-luminaire VLC. Since a phosphor-converted white LED luminaire is not sufficiently sensitive to the artificial light it emits, a dedicated photodiode is required as a receiver in order to establish the optical link between neighboring luminaires.

7.3 LED-to-LED visible light communication

LEDs may also be used to receive modulated optical signals coming from VLC transmitters. A LED-to-LED VLC link is feasible so long as there is an overlap between the sensing spectrum of receiving LEDs and the spectrum of transmitting LEDs.

7.3.1 Unidirectional VLC and illumination with LEDs

The visible light from a VLC transmitter is modulated to embed information (e.g. the luminaire identifier in an indoor positioning system), while providing flicker-free illumination in a certain dimming range. The receiving LEDs, which could be the LED screen or LED flashlight on a smart device, can demodulate the information while providing a steady light output. A number of technical challenges need to be addressed to realize LED-to-LED VLC and illumination: (i) How should information be encoded at the VLC transmitter that facilitates simple decoding at the LED receiver? (ii) How does the decoding mechanism work, given that the LED is used for both VLC reception and providing illumination? Our contributions towards the third sub-goal of this thesis are now summarized:

Sub-goal 3: *To provide flick-free illumination and unidirectional visible light communication between two LED devices, without dedicated light sensors.*

Contributions:

In Chapter 4, we proposed the design of a prototype system with two LED devices for unidirectional VLC while also providing illumination. The devices use the LEDs themselves for data transmission and reception, without additional dedicated light sensors. At the transmitter, a redundant run-length limited encoding scheme was considered for data transmission. We adopt the standard 4B6B RLL code that is DC-balanced and has the benefit of limiting flicker. The redundant bits were added such that decoding was realized with a simple threshold detection scheme and edge detection. Multi-level dimming was considered for illumination, providing a wide dimming range between 0.1 and 0.9 without causing flicker. The receiver modulates a dedicated sensing bit sequence with on-off keying and uses the OFF periods for VLC reception. The sensing bit sequence was with alternating 1s and 0s for flicker-free illumination while providing a steady light output. The built prototype was evaluated in terms of bit error rate (BER) and illumination flicker performance. We showed that reliable communication at a rate of a few kbps was achievable, with illumination flicker comparable to conventional PWM dimming.

7.3.2 Adaptive VLC and illumination with LEDs

The proposed calibration scheme at the receiver in Chapter 4 assumed a fixed communication distance between the two LED devices. As the receiver moves further away from the transmitter, the received light power decreases following the inverse square law or worse. Decoding using a constant threshold would fail as the average of photovoltage measurements approaches and drops below the threshold. Further, the initially proposed calibration scheme is not robust against ambient light changes, e.g. slow daylight variations. In order to support receiver portability and robustness against daylight fluctuation in the unidirectional VLC system, the following technical challenges were addressed: (i) How should the receiver adapt threshold based on the photovoltage measurements? (ii) How should the transmitter allocate the transmission power for better communication performance, while providing a desired dimming level within a certain range? Our contributions towards the fourth sub-goal of this thesis are:

Sub-goal 4: *To support external light condition and communication distance*

changes in unidirectional LED-to-LED visible light communication system.

Contributions:

In Chapter 5, we presented the design of a LED-based VLC system where the LED is used for adaptive VLC transmission and reception, as well as for illumination. In the proposed design, the modulation index at the transmitter, as well as calibration detection thresholds at the receiver, are adapted to react to changes in ambient illumination conditions and limited LED device portability. At the transmitter side, we considered a weighted combination of a PWM signal and a redundant run length limited (RLL) encoded on-off keying (OOK) signal. The weights were designed to achieve a target dimming level and enhance the transmit signal-to-noise ratio. At the receiver, a method for adaptive threshold detection was proposed. Using an experimental prototype system, we showed an increase of almost 30% in reliable communication distance in comparison to a non-adaptive VLC system in Chapter 4.

7.3.3 Two-way VLC and illumination with LEDs

The dual use of LEDs for illumination and sensing can be treated as being analogous to transmitting and receiving information in a two-way channel [2]. The two-way channel was first introduced by Shannon [3] and the achievable rates were analyzed in an information-theoretic setting. Since then, the two-way channel has been studied in different wireless communication systems [4], [5]. The performance of two-way VLC systems has not yet been studied in the literature. We considered two-way VLC, where we used LEDs as both transmitters and receivers, without using dedicated light sensors as receivers. The system allows two LED devices to simultaneously transmit and receive information through a bi-directional VLC link. The following technical challenges were addressed to realize the two-way VLC system: (i) How should data encoding/decoding be designed to enable LEDs to transmit/receive for a two-way VLC, while also providing illumination without perceivable flicker? (ii) How should the LED devices be synchronized for two-way VLC? (iii) What are the communication and illumination trade-offs in such a system? Our contributions towards the fifth sub-goal of this thesis are as follows:

Sub-goal 5: *To provide flicker-free illumination and full-duplex visible light communication between two LED devices, without dedicated light sensors.*

Contributions:

In Chapter 6 we presented the design of a two-way VLC system with LEDs used as transceivers and also for illumination. We showed that for time-slotted VLC, the combination of Manchester coding and OOK modulation achieves the optimum trade-off between system rate and illumination. This scheme was used for data transmission along with a simple exclusive-or (XOR) decoding scheme at the receiver. At the receiver, OFF periods in the signal waveform were used for retrieving the transmitted information. We implemented a proof-of-concept LED prototype system with low-power single red LED and showed that data rates in the order of kbps could be achieved at a distance of a few tens of cm. For luminaires with hundreds of LEDs, a communication range in the order of a few meters can thus be feasible.

7.4 Recommendations for future research

The focus of this thesis was to explore the sensing functionality of LED in color sensing and control, daylight adaptive control and VLC applications, along with providing illumination. To demonstrate the feasibility of each application, we built proof-of-concept prototypes. In this section, we sketch several potential research topics and future directions.

7.4.1 Robust color control of multi-color LEDs

The LED sensitivity can be obtained via a calibration phase, as we have shown with color sensing application in Chapter 2 and daylight sensing application in Chapter 3. We were assuming the sensing LEDs are operating at room temperature, with a stable current-voltage characteristic during the experimental tests. In practice, both temperature change the LED lifespan shift the current-voltage characteristic [6]. Therefore, color sensing and control using multi-color LEDs require feedback mechanisms to compensate for the current-voltage characteristic shift. In the future, robust and low-cost solutions may be explored by considering:

- built-in sensors that are used to measure the temperature- and aging-induced sensitivity change occurring during operation of the LEDs.
- control methods that jointly address temperature feed-forward and flux feedback compensations.

7.4.2 Occupancy sensing with LEDs

In indoor lighting control applications, a luminaire adapts its light output to occupancy and daylight changes. In Chapter 3, we have shown the designed prototype of daylight sensing LED luminaires that can self-sense and adapt to daylight changes, without using dedicated light sensors. However, such a lighting system still requires dedicated occupancy sensors for performing occupancy adaptive control.

We propose a future research direction on reusing an array of multi-color LEDs for occupancy sensing over their field-of-view, while providing flicker-free white light output and daylight sensing functionality. Occupancy sensing is based on detection of reflectance changes under the LED luminaires that is caused by user movements. Specifically, we consider RGB LED luminaires. We use part of the LEDs (e.g. green LEDs) to emit beacons and use the rest (e.g. red LEDs) to detect changes of the reflected beacon signal. The daylight sensing functionality could be supported by the blue LEDs, while the combination of RGB LEDs is used to produce white light for illumination.

7.4.3 MIMO LED-to-LED VLC with multi-color LEDs

In Chapters 4, 5 and 6, we studied the illumination and communication performance of LED-to-LED VLC systems by developing proof-of-concept prototypes with a single red color LED at the front-end of transmitter and receiver. The VLC channel is, therefore, single-input and single-output (SISO). Future research directions could be:

- developing MIMO LEDs-to-LEDs VLC systems with multi-color LEDs at the front-end of VLC transmitter and receiver, including at least red, green and blue LEDs;
- evaluation of the illumination and communication trade-offs in MIMO LED-to-LED VLC systems;
- integration of daylight-adaptive control into the MIMO LED-to-LED system with the blue LED channel reused for daylight sensing;
- developing coding and modulation schemes for MIMO VLC transceivers with which they can provide flicker-free *white* light for illumination.

REFERENCES

- [1] 802.15.7 IEEE standard for local and metropolitan area networks, *part 15.7: Short Range Wireless Optical Communication Using Visible Light*, 2011.
- [2] S. Li, A. Pandharipande, and F. M. J. Willems, “Two-way visible light communication and illumination with LEDs,” *IEEE Transactions on Communications*, vol. 65, no. 2, pp. 740–750, February 2017.
- [3] C. E. Shannon, “Two-way communication channels,” *Proceedings of the Fourth Berkeley Symposium on Mathematical Statistics and Probability*, pp. 611–644, 1961.
- [4] T. Koike-Akino, P. Popovski, and V. Tarokh, “Optimized constellations for two-way wireless relaying with physical network coding,” *IEEE Communications Surveys and Tutorials*, vol. 27, no. 5, pp. 773–787, June 2009.
- [5] R. Vaze, K. T. Truong, S. Weber, and R. W. Heath, “Two-way transmission capacity of wireless ad-hoc networks,” *IEEE Transactions on Wireless Communications*, vol. 10, no. 6, pp. 1966–1975, June 2011.
- [6] C. Martiny and M. Wendt, “Intrinsic sensing and color control of multiLED lamp-modules,” *Philips Research, Eindhoven, The Netherlands, Tech. Rep. PR-TN 2006/00195*, 2006.

Summary

Sensing, communication and illumination with LED lighting systems

Lighting is witnessing a major technology shift towards semiconductors with the adoption of light emitting diodes (LEDs). Nowadays, lighting applications in homes, offices, and industries are typically equipped with LEDs. LED lighting outperforms conventional lighting in aspects like long lifetime, energy efficiency and high switching frequency. In addition to illumination, a LED is capable of sensing light if its bias is properly chosen. As a sensor, a LED is sensitive to light with wavelengths that are shorter than the illumination band wavelengths. The scope of this doctoral research is to study the double functionality of LEDs in applications that perform both illumination and sensing and to develop prototype systems that include sensing in addition to illumination.

The advent of LEDs in lamps is bringing about new consumer applications and products, focusing on innovative ways to control and interact with LED lamps. Our first sub-goal in this research is therefore: *Sub-goal 1: To develop a prototype system that makes use of the LED wavelength selectivity to provide new ways of light interaction, without dedicated light sensors.*

In Chapter 2, we proposed a LED system consisting of LED lamps and a LED array, where the LED array is used to sense and pick up the color of a source lamp. When the distance between the sensing array and the source lamp is within a certain range, the LED array holds the color of the source lamp and transports this color to a destination lamp. We present a design prototype of the LED lamps and the LED array in order to realize the double functionality, color sensing and illumination. A driving protocol is proposed that realizes color sensing without causing flicker during illumination. Depending on the wavelength sensitivity of the LED devices, two methods for color estimation are proposed. Experimental results are presented to evaluate the performance of the proposed methods.

With LED lighting systems, the light output can be flexibly and easily con-

SUMMARY

trolled. This is especially attractive for daylight adaptive lighting control for reducing the substantial portion of the electrical energy that is consumed by lighting. Our second sub-goal in this research is therefore: *Sub-goal 2: To develop an autonomously controlled LED lighting system that can sense and adapt to daylight changes, without dedicated light sensors.*

In Chapter 3, we proposed LED luminaires that can perform the double functionality of illumination and daylight sensing, obviating the need of additional light sensors. We present a daylight sensing luminaire prototype and investigate two driving protocols for sensing and illumination. Both driving protocols are based on open-loop control for adaptation to daylight. The proposed system is shown to be more robust to reflectance changes in comparison to a photodetector-based closed-loop lighting control system.

Visible light communication (VLC) refers to communication in the visible part of the spectrum. This involves a VLC transmitter that transmits information by modulating its light output and a receiver that is capable of decoding the transmitted information. Embedding information by modulating light output has become easier with the advent of LEDs that allow for high switching frequencies. Assuming overlapped LED emitting and sensing spectra, reception of optical signals using LEDs is feasible. Our third sub-goal in this research is therefore: *Sub-goal 3: To provide flick-free illumination and unidirectional visible light communication between two LED devices, without dedicated light sensors.*

In Chapter 4, we proposed a LED system for jointly achieving VLC while providing flicker-free illumination. At the transmitter, a redundant run-length limited encoding scheme and multi-level dimming are considered for data transmission, with a wide dimming range. The receiver uses pulse-width modulation and uses the OFF periods for VLC reception. It is allowed for the receiver to be asynchronous to the transmitter, with a phase offset within a preset range. A key feature of the proposed system is that no dedicated devices are used for transmission / reception, since the illumination LEDs are used for these functions. We design a functional prototype of this system and evaluate the communication bit error rate and illumination flicker performance experimentally.

The proposed calibration scheme at the receiver in Chapter 4 assumed a fixed communication distance between the two LED devices and that the ambient light conditions did not change rapidly. Ambient light changes (e.g. slow daylight variations) can however limit the effective communication range in such a system.

To address this problem, we consider an adaptive VLC system. At the transmitter side, we consider a weighted combination of a PWM signal and a redundant RLL encoded OOK signal, where the weights are designed to achieve a target dimming level and enhance the transmit signal-to-noise ratio (SNR). At

the receiver, a method for adaptive threshold detection is proposed. We compare the proposed adaptive VLC system with the non-adaptive VLC system in Chapter 4 in terms of bit error rate (BER) performance using an experimental single LED system prototype. The fourth sub-goal in this research is therefore *Sub-goal 4: To enhance the unidirectional visible light communication performance between two LED devices.*

In Chapter 5, we presented the design of a LED based VLC system where the LED is used for adaptive VLC transmission and reception, as well as for illumination. In the proposed design, the modulation index at the transmitter as well as calibration detection thresholds at the receiver are adapted to react to changes in ambient illumination conditions and limited LED device portability. Using an experimental prototype system, we showed that an increase of almost 30% in reliable communication distance can be obtained in comparison to a non-adaptive VLC system in Chapter 4.

Finally, with the goal of improving the system rate, we consider two LED devices that can provide illumination and simultaneously transmit information to each other, while additionally serving as light sensors to receive this information. Our fifth sub-goal in this research is therefore: *Sub-goal 5: To provide flicker-free illumination and full-duplex visible light communication between two LED devices, without dedicated light sensors.*

In Chapter 6, we proposed a system consisting of two LED devices that are used for two-way VLC while also providing illumination. We consider Manchester coding and on-off keying for transmission. A reception scheme in which the LEDs themselves are used as receivers by sensing in the off periods is considered. A synchronization scheme to achieve frame- and symbol-level synchronization is proposed. A prototype of the proposed system is designed and the communication performance is evaluated.

Last but not least, in Chapter 7, the main contributions and conclusions of this thesis are summarized, and future research challenges are identified.

SUMMARY

Curriculum vitae

Shuai Li was born on 27-06-1987 in Shanxi, China. After finishing the B.Sc. study in 2009 at the Southwest University of Science and Technology (SWUST) in Sichuan, China, he did a M.Sc study in communications engineering at the RWTH Aachen University in Aachen, Germany. In 2012, he graduated within the Institute for Communication Technologies and Embedded Systems (ICE) on the subject “Automated Synthesis Flow for embedded FPGAs”. In July 2013, he started working at Philips Research, Eindhoven, The Netherlands, while pursuing a Ph.D. degree with the Eindhoven University of Technology of which the results are presented in this dissertation.

His research interests are in the areas of light-harvesting wireless sensor networks, daylight- and occupancy-adaptive indoor lighting control and LED-to-LED visible light communications.

Curriculum vitae

Acknowledgement

Foremost, I would like to express my deepest appreciation to my daily supervisor at Philips Lighting Research and co-promotor, dr. Ashish Pandharipande, for all his support, guidance and encouragement throughout the past years.

I would like to thank my promotor, prof. dr. ir. Frans M. J. Willems. Frans has been extremely patient and helpful. His comments and suggestions during all the stages of my PhD work have greatly contributed to improving the quality of this dissertation.

I am very thankful to prof. dr. ir Jan Bergmans, for his help with the coordination between Eindhoven University of Technology and Philips Research in the early phase of my PhD program.

Special thanks to prof. dr. U. Mitra, prof. dr. G. Q. Zhang, prof.dr.ir. S.M. Heemstra, prof. dr. ir. S.M. Heemstra and prof.dr.ir. J.P.M.G. Linnartz for being part of the doctorate committee.

My sincere thanks also goes to dr. Martin Elixmann and dr. Jos van Haaren for their warm encouragement and support while I was working as the Van der Pol Junior under their department groups at Philips Research and Philips Lighting Research. In particular, I would like to express my gratitude to some colleagues with whom I closely collaborated: dr. David Caicedo, dr. Hongming Yang and Sri Andari Husen.

Last but not least, a word of gratitude to my family in China. I would like to thank my parents, Yongzhong and Hailian, and my girlfriend Jiahang, for their unconditional love and support.

Thank you all,

Shuai Li
May 21, 2017